Efficient FEM Simulation Techniques for Thixoviscoplastic Flow Problems

Dissertation
zur Erlangung des akademischen Grades eines
Doktors der Naturwissenschaften
(Dr. rer. nat.)

Der Fakultät für Mathematik
der Technischen Universität Dortmund
vorgelegt von

Naheed Begum

im Juli 2023

Dissertation

Efficient FEM Simulation Techniques for Thixoviscoplastic Flow Problems

Fakultät für Mathematik

Technische Universität Dortmund

Erstgutachter: Prof. Dr. Stefan Turek

Zweitgutachter: Privatdozent Dr. Andriy Sokolov

Tag der mündlichen Prüfung: 16.11.2023

Abstract: This thesis is concerned with the numerical simulations of thixoviscoplastic (TVP) flow problems. As a nonlinear multifield two-way coupled problem, the analysis of thixoviscoplasticity in complex fluid processes would present a great challenge. Numerical simulations are conceived as economic and credible tools to replicate thixoviscoplastic phenomena in different flow circumstances. This thesis proceeds to provide efficient numerical methods and corresponding algorithmic tools to fulfill this goal.

To start with, we used a quasi-Newtonian modeling approach to integrate thixotropy in yield stress materials. Substantially, this is done simply by introducing a microstructure-dependent extended viscosity function into the rheological model for yield stress materials. Then, the generalized Stokes equations are supplemented with an evolution equation for microstructure, which controls the interplay of *shear rejuvenation* and *aging* processes via breakdown and buildup functions. We used the classical Bercovier-Engelmann's and Papanastasiou's regularizations to define the extended viscosity function.

Then, we generalized the standard FEM settings of Stokes equations, and proceeded with the well-posedness study of the problem to set the foundation for the approximate problem, and for the efficient solver. The well-posedness of the microstructure and viscoplastic subproblems are treated simultaneously. For the viscoplastic subproblem, we used the monotonicity property of the viscoplastic operator for diffusion. For the microstructure subproblem, for a given divergence-free velocity field, we used the weak coercivity and the continuity of the corresponding bilinear form. Then, for the multifield coupled TVP problem, we used a nonlinear contraction property for a mapping, a translation mapping of the corresponding thixoviscoplastic problem with a nonthixotropic one, acting on the set of admissible solutions to show the existence and uniqueness of a Fixed point solution and deduce the existence and uniqueness for coupled TVP problem.

In the context of solver, we advantageously use the delicate symbiosis aspects of the problem settings for FEM approximations, and the algorithmic tools to develop a TVP solver. It is based on a monolithic Newton-multigrid approach, where we treated the nonlinearity of the problem in a black box framework with an adaptive combined discrete Newton's method and a monolithic geometric multigrid solver. The linear systems inside the outer nonlinear iterations are solved in a block Gauss-Seidel way, where the construction of the blocks is based on incompressibility constraint. We efficiently handled the problem coupling locally with our choice of *discontinuous* linear pressure. Furthermore, due to the absence of pressure and microstructure coupling, we collocate the microstructure with the velocity in the quadratic FEM approximation to maintain the solver efficiency. Moreover, we deal with the weak coercivity of microstructure form with edge-oriented stabilization, to upgrade the coercivity to match the space norm. It is consistent with FEM discretization, linear with respect to the problem, and in addition, it enhances the efficiency of the solver.

Most importantly, we used the numerical simulations of thixoviscoplastic flow problems as a useful tool to understand the complex phenomena of interplay between plasticity and thixotropy. We incorporated thixotropy in well-established academical benchmarks, namely channel flow and lid-driven cavity flow. In the former, we developed a reduced one-dimensional TVP solver, then we generated reference solutions for higher-dimensional FEM fully developed TVP flow problem. We used the one-dimensional reference solutions as a validation mechanism, and as necessary Dirichlet boundary conditions at the inflow for microstructure, or as alternative Dirichlet boundary conditions instead of "do-nothing" at the outflow. For the latter, we used lid-driven cavity case for the visual validations of the solution's domains, and to optimize the algorithmic tools. For both, channel, and lid-driven cavity flows, we related the sharpness of interfaces between unyielded and yielded regions to microstructure via evolution process, which occurs in the transitions at the boundary limit of the regions. In addition, we anticipated equations in cross engineering disciplines to model and replicate numerically and experimentally rheological phenomena, namely shear localization and shear banding in Couette devices. In the end, we used thixotropy in contraction configuration to generate breakdown layers at the vicinity of the downstream channel's walls, that keep the TVP material smoothly flowing along the downstream channel. Consequently, our findings highlight the benefit of including the material microstructure, namely thixotropy, in material rheology. As an industrial application, the optimal settings for restart pressure in waxy crude oil transportation.

Key words: Thixoviscoplastic flows, FEM, Newton-multigrid, Local pressure Schur complement

Naheed Begum
TU Dortmund University, Germany

Dedicated to My Lovely Mother

Naheed Begum

Acknowledgement. Thank you Prof. Dr. Stefan Turek for supervising my thesis. Your significant accomplishments in the world of non-Newtonian fluid flow simulations, your well-known internationally recognized achievements in academia, working with you is a dream came true. In the beginning it was FeatFlow summer school. This memorable experience to witness the international and cooperative research atmosphere that you created within your chair, made it easy for me to go for the realization of my PhD thesis here at LSIII TU Dortmund University. To add, the different projects you made me actively involved opened my academical background towards the concrete industrial applications. In addition, the different teaching courses I was engaged in during my journey, kept my momentum high, and refined my didactic skills. An important point, your constant insist to present the results in seminar platforms and to participate in international conferences was of great motivation to take my ideas from the existence in thoughts to the existence in papers, then your readiness to go through my research reports was great incentive for me to take my ideas to the next level. You was available whenever needed, despite your busy schedule as Dean. Your optimism and easygoing communication made the unthinkable occurring reality. Your office was always open for discussions. All these important points contributed to see my thesis come to this stage, and makes my PhD journey a great experience. Stefan, thanks once more for accepting to review my thesis.

I am grateful to Privatdozent Dr. Andriy Sokolov, for accepting to review my thesis. Your versatile scientific background, particularly topics covered in your habilitation, discussions with you helped me to deepen my understanding and bridging it into my own TVP problem. As well as, your feedback remarks and suggestions were of great help. Thank you Andriy.
An immense thanks to you Prof. Dr. Matthias Röger, for accepting to be examiner within the jury of my thesis. Your expertise helped me to see my thesis with the lens of the material you suggested me. I really appreciate all the discussion rounds in a very welcoming and energetic mood, even at short notice. Your flexibility made it possible to conduct the PhD defense exam despite your busy calender. Thank you Matthias. Thank you Matthias. Prof. Dr. Joachim Stöckler, thank you for managing the thesis's defense, and made it happen in the perfect circumstance. As head of the PhD defense committee, communication with you was very efficient and easygoing. I have to confess that knowing you along tutoring your lecture, including the weakly planing meeting, it was a joyous and memorable experience. You are really so kind and illuminating person. Thank you Joachim.
Alrun Lamprecht, your perfection to manage our administrative documents, your readiness to help with all bureaucratic papers and conferences travels, enabled me to free my mind to focus on science. Thank you Alrun. Susanne Drees, administrating our preprint series, you did it perfectly. Thank you Susanne. Alrun and Susanne, I and all LSIII members are fortunate to have you.

Dr. Abderrahim Ouazzi, thank you for your sincere engagement in our scientific discussions, I am fortunate to work with you. Thanks Abderrahim. Dr. Hogenrich Damanick, thanks for your availability to share your coding and teaching expertise. Your step-by-step clarification of my scientifically concerned issues showed me how enthusiastic you are to take away my queries. Your constant motivation for thesis write-up and sharing experience of your own, without it this thesis could not come to this current stage. Thanks Hogen, your proofreading was a great help for improvement. Dr. Timm Treskatis thank you for proofreading, it was of great help to address important points with different perspective. Thank you for sharing your valuable research expertise in the field of of viscoplastic flow simulations. Thanks Timm. Dr. Christoph Lohmann, your proofreading given your wide-range expertise, and your scientific input helped me to refine theoretical aspect, and to bring the thesis in this final stage. Your constant motivation during thesis write-up helped me to keep the momentum, Thanks Christoph. M. Sc. Florian Streitbürger, M. Sc. Michael Fast, M. Sc. Muhammad Tayyab Bin Saghir, your friendly character and cooperative attitude made the teaming-up with you for the courses a memorable experience. Your company during conferences is appreciated. Florian, Michael, Tayyab thank you all. Dr. Christian Becker, to update the software system for my poster presentation is one example of your kindness. And the valuable MRB's work with Dipl.-Inf. Dirk Ribbrock to bring the up-to-date HPC infrastructure for our fancy simulations is amazing. Chritian, Dirk, I and all LSIII members are lucky to work with you. Dear LSIII members, all of you, the formers, the currents, each one of you made my PhD journey a true learning experience.

Dr. Patrick Westervoß, it was an amazing experience to work with you specially on SKZ project. You introduced me to the world of filled polymers simulations, and your expertise to take the integrated perspective of industrial partners and merging it in ours, this was a true learning experience. Our routing ‘‘with motive to take all scientific

worries away" during daily afternoon meeting, was a clock set-back moment for me. Being office-mate, and working with same code accelerated the implementation aspect of my PhD project. To you Dr. Malte Schuh, your helping attitude and the amazing discussion-rounds made me feel home. Your help with respect to ParaView, thesis submission process, and much more, are not forgotten. Malte, it was kind from you to make me live your PhD journey experience, it was great help for me to conduct mine in ease. Thank you Malte. To Robert Jendrny, your fruitful discussions in a friendly atmosphere made our office a great work-place. Organizing the annual LSIII gathering event with you was great fun experience. I feel fortunate to have you all as great officemates ever.

M. Sc. Abida Begum, to have you as an amazing friend, evening walks with you in the campus, and discussion of amazing future goals during lunch-breaks in mensa, filled me with energy and made my working days pleasant. Abida, thank you.

Dr. Sadia Siddiqa, Dr. Sahrish Naqvi, Dr. Hina Qammar, Ing. Muhammad Rashid, you are my best friends. As eager I am to address each one of you separately, more I am unable to do. You are for me true unity. Your recognized success in your professional life wherever you go, your navigation of life keeping up the standard high, your readiness to give back, and the action you took for empowering the deprived ones, made you true role models. Thank you for the support for my social projects back in our home country and elsewhere, you are the ones to count on. Your goodness is nourishing my existence. Sadia, Sahrish, Hina, Muhammad, I am fortunate with decades of friendship, thank you.

I am extremely fortunate to have a family which is constant source of love, encouragement and support. Thanks to you Maani, you are filling the gap in my absence, and removing my worries. At your young age to be enthusiastically engaged in my social development projects, made me proud of you and filled me with more energy to keep-up. I am fortunate to have you Maani, thank you. Lucky to have you Sania, your voice is the Call which cherished me during my journey, it was all time heard. Thanks for being my best buddy. Maria, you are for me the best to team-up with. Being extremely dedicated to support child's education, and women's empowerment, made me so proud. Thank you Maria. Thanks Waheed, your peaceful character, helping nature, work ethics, raised the bar for me. Always showing me how proud you are of me, made me feel blessed, and helped me to navigate life's difficulties with ease. I am so happy to have you, and I am proud of you. Dua Ayesha, to see you carrying out the family tradition is my motivation. I hope with my work to bring it to you in better way. Dua, you are my source of energy, I love you. My beloved Father, you murmured your expectation for me. Your soft utterance is Accelerando in me, engaged my entirety to let your expectations strongly heard. My only reason for existence my beloved Mother, you are filling every breath I take, you are covering every part of my sky. Every step you did with and for me is engraved in me. No way to try to give back, simply expressing gratitude, this work is dedicated to you. Both Ami and Abu, only because of you, I am the person who I am today. I love you both. Jahangir Ahmed, Aroosa Ahmed, and Nasim Ahmed, your love, your constant support, your understanding, I feel very fortunate to have you in my life. Your engagement in my social projects, setting-up new amazing goals with me, made me feel proud. You made my PhD journey quite memorable, thank you all. My beloved Grandfather, growing up under your care, holding up your finger, I was absorbing the wisdom of the first without knowing. My life's journey is revealing to me your valuable words and guideline ethics. Your last-glance for me is an ever-remembering call to make you proud of your legacy. This PhD thesis is a drop in your ocean that I am exploring.

Financial and compute resources: This work was financially supported by DAAD, a scholarship grant, and a BMWK grant. I most gratefully acknowledge the funding provided by Deutscher Akademischer Austauschdienst (DAAD) through the funding program /-ID: Research Grants-Doctoral Programmes in Germany 2016/17-(57214224), and ‘‘Bundesministerium für Wirtschaft und Klimaschutz (BMWK) aufgrund eines Beschlusses des Deutschen Bundestages" through ‘‘AiF-Forschungsvereinigung:Forschungs- Gesellschaft Verfahrens Technik .e V. - GVT" under the IGF project number ‘‘20871 N".
I would also like to gratefully acknowledge the support by LSIII and LiDO3 team at ITMC, TU Dortmund University, Germany.

Table of Contents

1

Introduction

In this thesis, we aim to investigate thixoviscoplasticity in fluid flow problems with the lens of numerical simulations, as economic and credible tools to understand complex material rheology.

1.1 Thesis Overview

Thixoviscoplastic flow integrates the competitive process of *Aging* and *Rejuvenation* inhabited in the material via plasticity and thixotropy interplay. The viscoplastic equations are supplemented with the evolution microstructure equation, which incorporates buildup and breakdown functions responsible for the process. It is a nonlinear multifield two-way coupled problem. Beside, the microstructure-velocity coupling by means of microstructure dependent plastic-viscosity, and yield stress, thixoviscoplastic flow possess the velocity-microstructure coupling due to not only the convection, but also to the shear rate dependent buildup and breakdown functions. In addition, thixoviscoplastic flows incorporate different types of nonlinearities, often with conflictual properties, which make the numerical simulations a true challenge.

To generalize the standard finite element methods (FEM) settings of Navier-Stokes equations, we use a FEM quasi-Newtonian modeling approach for thixoviscoplastic flow. This approach integrates the internal material microstructure within extended viscosity defined on full simulations domain. We use the classical Bercovier-Engelmann's [13] and Papanastasiou's [66] approximations for Frobenius norm of shear rate to define the extended viscosity. The dependence of this approximation modeling approach on regularization parameter raises challenges with respect to numerical solvers. In this regard, we develop a corresponding monolithic Newton-multigrid solver to delicately handle the regularization issue. We use Local Pressure Schur Complement (LPSC) techniques [76] to handle the linearized saddle point problems inside the outer Newton sweeps, taking into consideration the advantageous aspect of discontinuous linear pressure FEM approximation, and the collocation of velocity and microstructure in the same FEM quadratic interpolation.

With the goal to incorporate thixotropy in complex flow processes, we anticipate the flow simulations in wide range of circumstances. We provide thixoviscoplastic flow simulations in configurations of academic background, modeling interest, and industrial applications. That is, channel flow as well as lid-driven cavity as long-standing and well documented flow benchmarks, Couette flow as a simple enough for modeling and experimental testing, and 4:1 contraction flow as a close enough to industrial applications.

1.2 Problem Settings of Thesis

Here, we give the settings of thixoviscoplatic (TVP) flow problem, for this thesis, based on FEM quasi-Newtonian modeling approach. To do so, we approximate the Frobenius norm of deformation tensor, involved in the thixoviscoplatic constitutive model, with Bercovier-Engelmann's regularization [13],

$$\frac{1}{\sqrt{D_{\text{II},r}}} := \frac{1}{\sqrt{D_{\text{II}}{}^2 + k^2}}, \tag{1.1}$$

or, with Papanastasiou's regularization [66],

$$\frac{1}{\sqrt{D_{\text{II},r}}} := \frac{1}{\sqrt{D_{\text{II}}}} \left(1 - e^{-k\sqrt{D_{\text{II}}}}\right), \tag{1.2}$$

where k is a regularization parameter, and $D_{\text{II}} = \frac{1}{2}\left(\mathbf{D}(\boldsymbol{u}) : \mathbf{D}(\boldsymbol{u})\right)$ is the second invariant of deformation tensor, $\mathbf{D}(\boldsymbol{u}) = \frac{1}{2}\left(\nabla \boldsymbol{u} + (\nabla \boldsymbol{u})^{\mathrm{T}}\right)$. Then, we define the extended viscosity, $\mu(\cdot,\cdot)$, dependent on shear rate, $D_{\text{II},r}$, and microstructure, λ,

$$\mu(D_{\text{II},r}, \lambda) = \eta(D_{\text{II}}, \lambda) + \tau(\lambda)\frac{\sqrt{2}}{2}\frac{1}{\sqrt{D_{\text{II},r}}}, \tag{1.3}$$

where, $\eta(\cdot,\cdot)$, and $\tau(\cdot)$ are microstructure dependent plastic-viscosity, and yield stress respectively. And we rewrite the full set of TVP generalized Navier-Stokes equations

$$\begin{cases} \left(\dfrac{\partial}{\partial t} + u \cdot \nabla\right)\boldsymbol{u} - \boldsymbol{\nabla} \cdot \left(2\mu(D_{\text{II},r}, \lambda)\mathbf{D}(\boldsymbol{u})\right) + \nabla p = \boldsymbol{f}_{\boldsymbol{u}}, \\ \nabla \cdot \boldsymbol{u} = 0, \\ \left(\dfrac{\partial}{\partial t} + u \cdot \nabla\right)\lambda + \mathcal{M}(D_{\text{II},r}, \lambda) = f_\lambda, \end{cases} \tag{1.4}$$

in Ω. We denoted flow fields, microstructure, velocity, and pressure, by λ, $\boldsymbol{u}$, and p, respectively, and source terms by f_λ and $\boldsymbol{f}_{\boldsymbol{u}}$.

The microstructure equation for λ, which supplements the generalized Stokes equations, in (2.18) is responsible to integrate breakdown, $\mathcal{G}$, and buildup, $\mathcal{F}$, competition process. We concisely define TVP model as

$$\mathcal{M} := \mathcal{G} - \mathcal{F}. \tag{1.5}$$

We summarize a collection of thixotropic models from the literature in Table 1.1.

Table 1.1: Models for thixotropic materials

	η	τ	$\mathcal{F}$	$\mathcal{G}$
Worrall et al. [82]	$\lambda\,\eta_0$	τ_0	$\mathcal{M}_a(1-\lambda)\,\lVert\mathbf{D}\rVert$	$\mathcal{M}_b\lambda\,\lVert\mathbf{D}\rVert$
Coussot et al.[29]	$\lambda^g\,\eta_0$		$\mathcal{M}_a$	$\mathcal{M}_b\lambda\,\lVert\mathbf{D}\rVert$
Houška [45]	$(\eta_0 + \eta_\infty\lambda)\,\lVert\mathbf{D}\rVert^{n-1}$	$(\tau_0 + \tau_\infty\lambda)$	$\mathcal{M}_a(1-\lambda)$	$\mathcal{M}_b\lambda^m\,\lVert\mathbf{D}\rVert$
Mujumbar et al. [59]	$(\eta_0 + \eta_\infty\lambda)\,\lVert\mathbf{D}\rVert^{n-1}$	$\lambda^{g+1}G_0\Lambda_c$	$\mathcal{M}_a(1-\lambda)$	$\mathcal{M}_b\lambda\,\lVert\mathbf{D}\rVert$
Dullaert et al. [33]	$\lambda\eta_0$	$\lambda G_0(\lambda\,\lVert\mathbf{D}\rVert)\Lambda_c$	$(\mathcal{M}_{a_1} + \mathcal{M}_{a_2}\,\lVert\mathbf{D}\rVert)(1-\lambda)t^p$	$\mathcal{M}_b\lambda\,\lVert\mathbf{D}\rVert\,t^{-p}$

The model parameters, buildup parameter, $\mathcal{M}_a$, breakage parameter, $\mathcal{M}_b$, nonthixotropic plastic viscosity, η_0, nonthixotropic yield stress, τ_0, thixotropic plastic viscosity, η_∞, thixotropic yield stress, τ_∞, critical elastic strain, Λ_c, elastic modulus of unyielded material G_0, and indices rate g, p, m, n, give rise to different thixotropic models.

The thixotropic models in Table 1.1 include different nonlinearities, beside time dependency in equations (1.4), make the Sobolev spaces for a general FEM settings very wide and diffuse the goal aligned for this thesis. We content to limit the investigations for the time independent problems, and shear rate independent plastic-viscosity. So, the well-posedness of the problem follows accordingly. Without restriction, the thixotropic phenomena is replicated in the flow simulations, and the extension to include the other models and time dependency from solver perspective, is straightforward.

1.3 Originality of Thesis

The originality of this work is not limited to one research area, rather it has multi-aspects which covers the theoretical analysis, numerical method, implementation of efficient algorithmic tools, and applications for thixoviscoplastic flow problems.

To start with, we build the foundation for analysis of multifield dependent viscosity for complex flow problems. We highlight the micro-macro structure connections in flow problems with well accepted thixoviscoplastic models. In this regard, in our first paper [63] we used quasi-Newtonian modeling to have microstructure dependent viscosity, and outlined the abstract framework settings for further FEM analysis. We used simple thixoviscoplastic Houška to convey the micro-macro structure connections via unidirectional flow simulations.

Then in chapter 2, we investigate the solvability of thixoviscoplastic flow problems in general context of nonlinear multifield coupled problem facing all mathematical challenges with respect to different types of nonlinearities. The chapter is based on our published work [9, 5]. We give the main technical ingredients, that is spaces for FEM settings, important results from functional analysis, to establish the well-posedness of Houška thixoviscoplastic flow problem. Furthermore, we provide Houška thixoviscoplastic flow simulations in contraction configuration in [9], and upgrade the Bingham viscoplastic benchmark channel flow to incorporate thixotropy in [5].

The important aspect concerning efficient solver is addressed in Chapter 3, we use the FEM problem's settings, the well-posedness and error analysis results, published in *Proc. Appl. Math. Mech.* series [8, 12, 10], to develop numerical techniques for efficient solver. The solver is monolithic, and based on Newton and multigrid methods for multifield TVP problem. Furthermore, the solver's algorithms are written in a clear mathematical framework, which provide the foundation for further theoretical convergence analysis investigations.

The core of the thesis is the numerical simulation aspect in Chapter 4, we incorporate thixotropy in well established academical benchmarks, namely channel flow and lid-driven cavity flow, published in [7, 5]. For the channel flow, we developed of a reduced one-dimensional TVP model to generate reference solutions for higher-dimensional fully developed flows. The reduced one-dimensional solutions are used for validations, or as necessary Dirichlet boundary conditions at the inflow boundary for microstructure, or as alternative Dirichlet boundary conditions instead of "do-nothing" at the outflow. For lid-driven cavity flow, we use it for the visual validations of the solution's domains, and to optimize the algorithmic tools. For both, channel flow, and lid-driven cavity flow, we relate the width of interfaces between unyielded and yielded regions to microstructure via competition process, which take place in the transitions at

the boundary limit of the regions. In addition, we anticipate equations in cross engineering disciplines to model and replicate numerically and experimentally rheological phenomena, namely *shear localization* and *shear banding* in Couette device. The discussion and the findings were published in [11]. Lastly, we use thixotropy to generate breakdown layers at the vicinity of downstream of contraction flow, which keep TVP material smoothly flowing along the downstream channel. The results are published in [6], which recommend as well to take into consideration the microstructure of the material in industrial applications by bringing into focus the start-up in waxy crude oil transportation.

1.4 Guideline for Readers

The thesis is composed of five chapters covering the problem from modeling, FEM analysis, numerical methods, algorithmic tools, and simulations perspectives. Each chapter is made optimally self-content with necessary subsections, a brief opening introductive guidance, and interim concluding remarks. The reader can navigate freely between the chapters without the numbering order's restriction.

1.5 Thesis Organization

Chapter 2 is concerned with the well-posedness of TVP flow problems in FEM context. We start by introducing the variational principle and functional spaces in the context of shear rate independent plastic viscosity. Then, we express the continuous TVP problems in a classical abstract setting of saddle point problems based on the incompressibility constraint, and the approximated one in conforming framework. We treat the existence and uniqueness of the microstructure and viscoplastic subproblems in parallel manner. For the viscoplastic subproblem, we use monotonicity property of viscoplastic operator for the diffusion. For microstructure subproblem, for a given divergence-free velocity, we use the weak coercivity and continuity of the corresponding bilinear form. Then, for the multifield coupled TVP problem we use the nonlinear contraction property for the mapping, translation mapping of the corresponding TVP problem with a nonthixotropic one, acting on the set of admissible solutions to show the existence of a fixed point solution to deduce the existence results for the coupled TVP problem.

Then, in Chapter 3, we develop FEM-TVP solver based on monolithic Newton-multigrid method to tackle TVP generalized Stokes equations. In our approach, we treat the nonlinearity of the problem in black box framework using an adaptive combined discrete Newton's and monolithic geometric multigrid solver. The linear systems inside the outer nonlinear iterations are solved in a block Gauss-Seidel way, where the construction of the blocks is based on incompressibility constraint. Furthermore, with our choice of *discontinuous* linear pressure approximation P_1^{disc}, we efficiently handle the problem coupling locally. To maintain the solver efficiency with the fact of noncoupling of pressure and microstructure, we collocate the microstructure and the velocity components in the same quadratic FEM approximations Q_2. We overcome the lack of strong coercivity of microstructure form with stabilization, that is edge-oriented jump of the gradient to upgrade the coercivity to match the space norm. It is consistent with FEM discretization, linear with respect to the problem, and in addition it enhances the solver efficiency.

In Chapter 4, we extensively analyze thixoviscoplastic flows in different flow configurations of academic background, modeling interest, and industrial applications. Firstly, we elevate the viscoplastic channel flow benchmark to incorporate microstructure. We took the reduced one-dimensional solutions profiles to provide the necessary boundary conditions (inflow boundary conditions), alternative boundary conditions

at the outflow (Dirichlet instead of "do-nothing"), beside that as a solution's validation mechanism at each x-axis cross section along the channel. Followed by the well documented and long standing lid-driven cavity benchmark, to validate thixoviscoplastic solutions point-wisely, and to analyze the performance of monolithic Newton-multigrid solver for TVP as an example of coupled multifield problems. Secondly we revisit the powder Couette flow, on hand to validate and calibrate our numerical method for an optimal settings with experimental data that we lack for thixoviscoplastic material, on other hand to highlight the issue of the types of transitions between fluid-like and solid-like zones. Then, we use buildup and breakdown within the microstructure to categorize the type of transitions into shear localization and shear banding. Lastly, we use contraction configuration as a close enough for industrial and engineering applications, to analyze the thixotropic phenomena, namely the competition process of *Shear Aging* and *Shear Rejuvenation*.

In the concluding Chapter 5, we highlight the multi-aspects of our research results, including the newly developed numerical methods and algorithmic tools, that we use for the numerical simulations. We provide the substantial extensions of this work in the direction of time-dependent problems, and also in models with constitutive laws toward thixotropic elasto-viscoplastic (TEVP) flows [41, 72, 73].

1.6 Publications and Presentations Parallel to Thesis

During the course of this PhD journey, side-by research challenges were elevated and the findings were made publicly available. Here is the list of publications and presentations parallel to Thesis.

1.6.1 Publications

1. Ouazzi, A., Begum, N., Turek, S., Newton-Multigrid FEM solver for the simulation of quasi-Newtonian modeling of thixotropic flows, **700**, *Numerical Methods and Algorithms in Science and Engineering*, 2021, [63].
2. Begum, N., Ouazzi, A., Turek, S., Finite element methods for the simulation for the simulation of thixotropic flow, *9th edition of the International Conference on Computational Methods for Coupled Problems in Science and Engineering*, DOI: 10.23967/coupled.2021.028, 2021, [6].
3. Begum, N., Ouazzi, A., Turek, S., Monolithic finite element method for the simulation of thixoviscoplastic flows, *Book of Extended Abstracts of the 6th Eccomas Young Investigators Conference*, https://doi.org/10.4995/YIC2021.2021.12250, 2021, [7].
4. Begum, N., Ouazzi, A., Turek, S., Monolithic Newton-multigrid FEM for the simulation of thixotropic flow problems, **21**, *Proc. Appl. Math. Mech.*, 10.1002/pamm.202100019, 2021, [8].
5. Begum, N., Ouazzi, A., Turek, S., FEM analysis and monolithic Newton-multigrid solver for thixoviscoplastic flow problems, *ECCOMAS Congress 2022 - 8th European Congress on Computational Methods in Applied Sciences and Engineering*, doi.org/10.23967/eccomas.2022.119, 2022, [9].
6. Begum, N., Ouazzi, A., Turek, S., FEM simulations of thixoviscoplastic flow problems: Error analysis, **23**, 1, *Proc. Appl. Math. Mech.*, 10.1002/pamm.202200294, 2023, [12].
7. Begum, N., Ouazzi, A., Turek, S., FEM modeling and simulation of thixoviscoplastic flow problems, *AIP Conference Proceedings*, in press, 2023, [11].
8. Begum, N., Ouazzi, A., Turek, S., Efficient Newton-multigrid FEM solver for multifield nonlinear coupled problems applied to thixoviscoplastic flows, *Proc. Appl. Math. Mech.*, 2023, [10].
9. Begum, N., Ouazzi, A., Turek, S., FEM simulation for nonlinear multifield coupled problems: Application to thixoviscoplastic flow, *X edition of the International Conference on Computational Methods for Coupled Problems in Science and Engineering*, 2023, [5].

1.6.2 Pro-seminar Talks

1. Begum, N., Ouazzi, A., Turek, S., Monolithic Newton-multigrid FEM for the simulation of thixotropic flow problems, Oberseminar Series, Winter Term 2020/21, *Chair of Applied Mathematics and Numerics LSIII, TU Dortmund, Germany*, 16th March 2021.
2. Begum, N., Ouazzi, A., Turek, S., Monolithic Finite Element Methods for the simulation of thixoviscoplastic flows, Oberseminar Series, Summer Term 2021, *Chair of Applied Mathematics and Numerics LSIII, TU Dortmund, Germany*, 6th July 2021.
3. Begum, N., Ouazzi, A., Turek, S., FEM modeling and simulation of thixoviscoplastic flow problems, Oberseminar Series, Winter Term 2022, *Chair of Applied Mathematics and Numerics LSIII, TU Dortmund, Germany*, 2nd March 2022.

1.6.3 Presentations in Conferences

1. Ouazzi, A., Begum, N., Turek, S., Newton-multigrid FEM solver for the simulation of quasi-newtonian modeling of thixotropic flows,WCCM-ECCOMAS 2021, *14th World Congress on Computational Mechanics WCCM, Virtual Congress*, 11-15 January 2021.
2. Begum, N., Ouazzi, A., Turek, S., Monolithic Newton-multigrid FEM for the simulation of thixotropic flow problems, GAMM 2020-21, *91st Annual Meeting of the International Association of Applied Mathematics and Mechanics*, 15-19 March 2021, Kassel, Germany.
3. Begum, N., Ouazzi, A., Turek, S. Monolithic Finite Element Methods for the simulation of thixotropic flows, COUPLED2021, *IX International Conference on Computational Methods for Coupled Problems in Science and Engineering*, 13-16 June 2021, Chia Laguna, Sardinia,Italy.
4. Begum, N., Ouazzi, A., Turek, S., Monolithic Finite Element Methods for the simulation of thixoviscoplastic flows, YIC2021, *6th ECCOMAS Young Investigators Conference*, 7-9 July 2021, Valencia Spain.
5. Begum, N., Ouazzi, A., Turek, S.,Newton-multigrid FEM solver for the simulation of thixoviscoplastic flow problems, PragueSum 2021, *Summer School and Workshop "Fluids under Control"* , 23-27 August 2021, Prague, Czech Republic.
6. Begum, N., Ouazzi, A., FEM analysis and monolithic Newton-multigrid solver for thixoviscoplastic flow problems, ECCOMAS2022, *8th European Congress on Computational Methods in Applied Sciences and Engineering*, 5-9 June 2022, Oslo, Norway.
7. Begum, N., Ouazzi, A., Turek, S., FEM simulations of thixoviscoplastic flow problems, GAMM2022, *92nd Annual Meeting of the International Association of Applied Mathematics and Mechanics*, 15-19 August 2022, Aachen, Germany.
8. Begum, N., Ouazzi, A., Turek, S., FEM analysis and monolithic Newton-multigrid solver for thixoviscoplastic flow problems, *9th GACM Colloquium on Computational Mechanics for Young Scientists from Academia and Industry*, 21- 23 September 2022, Essen, Germany.
9. Begum, N., Ouazzi, A., Turek, S., FEM modeling and simulation of thixoviscoplastic flow problems, ICMSAO'23, *9th International Conference on Modeling, Simulation and Applied Optimization*, 26-28 April 2023, Marrakech, Morocco.
10. Begum, N., Ouazzi, A., Turek, S., An efficient Newton-multigrid FEM solver for multifield nonlinear problems applied to thixoviscoplastic flows, GAMM2023, *93rd Annual Meeting of the International Association of Applied Mathematics and Mechanics*, 30 May -2 June 2023, Dresden, Germany.
11. Begum, N., Ouazzi, A., Turek, S., Monolithic Newton-Multigrid FEM solver for nonlinear multifield coupled problems: Application to thixotropic flow, COUPLED2023, *X International Conference on Computational Methods for Coupled Problems in Science and Engineering*, 4-7 June 2023, Chania, Crete, Greece.

In the following chapter, we address the solvability of thixoviscoplastic flow problems in FEM settings.

2

Finite Element Method for Thixoviscoplastic Flow Problems

This chapter is concerned with the well-posedness of thixoviscoplastic (TVP) flow problems in finite element method (FEM) context. To set the foundation for an efficient monolithic TVP solver, we restrict our study to a quasi-Newtonian modeling approach. We analyze the microstructure and viscoplastic subproblems in parallel manner, then we present the well-posedness of the mutifield coupled TVP problem.

2.1 Introduction

In this chapter, we present the well-posedness of quasi-Newtonian modeling approach of TVP flow problems in FEM context.
Thixoviscoplastic flows are multifield nonlinear coupled problems. Beside the integrated nonlinearity within generalized Navier-Stokes and microstructure equations, thixoviscoplastic problems induce a two way coupling. Such problems are often lacking unified FEM analysis due to the presence of different nonlinearities. Thus, we treat auxiliary microstructure and viscoplastic subproblems with the corresponding suitable analysis tools to guarantee existence and uniqueness of solutions. Then, we proceed with the well-posedness of multifield coupled TVP problem.

In Section §2.2, we introduce Sobolev spaces for the FEM settings for thixoviscoplastic flow problems in context of shear rate independent plastic viscosity, which corresponds to TVP Houška model. That is, the plastic viscosity is exclusively dependent on microstructure. Moreover, we define the necessary inner products and associated norms.

We proceed with the thixoviscoplastic FEM problem settings in Section §2.3. The continuous weak formulation of the TVP problem is presented in general saddle point abstract from. We take the spaces $(H_0^1(\Omega))^d, d = 2$, for velocity, $L_0^2(\Omega)$ for pressure, as a natural choice to derive the weak formulation for Navier-Stokes equations, and $H^1(\Omega)$ space for microstructure field for this thesis. We first derive the weak forms for microstructure and velocity fields, then we demonstrate the derivation of the weak formulation for the coupled field $\tilde{\boldsymbol{u}} = (\boldsymbol{u}, \lambda)$, and present the problem in a general saddle point context. The weak formulation is derived for general domains with different type of boundary conditions, including inflow conditions for microstructure.

Section §2.4 is devoted to the question of existence and uniqueness of the solution of the weak formulation of TVP problem. We start with the well-posedness of microstructure and viscoplastic subproblems, and proceed with the well-posedness of the coupled one. Firstly for viscoplastic subproblem, for a given microstructure field, we use the *Lemma plastic monotonicity in* $\mathbb{R}^{d\times d}$ to demonstrate the monotonicity property. Secondly, the microstructure subproblem for a given divergence-free velocity is a bilinear form with respect to microstructure field. In this regard, we use the weak coercivity and the continuity for the existence and uniqueness of the solution of the microstructure subproblem. As far as the multifield coupled TVP problem is concerned, we proceed by constructing a mapping which acts on the set of admissible solutions and show the existence of the fixed point solution. The main ingredient to show the existence of the solution is the nonlinear contraction property of an auxiliary mapping, which is related to the translation of thixoviscoplastic problem with a nonthixotropic one.

Section §2.5 is concerned with the FEM TVP approximations. We introduce the approximate TVP problem in conforming framework with stable pair for velocity and pressure. And we proceed with the well-posedness of the approximate problem similar to the continuous one, providing strong divergence free assumptions to not overload the new challenges with extra technicalities. We provide boundedness of the solutions with the data. On one hand, the pressure is underdetermined in rigid zones as its bound shows that if the source term tends towards zero, the limit for pressure is not necessarily zero in the limit of regularization parameter. On the other hand, microstructure bound exhibits that the higher order derivatives of microstructure are not controlled, that is the microstructure is only bounded with L^2-norm and boundary norm.

The summarising Section §2.6, highlights conclusions and main results of the chapter. Firstly, we introduce Sobolev spaces for the FEM settings for thixoviscoplastic flow problems. Then, we proceed with the thixoviscoplastic FEM problem settings in general saddle point abstract form. Secondly, we investigate the well-posedness of the continuous TVP problem via the well-posedness of microstructure and viscoplastic subproblems. Lastly, we present the approximate TVP problem in conforming FEM context, show the well-posedness of the problem, and provide the boundedness of the solutions for flow fields with data. To conclude, FEM quasi-Newtonian thixoviscoplastic flow has a solution with respect to data. Furthermore, the pressure is underdetermined in rigid zones and higher order derivatives of microstructure are not controlled.

2.2 Notations and Terminology

For FEM discretization of thixoviscoplastic flow problems, we use Sobolev spaces which are introduced, here, in context of shear rate independent plastic viscosity. In other words, the plastic viscosity is dependent on microstructure exclusively. As a consequence, we introduce Sobolev spaces with an integer power. Moreover, we define the corresponding inner products and associated norms (for details, we refer to [22], [42], and [75]).

A zero order Sobolev space is the space of all square integrable real functions defined in Ω,

$$H^0(\Omega) = \left\{ v \mid \int_\Omega |v|^2 \ d\Omega < \infty \right\}. \tag{2.1}$$

This is the usual real Hilbert space denoted as $L^2(\Omega)$.
The first order Sobolev space, $H^1(\Omega)$, is the space of real functions whose first spatial derivatives are in $H^0(\Omega)$, defined as

$$H^1(\Omega) = \left\{ v \in L^2(\Omega) | \ \nabla v \ \in L^2(\Omega) \right\}. \tag{2.2}$$

In general for an integer m, the space of real functions whose generalized m spatial derivatives are in $L^2(\Omega)$ defined as

$$H^m(\Omega) = \left\{ v \in L^2(\Omega) | \ D^\alpha v := \frac{\partial^{|\alpha|} v}{\partial^{\alpha_1} x_1 \cdots \partial^{\alpha_n} x_n} \in L^2(\Omega), \forall \, |\alpha| \leq m, |\alpha| = \alpha_1 + \alpha_2 + \cdots + \alpha_n \right\}. \tag{2.3}$$

For practicality, we introduce the space of all square integrable real functions with zero mean value in Ω

$$L^2_0(\Omega) = \left\{ v \in L^2(\Omega) \ | \ \int_\Omega v \ d\Omega = 0 \right\} \tag{2.4}$$

which we use as representative of $L^2(\Omega)/\mathbb{R}$.
For the trace of functions, we set $\partial\Omega$ be a Lipschitz boundary of Ω and $\Gamma \subset \partial\Omega$ be any section of $\partial\Omega$. The space of $H^1(\Omega)$ functions with zero trace at the boundary $\partial\Omega$ is denoted by

$$H^1_0(\Omega) = \left\{ v \in H^1(\Omega) \ | \ v_{|\partial\Omega} = 0 \right\}, \tag{2.5}$$

while the space of $H^1(\Omega)$ functions with zero trace at Γ is denoted by

$$H^1_\Gamma(\Omega) = \left\{ v \in H^1(\Omega) \ | \ v_{|\Gamma} = 0, \Gamma \subset \partial\Omega \right\}. \tag{2.6}$$

Furthermore, we set $\boldsymbol{n}$ be the outward unit normal vector to Γ, and define two additional boundary sections [43], inflow boundary, Γ^-,

$$\Gamma^- = \{ \boldsymbol{x} \in \Gamma \subset \partial\Omega \ | \ \boldsymbol{u} \cdot \boldsymbol{n} < 0 \}, \tag{2.7}$$

and outflow boundary [43], Γ^+,

$$\Gamma^+ = \{ \boldsymbol{x} \in \Gamma \subset \partial\Omega \ | \ \boldsymbol{u} \cdot \boldsymbol{n} > 0 \}. \tag{2.8}$$

On theses spaces, we define inner products and corresponding norms (for steady state problems).

We limit the definition of inner product to $L^2(\Omega)$ space, since it is the base of inner products and norms on higher order spaces and to not overload the text with unnecessary symbols.
For all $v, w \in L^2(\Omega)$, we define the inner product on $L^2(\Omega)$ as

$$(v, w) = \int_\Omega vw \ d\Omega, \tag{2.9}$$

and the corresponding norm, which we term zero norm/L^2-norm, as

$$\|v\|_0 = (v, v)^{\frac{1}{2}}. \tag{2.10}$$

For the one order space $H^1(\Omega)$, the associated one norm/H^1-norm is defined for all $v \in H^1(\Omega)$ as

$$\|v\|_1 = \left[(v, v) + (\nabla \ v, \nabla \ v) \right]^{\frac{1}{2}}. \tag{2.11}$$

It is worth to mention that we often use the semi norm $|\cdot|_1$ which we define as

$$|v|_1 = \left[(\nabla \ v, \nabla \ v) \right]^{\frac{1}{2}}. \tag{2.12}$$

Furthermore, for a given vector-valued function, $\boldsymbol{u} \in (H^1(\Omega))^d; d = 2$, we introduce the boundary inner product

$$< v, w >_{\pm} = \int_{\Gamma^{\pm}} |\boldsymbol{u} \cdot \boldsymbol{n}| \; vw ds, \tag{2.13}$$

as well as the associated boundary norm (semi-norm)

$$< v >_{\pm} = < v, v >_{\pm}^{\frac{1}{2}} . \tag{2.14}$$

In what follows, the inner product symbols $(\cdot, \cdot)$, and $\langle \cdot, \cdot \rangle$ are used alternatively with their exact definitions. We are also interested in space of bounded function in Ω, which is the Lebesgue space, defined as

$$L^{\infty}(\Omega) := \{ v : \Omega \to \mathbb{R} \;\; measureable \; and \; |v(x)| < +\infty \;\; almost \; everywhere \; in \;\; \Omega \} , \tag{2.15}$$

with the norm

$$\|v\|_{\infty} = ess.sup_{x \in \Omega} |v(x)|. \tag{2.16}$$

We will often use zero-infinity notation $|\cdot|_{0,\infty}$ to refer to $\|\cdot\|_{\infty}$.
Moreover, for functions with bounded derivatives i.e. $v \in H^1(\Omega)$ such that $\nabla v \in L^{\infty}(\Omega)$, we define one-infinity norm $|\cdot|_{1,\infty}$ as

$$|v|_{1,\infty} = \|\nabla v\|_{\infty} . \tag{2.17}$$

Now, we are ready to go forward to derive the weak formulation of TVP problem. In this regard, we derive the weak form using $H^1(\Omega)$ space for velocity and microstructure. As a consequence, the FEM analysis of the TVP problem follows this specific choice. Using, the exact space for microstructure leads to different FEM analysis, which goes beyond the interest of the thesis.

2.3 Thixoviscoplastic Problem Settings

In this section, we present the continuous weak formulation of generalized Stokes TVP problem. That is,

$$\begin{cases} \dfrac{\partial \boldsymbol{u}}{\partial t} - \boldsymbol{\nabla} \cdot \Big(2\mu(D_{\mathrm{II},r}, \lambda) \mathbf{D}(\boldsymbol{u}) \Big) + \nabla p = \boldsymbol{f_u}, \\ \nabla \cdot \boldsymbol{u} = 0, \\ \left(\dfrac{\partial}{\partial t} + u \cdot \nabla \right) \lambda + \mathcal{M}(D_{\mathrm{II},r}, \lambda) = f_{\lambda}, \end{cases} \tag{2.18}$$

in Ω. Along this thesis, the function $\mathcal{M}(\cdot, \cdot)$ corresponds to Houška TVP model with the power $m = n = 1$ from Table 1.1. We write in the saddle point abstract from based on incompressibility constraint the problem (2.18) in the framework of [22, 42]. To do so, we take the spaces $(H_0^1(\Omega))^d, d = 2$, for velocity, $L_0^2(\Omega)$ for pressure, as a natural choice for the weak formulation of Stokes equations, and $H^1(\Omega)$ for microstructure, for geometry with inflow.

We set $\mathbb{V} := (H_0^1(\Omega))^2, \mathbb{T} := H^1(\Omega)$, and $\mathbb{W} := \mathbb{V} \times \mathbb{T}$ be the product space of velocity and microstructure spaces $\mathbb{V}$ and $\mathbb{T}$, respectively. We denote by $\mathbb{Q} := L_0^2(\Omega)$ the pressure space. To write the problem in the operator form, we introduce the dual spaces $\mathbb{V}'$, $\mathbb{T}'$, $\mathbb{W}' := \mathbb{V}' \times \mathbb{T}'$, and $\mathbb{Q}'$ of spaces $\mathbb{V}$, $\mathbb{T}$, $\mathbb{W} := \mathbb{V} \times \mathbb{T}$,

and $\mathbb{Q}$, respectively. The product space $\mathbb{W}$ and the pressure space $\mathbb{Q}$ are associated with H^1-norm $\|\cdot\|_1$ and L^2-norm $\|\cdot\|_0$, respectively.
Let $\tilde{\boldsymbol{u}} = (\boldsymbol{u}, \lambda)$ be coupled field, for velocity and microstructure, and $\tilde{\boldsymbol{v}} = (\boldsymbol{v}, \xi)$ be its associated test coupled field. We introduce the TVP form for the coupled field defined on $\mathbb{W} \times \mathbb{W} \times \mathbb{W}$ as

$$a_{\tilde{\boldsymbol{u}}}(\tilde{\boldsymbol{u}})(\tilde{\boldsymbol{u}}, \tilde{\boldsymbol{v}}) = a_{\boldsymbol{u}}(\tilde{\boldsymbol{u}})(\boldsymbol{u}, \boldsymbol{v}) + a_{\lambda}(\tilde{\boldsymbol{u}})(\lambda, \xi) \quad \forall\ (\tilde{\boldsymbol{u}}, \tilde{\boldsymbol{v}}) \in \mathbb{W} \times \mathbb{W}, \tag{2.19}$$

which is the sum of velocity form $a_{\boldsymbol{u}}(\cdot)(\cdot,\cdot)$ defined on $\mathbb{W} \times \mathbb{V} \times \mathbb{V}$ and microstructure form $a_{\lambda}(\cdot)(\cdot,\cdot)$ defined on $\mathbb{W} \times \mathbb{T} \times \mathbb{T}$.
We denote by $b(\cdot,\cdot)$, the bilinear form defined on $\mathbb{V} \times \mathbb{Q}$ related to incompressibility constraint.
We also introduce the linear coupled field $l_{\tilde{\boldsymbol{u}}}$ defined in $\mathbb{W}'$ as

$$l_{\tilde{\boldsymbol{u}}}(\tilde{\boldsymbol{v}}) = l_{\boldsymbol{u}}(\boldsymbol{v}) + l_{\lambda}(\xi) \quad \forall\ \tilde{\boldsymbol{v}} \in \mathbb{W}. \tag{2.20}$$

The weak formulation for thixoviscoplastic flow problems (2.18) reads:

Find $(\tilde{\boldsymbol{u}}, p) \in \mathbb{W} \times \mathbb{Q}$ *such that*

$$a_{\tilde{\boldsymbol{u}}}(\tilde{\boldsymbol{u}})(\tilde{\boldsymbol{u}}, \tilde{\boldsymbol{v}}) + b(\boldsymbol{v}, p) - b(\boldsymbol{u}, q) = l_{\tilde{\boldsymbol{u}}}(\tilde{\boldsymbol{v}}), \quad \forall\ (\tilde{\boldsymbol{v}}, q) \in \mathbb{W} \times \mathbb{Q}, \tag{2.21}$$

which is often written equivalently as

Find $(\tilde{\boldsymbol{u}}, p) \in \mathbb{W} \times \mathbb{Q}$ *such that*

$$\begin{cases} a_{\tilde{\boldsymbol{u}}}(\tilde{\boldsymbol{u}})(\tilde{\boldsymbol{u}}, \tilde{\boldsymbol{v}}) + b(\boldsymbol{v}, p) = l_{\tilde{\boldsymbol{u}}}(\tilde{\boldsymbol{v}}) & \forall\ \tilde{\boldsymbol{v}} \in \mathbb{W}, \\ b(\boldsymbol{u}, q) = 0 & \forall q \in \mathbb{Q}. \end{cases} \tag{2.22}$$

For convenience, we also write the strong continuous TVP problem in the following operator form

Find $(\tilde{\boldsymbol{u}}, p) \in \mathbb{W} \times \mathbb{Q}$ *such that*

$$\begin{cases} \mathcal{A}_{\tilde{\boldsymbol{u}}}(\tilde{\boldsymbol{u}})\tilde{\boldsymbol{u}} + \mathcal{B}^{\mathrm{T}} p = \boldsymbol{f}_{\tilde{\boldsymbol{u}}} & \text{in } \mathbb{W}', \\ \mathcal{B}\boldsymbol{u} = 0 & \text{in } \mathbb{Q}'. \end{cases} \tag{2.23}$$

The coupled operator $\mathcal{A}_{\tilde{\boldsymbol{u}}}(\cdot)(\cdot)$ is defined in $\mathbb{W}'$ as

$$\mathcal{A}_{\tilde{\boldsymbol{u}}}(\tilde{\boldsymbol{u}})\tilde{\boldsymbol{u}} = \mathcal{A}_{\boldsymbol{u}}(\tilde{\boldsymbol{u}})\boldsymbol{u} + \mathcal{A}_{\lambda}(\tilde{\boldsymbol{u}})\lambda. \tag{2.24}$$

The operator $\mathcal{A}_{\tilde{\boldsymbol{u}}}(\cdot)(\cdot)$ is the sum of velocity operator $\mathcal{A}_{\boldsymbol{u}}(\tilde{\boldsymbol{u}})(\cdot)$ defined in $\mathbb{V}'$

$$\langle \mathcal{A}_{\boldsymbol{u}}(\tilde{\boldsymbol{u}})\boldsymbol{u}, \boldsymbol{v} \rangle = a_{\boldsymbol{u}}(\tilde{\boldsymbol{u}})(\boldsymbol{u}, \boldsymbol{v}) \quad \forall\ \boldsymbol{v} \in \mathbb{V}, \tag{2.25}$$

and microstructure operator $\mathcal{A}_{\lambda}(\tilde{\boldsymbol{u}})(\cdot)$ defined in $\mathbb{T}'$

$$\langle \mathcal{A}_{\lambda}(\tilde{\boldsymbol{u}})\lambda, \xi \rangle = a_{\lambda}(\tilde{\boldsymbol{u}})(\lambda, \xi) \quad \forall\ \xi \in \mathbb{T}. \tag{2.26}$$

While, the operators $\mathcal{B}$, and $\mathcal{B}^{\mathrm{T}}$ are defined as

$$\langle \mathcal{B}\boldsymbol{v}, q \rangle = \langle \boldsymbol{v}, \mathcal{B}^{\mathrm{T}} q \rangle = b(\boldsymbol{v}, q) \quad \forall\ \boldsymbol{v} \in \mathbb{V}, q \in \mathbb{Q}. \tag{2.27}$$

Now, we turn to detail expressions of previously introduced forms and operators. For all $\tilde{\boldsymbol{u}} = (\boldsymbol{u}, \lambda) \in \mathbb{W}$, the velocity weak form $a_{\boldsymbol{u}}(\cdot)(\cdot,\cdot)$ is given as

$$a_{\boldsymbol{u}}(\tilde{\boldsymbol{u}})(\boldsymbol{u}, \boldsymbol{v}) = \Big(2\mu(D_{\mathrm{II},r}(\boldsymbol{u}), \lambda)\mathbf{D}(\boldsymbol{u}), \mathbf{D}(\boldsymbol{v})\Big) \quad \forall\ \boldsymbol{v} \in \mathbb{V}, \tag{2.28}$$

The coupling of velocity weak form and operator with the microstructure is only through the effective viscosity $\mu(\cdot,\cdot)$. On other hand, the coupling of the microstructure weak form and operator defined as

$$a_\lambda(\tilde{\boldsymbol{u}})(\lambda,\xi) = \Big(\mathcal{M}_a\,\lambda,\xi\Big) + \Big(\mathcal{M}_b\sqrt{D_{\text{II},r}(\boldsymbol{u})}\;\lambda,\xi\Big) - \Big(\lambda,\boldsymbol{u}\cdot\nabla\xi\Big) + \langle\lambda,\xi\rangle_+ \quad \forall\;\xi\in\mathbb{T}, \tag{2.29}$$

is due to the breakdown contribution, second term, convection of microstructure with velocity, third term, and outflow boundary inner product (2.13), fourth term, in (2.29). The weak form and operator for the incompressibility constraint are defined with the negative divergence as

$$b(\boldsymbol{v},q) = -\Big(\nabla\cdot\boldsymbol{v},q\Big) \quad \forall\;q\in\mathbb{Q}, \tag{2.30}$$

in order to have $\mathcal{B}^{\mathrm{T}}$ as the gradient operator. The linear forms due to source terms are defined, respectively, for momentum equation as

$$l_{\boldsymbol{u}}(\boldsymbol{v}) = \Big(\boldsymbol{f}_{\boldsymbol{u}},\boldsymbol{v}\Big) \quad \forall\;\boldsymbol{v}\in\mathbb{V}, \tag{2.31}$$

and for microstructure equation as

$$l_\lambda(\xi) = \Big(f_\lambda,\xi\Big) \qquad\qquad \forall\;\xi\in\mathbb{T}, \tag{2.32a}$$

$$l_\lambda(\xi) = \Big(f_\lambda,\xi\Big) + \langle\lambda_{in},\xi\rangle_- \quad \forall\;\xi\in\mathbb{T}. \tag{2.32b}$$

The linear microstructure form (2.32a) corresponds to a strongly imposed inflow boundary conditions. While, for a weakly imposed inflow boundary conditions, the microstructure space is set to $\mathbb{T} := H^1_{\Gamma}(\Omega)$ and the microstructure linear form is set to (2.32b).

We demonstrate the derivation of the weak form (2.19) through its two components, the velocity weak form (2.28) and the microstructure weak form (2.29).
Let us start with velocity weak form (2.28), we multiply the steady momentum equation (2.18) with a test function $\boldsymbol{v}\in\mathbb{V}$

$$-\int_\Omega \boldsymbol{\nabla}\cdot\Big(2\mu(D_{\text{II},r},\lambda)\mathbf{D}(\boldsymbol{u})\Big)\,\boldsymbol{v}\;d\Omega + \int_\Omega \nabla p\;\boldsymbol{v}\;d\Omega = \int_\Omega \boldsymbol{f}_{\boldsymbol{u}}\boldsymbol{v}\;d\Omega \quad \forall\;\boldsymbol{v}\in\mathbb{V}, \tag{2.33}$$

and integrate by parts, the first and the second terms of (2.33), over a domain Ω with boundary $\partial\Omega$

$$\begin{aligned}\int_\Omega 2\mu(D_{\text{II},r},\lambda)\mathbf{D}(\boldsymbol{u}):\mathbf{D}(\boldsymbol{v})\;d\Omega - \int_{\partial\Omega}\Big(2\mu(D_{\text{II},r},\lambda)\mathbf{D}(\boldsymbol{u}) - p\mathbf{I}\Big)\cdot\boldsymbol{n}\;\boldsymbol{v}\;d\sigma \\ - \int_\Omega p\;\nabla\cdot\boldsymbol{v}\;d\Omega = \int_\Omega \boldsymbol{f}_{\boldsymbol{u}}\boldsymbol{v}\;d\Omega \quad \forall\;\boldsymbol{v}\in\mathbb{V},\end{aligned} \tag{2.34}$$

for a general geometry with boundary $\partial\Omega = \Gamma\cup\Gamma^-\cup\Gamma^+$, we use homogeneity of test function on $\Gamma\cup\Gamma^-$, and do-nothing boundary condition on Γ^+ to cancel the boundary term. We assign the addition of first and second terms of (2.34) to velocity weak form (2.28), and third term of (2.34) to weak divergence form (2.30), and fourth term of (2.34) to linear form (2.31), to conclude expressions of weak forms (2.28), (2.30), and (2.31).

For microstructure weak form, we multiply the steady microstructure equation (2.18) with a test function $\xi\in\mathbb{T}$

$$\int_\Omega \boldsymbol{u}\cdot\nabla\lambda\;\xi\;d\Omega + \int_\Omega \mathcal{M}(D_{\text{II},r},\lambda)\xi\;d\Omega = \int_\Omega f_\lambda\;\xi\;d\Omega \quad \forall\;\xi\in\mathbb{T}, \tag{2.35}$$

and integrate by parts, the first term of (2.35), over a domain Ω with boundary $\partial\Omega = \Gamma \cup \Gamma^- \cup \Gamma^+$. Then, we use the homogeneity of test function on Γ and the value of microstructure at inflow boundary Γ^- to obtain

$$-\int_\Omega \lambda\ \boldsymbol{u}\cdot\nabla\xi\ d\Omega + \int_{\Gamma^+} |\boldsymbol{u}\cdot\boldsymbol{n}|\,\lambda\ \xi\ d\sigma + \int_\Omega \mathcal{M}(D_{\mathbb{II},r},\lambda)\xi\ d\Omega = \tag{2.36a}$$

$$\int_\Omega f_\lambda\ \xi\ d\Omega + \int_{\Gamma^-} |\boldsymbol{u}\cdot\boldsymbol{n}|\,\lambda_{in}\ \xi\ d\sigma \quad \forall\ \xi \in \mathbb{T}. \tag{2.36b}$$

In case of strongly imposed inflow boundary conditions for λ, the boundary term of (2.36b) vanishes to have the linear form version (2.32a) from (2.36b). While, in the case of weakly imposed inflow boundary conditions for λ, the full term of (2.36b) is assigned to the linear form version (2.36b).

We introduced a coupled field $\tilde{\boldsymbol{u}} = (\boldsymbol{u}, \lambda)$ for the TVP problem, and presented the problem in a general saddle point context based on incompressibility. The coupled field is set in H^1, which reduces the admissible solution for microstructure. We derived weak forms on a general domain with different type of boundary conditions, and allowed the problem to satisfy inflow conditions for microstructure in strong as well as in weak sense. Setting microstructure in H^1 gives rise to a challenge that the energy microstructure norm is not a norm in H^1. In what follows, we proceed with the FEM analysis of this choice of space setting. Next section is devoted to well-posedness of TVP problem.

2.4 Well-posedness of Thixoviscoplastic Problem

In the previous section, we presented the TVP problem in general saddle point abstract framework based on incompressibility constraint using a coupled field of velocity and microstructure. We proceed, here, with the question of existence and uniqueness of the solution of weak form of TVP problem.

Theorem 1 (Well-posedness). *Let $\boldsymbol{f_u} \in (L^2(\Omega))^2$ and $f_\lambda \in L^2(\Omega)$, then the thixoviscoplastic problem (2.21) has a solution $(\tilde{\boldsymbol{u}}, p) = (\boldsymbol{u}, \lambda, p) \in \mathbb{W}\times\mathbb{Q}$.*

For the proof of the Theorem 1, we use two intermediate propositions related to viscoplastic subproblem and microstructure subproblem.
Firstly, we introduce the subspace $\mathbb{V}_0 \subset \mathbb{V}$ of divergence-free functions

$$\mathbb{V}_0 = \{\boldsymbol{v} \in \mathbb{V} \mid \nabla\cdot\boldsymbol{v} = 0\}, \tag{2.37}$$

The viscoplastic subproblem: For a given $\lambda \in \mathbb{T}$,
Find $(\boldsymbol{u}, p) \in \mathbb{V}\times\mathbb{Q}$ *such that*

$$\begin{cases} a_{\boldsymbol{u}}(\tilde{\boldsymbol{u}})(\boldsymbol{u},\boldsymbol{v}) + b(\boldsymbol{v},p) = l_{\boldsymbol{u}}(\boldsymbol{v}) & \forall \boldsymbol{v}\in\mathbb{V}, \\ b(\boldsymbol{u},q) = 0 & \forall q\in\mathbb{Q}, \end{cases} \tag{2.38}$$

The microstructure subproblem: For a given $\boldsymbol{u} \in \mathbb{V}_0$
Find $\lambda \in \mathbb{T}$ *such that*

$$a_\lambda(\tilde{\boldsymbol{u}})(\lambda,\xi) = l_\lambda(\xi), \quad \forall \xi \in \mathbb{T}. \tag{2.39}$$

The well-posedness results for viscoplastic subproblem are stated in Proposition 1.

Proposition 1 (Viscoplastic subproblem). *For $\boldsymbol{f_u} \in (L^2(\Omega))^2$, and $\zeta \in \mathbb{T}$ solution of the microstructure subproblem (2.39), there exists a unique solution $\boldsymbol{u} = \boldsymbol{u}(\zeta)$ to the viscoplastic subproblem (2.38), and it satisfies the estimate*

$$\|\boldsymbol{u}\|_1 \leq \frac{1}{\eta_0 \mathcal{C}_k} \|\boldsymbol{f_u}\|_0 , \tag{2.40}$$

$$\|p\|_0 \leq \frac{1}{\beta}\Big(1 + \frac{2\,(\eta_\infty + k\tau_\infty)}{\eta_0 \mathcal{C}_k}\Big) \|\boldsymbol{f_u}\|_0 , \tag{2.41}$$

where $\mathcal{C}_K$ denotes the Korn's inequality constant [61], and β is the Ladyzhenskaya-Babuška-Brezzi (LBB) constant [22].

The well-posedness results for microstructure subproblem are stated in Proposition 2.

Proposition 2 (Microstructure subproblem). *For $f_\lambda \in L^2(\Omega)$, and $\boldsymbol{u} \in \mathbb{V}_0$ solution of viscoplastic subproblem (2.38), there exists a unique solution $\lambda = \lambda(\boldsymbol{u})$ to the microstructure subproblem (2.39), and it satisfies the estimate*

$$\|\lambda\|_0 \leq \frac{1}{\mathcal{M}_a} \|f_\lambda\|_0 , \tag{2.42}$$

$$\mathcal{M}_a \|\lambda\|_0^2 + \frac{1}{2}\langle\lambda\rangle^2 \leq \frac{1}{\mathcal{M}_a} \|f_\lambda\|_0^2 . \tag{2.43}$$

2.4.1 Well-posedness of Viscoplastic Subproblem

We proceed with the investigation of well-posedness of viscoplastic subproblem, similar investigation can be found in [1, 67]. We demonstrate the monotonicity and the continuity of the corresponding viscoplastic nonlinear operator [23, 24, 57, 58]. Here, we introduce two lemmas related to monotonicity and continuity of viscous plasticity in $\mathbb{R}^{d\times d}$.

2.4.2 Lemma Plastic Monotonicity in $\mathbb{R}^{d\times d}$

Lemma 1. *(Monotonicity) For all $\mathcal{X}, \mathcal{Y} \in \mathbb{R}^{d\times d}$, $\zeta \in [0,1]$, and $\tau(\cdot)$ is a mapping defined as $\tau(\zeta) : [0,1] \to [0, \mathcal{R}^+]$, we have*

$$\Big(\tau(\zeta)\frac{\mathcal{X}}{|\mathcal{X}|_{F,r}} - \tau(\zeta)\frac{\mathcal{Y}}{|\mathcal{Y}|_{F,r}}, \mathcal{X} - \mathcal{Y}\Big) \geq 0, \tag{2.44}$$

where, $|\cdot|_{F,r}$ denotes an approximation of the Frobenius norm $|\cdot|_F$, such that

$$|\mathcal{X}|_F \leq |\mathcal{X}|_{F,r} \quad \forall\ \mathcal{X} \in \mathbb{R}^{d\times d}, \tag{2.45}$$

$$\Big||\mathcal{X}|_{F,r} - |\mathcal{Y}|_{F,r}\Big| \leq |\mathcal{X} - \mathcal{Y}|_F \quad \forall\ \mathcal{X}, \mathcal{Y} \in \mathbb{R}^{d\times d}. \tag{2.46}$$

Proof. (lemma 1) We show the monotonicity property of the mapping $\mathcal{X} \to \frac{\mathcal{X}}{|\mathcal{X}|_{F,r}}$ in $\mathbb{R}^{d\times d}$ which is a key to demonstrate the monotonicity of weak form $a_{\boldsymbol{u}}(\cdot)(\cdot,\cdot)$.

Let $\mathcal{X}, \mathcal{Y} \in \mathbb{R}^{d\times d}$ and $\zeta \in [0,1]$, we evaluate the right hand side of (2.44), add and subtract $\tau(\zeta)\frac{\mathcal{Y}}{|\mathcal{X}|_{F,r}}$, and segregate terms as

$$\Big(\tau(\zeta)\frac{\mathcal{X}}{|\mathcal{X}|_{F,r}}-\tau(\zeta)\frac{\mathcal{Y}}{|\mathcal{Y}|_{F,r}},\mathcal{X}-\mathcal{Y}\Big)=\Big(\tau(\zeta)\frac{\mathcal{X}}{|\mathcal{X}|_{F,r}}-\tau(\zeta)\frac{\mathcal{Y}}{|\mathcal{X}|_{F,r}},\mathcal{X}-\mathcal{Y}\Big) \tag{2.47}$$

$$-\Big(\tau(\zeta)\frac{\mathcal{Y}}{|\mathcal{Y}|_{F,r}}-\tau(\zeta)\frac{\mathcal{Y}}{|\mathcal{X}|_{F,r}},\mathcal{X}-\mathcal{Y}\Big). \tag{2.48}$$

Then, we manage a common denominator, and rearrange terms for (2.48)

$$\Big(\tau(\zeta)\frac{\mathcal{Y}}{|\mathcal{Y}|_{F,r}}-\tau(\zeta)\frac{\mathcal{Y}}{|\mathcal{X}|_{F,r}},\mathcal{X}-\mathcal{Y}\Big)=\Big(\tau(\zeta)\frac{|\mathcal{X}|_{F,r}\,\mathcal{Y}}{|\mathcal{Y}|_{F,r}\,|\mathcal{X}|_{F,r}}-\tau(\zeta)\frac{|\mathcal{Y}|_{F,r}\,\mathcal{Y}}{|\mathcal{Y}|_{F,r}\,|\mathcal{X}|_{F,r}},\mathcal{X}-\mathcal{Y}\Big) \tag{2.49}$$

$$=\Big(\frac{\tau(\zeta)}{|\mathcal{X}|_{F,r}}\left(|\mathcal{X}|_{F,r}-|\mathcal{Y}|_{F,r}\right)\frac{\mathcal{Y}}{|\mathcal{Y}|_{F,r}},\mathcal{X}-\mathcal{Y}\Big). \tag{2.50}$$

Now, we apply conditions (2.45) for the term $\dfrac{\mathcal{Y}}{|\mathcal{Y}|_{F,r}}$, and (2.46) for the term $|\mathcal{X}|_{F,r}-|\mathcal{Y}|_{F,r}$, on the approximated norm in (2.50), we get

$$\Big(\tau(\zeta)\frac{\mathcal{X}}{|\mathcal{X}|_{F,r}}-\tau(\zeta)\frac{\mathcal{Y}}{|\mathcal{Y}|_{F,r}},\mathcal{X}-\mathcal{Y}\Big)\geq\Big(\frac{\tau(\zeta)}{|\mathcal{X}|_{F,r}}\mathcal{X}-\mathcal{Y},\mathcal{X}-\mathcal{Y}\Big) \tag{2.51}$$

$$-\Big(\frac{\tau(\zeta)}{|\mathcal{X}|_{F,r}}\left|\mathcal{X}-\mathcal{Y}\right|_{F},\mathcal{X}-\mathcal{Y}\Big) \tag{2.52}$$

which concludes the proof

$$\Big(\tau(\zeta)\frac{\mathcal{X}}{|\mathcal{X}|_{F,r}}-\tau(\zeta)\frac{\mathcal{Y}}{|\mathcal{Y}|_{F,r}},\mathcal{X}-\mathcal{Y}\Big)\geq\ 0. \tag{2.53}$$

2.4.3 Lemma Plastic Continuity in $\mathbb{R}^{d\times d}$

Lemma 2. *(Continuity) For all $\mathcal{X},\mathcal{Y},\mathcal{Z}\in\mathbb{R}^{d\times d}$, $\zeta\in[0,1]$, and $\tau(\cdot)$ is a mapping defined as $\tau(\zeta)\colon[0,1]\to[0,\mathbb{R}^{+}]$, we have*

$$\left|\Big(\tau(\zeta)\frac{\mathcal{X}}{|\mathcal{X}|_{F,r}}-\tau(\zeta)\frac{\mathcal{Y}}{|\mathcal{Y}|_{F,r}},\mathcal{Z}\Big)\right|\leq\ 2\tau_{\infty}k\left|\mathcal{X}-\mathcal{Y}\right|_{F}\left|\mathcal{Z}\right|_{F}, \tag{2.54}$$

where, $|\cdot|_{F,r}$ is an approximation of the Frobenius norm $|\cdot|_{F}$, such that

$$\frac{1}{|\mathcal{X}|_{F,r}}\leq k\quad\forall\ \mathcal{X}\in\mathbb{R}^{d\times d}, \tag{2.55}$$

where, $k\geq 0$ is a regularization parameter.

Proof. (Lemma 2) Let $\mathcal{X},\mathcal{Y},\mathcal{Z}\in\mathbb{R}^{d\times d}$ and $\zeta\in[0,1]$, we evaluate the right hand side of (2.54), add and subtract the term $\tau(\zeta)\dfrac{\mathcal{Y}}{|\mathcal{X}|_{F,r}}$, segregate terms as

$$\Big(\tau(\zeta)\frac{\mathcal{X}}{|\mathcal{X}|_{F,r}}-\tau(\zeta)\frac{\mathcal{Y}}{|\mathcal{Y}|_{F,r}},\mathcal{Z}\Big)=\Big(\tau(\zeta)\frac{\mathcal{X}}{|\mathcal{X}|_{F,r}}-\tau(\zeta)\frac{\mathcal{Y}}{|\mathcal{X}|_{F,r}},\mathcal{Z}\Big) \tag{2.56}$$

$$-\Big(\tau(\zeta)\frac{\mathcal{Y}}{|\mathcal{Y}|_{F,r}}-\tau(\zeta)\frac{\mathcal{Y}}{|\mathcal{X}|_{F,r}},\mathcal{Z}\Big). \tag{2.57}$$

Then, we manage a common denominator, and rearrange terms, for (2.57)

$$\Big(\tau(\zeta)\frac{\mathcal{Y}}{|\mathcal{Y}|_{F,r}}-\tau(\zeta)\frac{\mathcal{Y}}{|\mathcal{X}|_{F,r}},\mathcal{Z}\Big)=\Big(\tau(\zeta)\frac{|\mathcal{X}|_{F,r}\,\mathcal{Y}}{|\mathcal{Y}|_{F,r}\,|\mathcal{X}|_{F,r}}-\tau(\zeta)\frac{|\mathcal{Y}|_{F,r}\,\mathcal{Y}}{|\mathcal{Y}|_{F,r}\,|\mathcal{X}|_{F,r}},\mathcal{Z}\Big) \tag{2.58}$$

$$=\Big(\frac{\tau(\zeta)}{|\mathcal{X}|_{F,r}}\left(|\mathcal{X}|_{F,r}-|\mathcal{Y}|_{F,r}\right)\frac{\mathcal{Y}}{|\mathcal{Y}|_{F,r}},\mathcal{Z}\Big). \tag{2.59}$$

Now, we apply the condition (2.45) and (2.46) on the approximated norm for (2.59), to obtain

$$\left|\Big(\tau(\zeta)\frac{\mathcal{X}}{|\mathcal{X}|_{F,r}}-\tau(\zeta)\frac{\mathcal{Y}}{|\mathcal{Y}|_{F,r}},\mathcal{Z}\Big)\right|\leq\Big(\frac{\tau(\zeta)}{|\mathcal{X}|_{F,r}}\,|\mathcal{X}-\mathcal{Y}|_{F}\,,\mathcal{Z}\Big) \tag{2.60}$$

$$+\Big(\frac{\tau(\zeta)}{|\mathcal{X}|_{F,r}}\,|\mathcal{X}-\mathcal{Y}|_{F}\,,\mathcal{Z}\Big), \tag{2.61}$$

then, we take the upper bound for $\tau(\cdot)$ and use the condition (2.55) for the term $\dfrac{1}{|\mathcal{X}|_{F,r}}$ on the approximated norm, to obtain

$$\left|\Big(\tau(\zeta)\frac{\mathcal{X}}{|\mathcal{X}|_{F,r}}-\tau(\zeta)\frac{\mathcal{Y}}{|\mathcal{Y}|_{F,r}},\mathcal{X}-\mathcal{Y}\Big)\right|\leq\ 2\tau_\infty k\,|\mathcal{X}-\mathcal{Y}|_{F}\,|\mathcal{Z}|_{F}\,, \tag{2.62}$$

which concludes the proof.

Now, we proceed with the proof of Proposition 1.

Proof of Proposition 1

Proof. (Proposition 1) For a given $\zeta\in\mathbb{T}$, we apply Browder-Minty Theorem of monotone operator to $a_{\boldsymbol{u}}(\cdot)(\cdot,\cdot)$ on $\mathbb{V}_0\times\mathbb{V}_0$ to show existence and uniqueness of the solution $\boldsymbol{u}=\boldsymbol{u}(\zeta)\in\mathbb{V}_0$. That is, we show that the operator $a_{\boldsymbol{u}}(\cdot)(\cdot,\cdot)$ is coercive, continuous, and monotone on $\mathbb{V}_0\times\mathbb{V}_0$, and that the operator $l_{\boldsymbol{u}}(\cdot)$ is bounded.
We start with the coerciveness property,

Coerciveness of $a_{\boldsymbol{u}}(\cdot)(\cdot,\cdot)$: For all $\boldsymbol{v}\in\mathbb{V}_0$, $\tilde{\boldsymbol{v}}:=(\boldsymbol{v},\zeta)$, we evaluate $a_{\boldsymbol{u}}(\tilde{\boldsymbol{v}})(\boldsymbol{v},\boldsymbol{v})$,

$$a_{\boldsymbol{u}}(\tilde{\boldsymbol{v}})(\boldsymbol{v},\boldsymbol{v})=\Big(2\mu(D_{\mathbb{II},r},\zeta)\mathbf{D}(\boldsymbol{v}),\mathbf{D}(\boldsymbol{v})\Big)\quad\forall\ \boldsymbol{v}\in\mathbb{V}_0, \tag{2.63}$$

then, we take into consideration the positivity of the plastic contribution, to deduce

$$a_{\boldsymbol{u}}(\tilde{\boldsymbol{v}})(\boldsymbol{v},\boldsymbol{v})\geq\ 2\Big(\eta(\zeta)\mathbf{D}(\boldsymbol{v}),\mathbf{D}(\boldsymbol{v})\Big)\quad\forall\ \boldsymbol{v}\in\mathbb{V}_0. \tag{2.64}$$

We take the lower value of $\eta(\cdot)$, and use the Korn's first inequality [61], to conclude the coerciveness of $a_{\boldsymbol{u}}(\cdot)(\cdot,\cdot)$

$$a_{\boldsymbol{u}}(\tilde{\boldsymbol{v}})(\boldsymbol{v},\boldsymbol{v})\geq\ \eta_0 C_K\,\|\boldsymbol{v}\|_1^2\quad\forall\ \boldsymbol{v}\in\mathbb{V}_0, \tag{2.65}$$

where, $\mathcal{C}_K$ denotes the Korn's inequality constant.

We proceed with the important property of continuity.

Continuity of $a_{\boldsymbol{u}}(\cdot)(\cdot,\cdot)$: For all $\boldsymbol{u},\boldsymbol{v},\boldsymbol{\eta}\in\mathbb{V}_0$, $\tilde{\boldsymbol{u}}:=(\boldsymbol{u},\zeta)$, and $\tilde{\boldsymbol{v}}:=(\boldsymbol{v},\zeta)$, we evaluate the difference $a_{\boldsymbol{u}}(\tilde{\boldsymbol{u}})(\boldsymbol{u},\boldsymbol{\eta})-a_{\boldsymbol{u}}(\tilde{\boldsymbol{v}})(\boldsymbol{v},\boldsymbol{\eta})$,

$$a_{\boldsymbol{u}}(\tilde{\boldsymbol{u}})(\boldsymbol{u},\boldsymbol{\eta})-a_{\boldsymbol{u}}(\tilde{\boldsymbol{v}})(\boldsymbol{v},\boldsymbol{\eta})=\Big(2\mu(D_{\mathrm{II},r}(\boldsymbol{u}),\zeta)\mathbf{D}(\boldsymbol{u}),\mathbf{D}(\boldsymbol{\eta})\Big)-\Big(2\mu(D_{\mathrm{II},r}(\boldsymbol{v}),\zeta)\mathbf{D}(\boldsymbol{v}),\mathbf{D}(\boldsymbol{\eta})\Big),\tag{2.66}$$

then, segregate the viscous term, and the plastic term. With the linearity of symmetric gradient $\mathbf{D}(\cdot)$, we get

$$\begin{aligned}a_{\boldsymbol{u}}(\tilde{\boldsymbol{u}})(\boldsymbol{u},\boldsymbol{\eta})-a_{\boldsymbol{u}}(\tilde{\boldsymbol{v}})(\boldsymbol{v},\boldsymbol{\eta})=&\Big(2\eta(\zeta)\mathbf{D}(\boldsymbol{u}-\boldsymbol{v}),\mathbf{D}(\boldsymbol{\eta})\Big)&(2.67)\\&+\Big(\tau(\zeta)\frac{\sqrt{2}}{\sqrt{D_{\mathrm{II},r}(\boldsymbol{u})}}\mathbf{D}(\boldsymbol{u}),\mathbf{D}(\boldsymbol{\eta})\Big)-\Big(\tau(\zeta)\frac{\sqrt{2}}{\sqrt{D_{\mathrm{II},r}(\boldsymbol{v})}}\mathbf{D}(\boldsymbol{v}),\mathbf{D}(\boldsymbol{\eta})\Big)&(2.68)\end{aligned}$$

We take the upper bound of plastic viscosity $\eta(\cdot)$, and use the Hölder inequality for the viscous term (2.67). Moreover, we use the continuity of the plastic term (2.68), using Lemma 2, to conclude the continuity of $a_{\boldsymbol{u}}(\cdot)(\cdot,\cdot)$

$$|a_{\boldsymbol{u}}(\tilde{\boldsymbol{u}})(\boldsymbol{u},\boldsymbol{\eta})-a_{\boldsymbol{u}}(\tilde{\boldsymbol{v}})(\boldsymbol{v},\boldsymbol{\eta})|\leq\Big(2\eta_\infty+2\tau_\infty k\Big)\left\|\boldsymbol{u}-\boldsymbol{v}\right\|_1\left\|\boldsymbol{\eta}\right\|_1\quad\forall\boldsymbol{u},\boldsymbol{v},\boldsymbol{\eta}\in\mathbb{V}_0,\tag{2.69}$$

The coercivity and continuity properties are not sufficient for the existence and uniqueness of the solution. Now, we check the monotonicity property of of $a_{\boldsymbol{u}}(\cdot)(\cdot,\cdot)$.

Monotonicity of $a_{\boldsymbol{u}}(\cdot)(\cdot,\cdot)$: Let $\boldsymbol{u},\boldsymbol{v}\in\mathbb{V}_0$, and set $\boldsymbol{\eta}=\boldsymbol{u}-\boldsymbol{v}$.
We evaluate the difference $a_{\boldsymbol{u}}(\tilde{\boldsymbol{u}})(\boldsymbol{u},\boldsymbol{u}-\boldsymbol{v})-a_{\boldsymbol{u}}(\tilde{\boldsymbol{v}})(\boldsymbol{v},\boldsymbol{u}-\boldsymbol{v})$, segregate the viscous term, and the plastic term, then we use the linearity of symmetric gradient $\mathbf{D}(\cdot)$, to obtain

$$\begin{aligned}a_{\boldsymbol{u}}(\tilde{\boldsymbol{u}})(\boldsymbol{u},\boldsymbol{\eta})-a_{\boldsymbol{u}}(\tilde{\boldsymbol{v}})(\boldsymbol{v},\boldsymbol{\eta})=&\Big(2\eta(\zeta)\mathbf{D}(\boldsymbol{\eta}),\mathbf{D}(\boldsymbol{\eta})\Big)&(2.70)\\&+\Big(\tau(\zeta)\frac{\sqrt{2}}{\sqrt{D_{\mathrm{II},r}(\boldsymbol{u})}}\mathbf{D}(\boldsymbol{u}),\mathbf{D}(\boldsymbol{\eta})\Big)-\Big(\tau(\zeta)\frac{\sqrt{2}}{\sqrt{D_{\mathrm{II},r}(\boldsymbol{v})}}\mathbf{D}(\boldsymbol{v}),\mathbf{D}(\boldsymbol{\eta})\Big)&(2.71)\end{aligned}$$

We take the lower bound of plastic viscosity $\eta(\cdot)$, and use the Korn's first inequality [61] for the viscous term (2.70). Moreover, we use the monotonicity of the plastic term (2.71), using Lemma 1, to obtain

$$a_{\boldsymbol{u}}(\tilde{\boldsymbol{u}})(\boldsymbol{u},\boldsymbol{\eta})-a_{\boldsymbol{u}}(\tilde{\boldsymbol{v}})(\boldsymbol{v},\boldsymbol{\eta})\geq\eta_0\mathcal{C}_K\left\|\boldsymbol{\eta}\right\|_1^2,\quad\forall\boldsymbol{u},\boldsymbol{v}\in\mathbb{V}_0\tag{2.72}$$

to conclude the proof of monotonicity property.

Furthermore, the linear operator $l_{\boldsymbol{u}}(\cdot)$ is bounded. Since, we have

$$l_{\boldsymbol{u}}(\boldsymbol{v})=\Big(\boldsymbol{f}_{\boldsymbol{u}},\boldsymbol{v}\Big)\leq\left\|\boldsymbol{f}_{\boldsymbol{u}}\right\|_0\left\|\boldsymbol{v}\right\|_1\quad\forall\boldsymbol{v}\in\mathbb{V}_0.\tag{2.73}$$

Then, with the definition of the norm for linear operators

$$\left\|l_{\boldsymbol{u}}\right\|_{\mathbb{V}_0'}=\sup_{\boldsymbol{v}\in\mathbb{V}_0}\frac{|l_{\boldsymbol{u}}(\boldsymbol{v})|}{\left\|\boldsymbol{v}\right\|_1}\quad\forall\boldsymbol{v}\in\mathbb{V}_0,\tag{2.74}$$

we obtain

$$\left\|l_{\boldsymbol{u}}\right\|_{\mathbb{V}_0'}\leq\left\|\boldsymbol{f}_{\boldsymbol{u}}\right\|_0\quad\forall\boldsymbol{v}\in\mathbb{V}_0,\tag{2.75}$$

and conclude the boundedness of the linear operator $l_{\boldsymbol{u}}(\cdot)$ in $\mathbb{V}_0$.

Now, we use the monotonicity and the continuity of $a_{\tilde{\boldsymbol{u}}}(\cdot)(\cdot,\cdot)$ in $\mathbb{V}_0 \times \mathbb{V}_0$, and the continuity of the linear operator $l_{\boldsymbol{u}}(\cdot)$ to conclude the existence and uniqueness of a solution $\boldsymbol{u} = \boldsymbol{u}(\zeta) \in \mathbb{V}_0$ to the viscoplastic subproblem. Moreover, we use the coercivity of $a_{\tilde{\boldsymbol{u}}}(\cdot)(\cdot,\cdot)$ in $\mathbb{V}_0 \times \mathbb{V}_0$ and the continuity of the linear operator $l_{\boldsymbol{u}}(\cdot)$, to deduce that the solution is bounded with respect to data. Indeed, from the coerciveness of $a_{\boldsymbol{u}}(\cdot)(\cdot,\cdot)$ (2.65), we get

$$\eta_0 \mathcal{C}_K \left\|\boldsymbol{u}\right\|_1^2 \leq a_{\tilde{\boldsymbol{u}}}(\tilde{\boldsymbol{u}})(\boldsymbol{u},\boldsymbol{u}) = l_{\boldsymbol{u}}(\boldsymbol{u}), \tag{2.76}$$

and from the continuity of the linear operator $l_{\boldsymbol{u}}(\cdot)$ (2.75), we obtain

$$\eta_0 \mathcal{C}_K \left\|\boldsymbol{u}\right\|_1^2 \leq \ \left\|\boldsymbol{f}_{\boldsymbol{u}}\right\|_0 \left\|\boldsymbol{u}\right\|_1 . \tag{2.77}$$

Thus, the boundedness of the solution with data

$$\left\|u\right\|_1 \leq \ \frac{1}{\eta_0 \mathcal{C}_K} \left\|\boldsymbol{f}_{\boldsymbol{u}}\right\|_0 . \tag{2.78}$$

Let us introduce the space of bounded solution that we denote by $\mathcal{BS}_{\mathcal{VP}}$.

Definition 1. *For $r_{\boldsymbol{u}} \in \mathbb{R}^+$ such that $r_{\boldsymbol{u}} = \dfrac{\left\|\boldsymbol{f}_{\boldsymbol{u}}\right\|_0}{\eta_0 \mathcal{C}_K}$, we define the space of bounded solution, $\mathcal{BS}_{\mathcal{VP}}$, as*

$$\mathcal{BS}_{\mathcal{VP}} = \{\boldsymbol{v} \in \mathbb{V}_0 \mid \ \left\|\boldsymbol{v}\right\|_1 \leq \ r_{\boldsymbol{u}}\} . \tag{2.79}$$

The existence of the pressure is due to Lagrange multiplier argument. Indeed, let us consider the problem

$$\mathcal{LM}_{\boldsymbol{u}}(\boldsymbol{v}) = \langle \boldsymbol{f}_{\boldsymbol{u}}, \boldsymbol{v}\rangle - a_{\boldsymbol{u}}(\tilde{\boldsymbol{u}})(\boldsymbol{u},\boldsymbol{v}), \quad \forall \boldsymbol{v} \in \mathbb{V}. \tag{2.80}$$

Thus, $\mathcal{LM}_{\boldsymbol{u}}(\boldsymbol{v}) = 0$ on $\mathbb{V}_0 = \ker \mathcal{B}$, which imply that $\mathcal{LM}_{\boldsymbol{u}} \in \operatorname{Im} \mathcal{B}$. That is, there exist a $p \in \mathbb{Q}$ such that

$$\mathcal{LM}_{\boldsymbol{u}}(\boldsymbol{v}) = b(\boldsymbol{v},p), \quad \forall \boldsymbol{v} \in \mathbb{V}. \tag{2.81}$$

Then, using the LBB condition, we have

$$\left\|p\right\|_{\mathbb{Q}/\ker \mathcal{B}^{\mathrm{T}}} \leq \frac{1}{\beta} \sup_{\boldsymbol{v}\in\mathbb{V}} \frac{b(\boldsymbol{v},p)}{\left\|\boldsymbol{v}\right\|_{\mathbb{V}}}, \tag{2.82}$$

where, β is the Ladyzhenskaya-Babuška-Brezzi (LBB) constant. With the surjectivity of $\mathcal{B}$ (2.81), we get

$$\left\|p\right\|_{\mathbb{Q}/\ker \mathcal{B}^{\mathrm{T}}} \leq \frac{1}{\beta} \left\|\mathcal{LM}_{\boldsymbol{u}}\right\|_{\mathbb{V}'} . \tag{2.83}$$

From the Lagrange multiplier definition (2.80), and the boundedness of velocity $\boldsymbol{u}$, we have the estimate

$$\left\|\mathcal{LM}_{\boldsymbol{u}}\right\|_{\mathbb{V}'} \leq \Big(1 + \frac{\left\|a_{\boldsymbol{u}}\right\|}{\eta_0 \mathcal{C}_K}\Big) \left\|\boldsymbol{f}_{\boldsymbol{u}}\right\|_0 , \tag{2.84}$$

where $\left\|a_{\boldsymbol{u}}\right\|$ denote the upper bound of the operator $a_{\boldsymbol{u}}(\cdot)(\cdot,\cdot)$, that is

$$\left\|a_{\boldsymbol{u}}\right\| \leq 2\left(\eta_\infty + k\tau_\infty\right). \tag{2.85}$$

Then,

$$\left\|p\right\|_0 \leq \frac{1}{\beta}\Big(1 + \frac{2\left(\eta_\infty + k\tau_\infty\right)}{\eta_0 \mathcal{C}_K}\Big) \left\|\boldsymbol{f}_{\boldsymbol{u}}\right\|_0 , \tag{2.86}$$

This concludes the proof of proposition 1.

2.4.4 Well-posedness of Microstructure Subproblem

In connection with our TVP problem, we adopt the formulation of microstructure subproblem with respect to H^1 space similar to [55]. For alternative formulation we refer to [2, 52, 43]. The microstructure subproblem for a given divergence-free velocity is a bilinear form with respect to microstructure field. For the existence and uniqueness of solution of microstructure subproblem (2.39), we demonstrate that the bilinear form $a_\lambda(\tilde{\boldsymbol{u}})(\cdot,\cdot)$ is positive bounded below and continuous, and the linear operator $l_\lambda(\cdot)$ is continuous.

Proof of Proposition 2

Proof. (Proposition 2) For every $\boldsymbol{u} \in \mathbb{V}_0$, $\xi \in \mathbb{T}$, and $\tilde{\boldsymbol{u}} := (\boldsymbol{u}, \xi)$, firstly, we demonstrate that the bilinear form $a_\lambda(\tilde{\boldsymbol{u}})(\cdot,\cdot)$ is positive bounded weakly from below. That is, the bilinear form $a_\lambda(\tilde{\boldsymbol{u}})(\cdot,\cdot)$ can not be bounded from below with the complete norm of the space $\mathbb{T}$. We refer to this property as "coercivity" in a weak norm.

Coerciveness in weak norm of $a_\lambda(\tilde{\boldsymbol{u}})(\cdot,\cdot)$: Let $\xi \in \mathbb{T}$, we have

$$a_\lambda(\tilde{\boldsymbol{u}})(\xi,\xi) = \Big(\mathcal{M}(D_{\mathbb{II},r},\xi),\xi\Big) - \Big(\xi, \boldsymbol{u}\cdot\nabla\xi\Big) + \langle\xi,\xi\rangle_+ \quad \forall\ \xi \in \mathbb{T}. \tag{2.87}$$

Then, we integrate by part of the convective term, to have

$$a_\lambda(\tilde{\boldsymbol{u}})(\xi,\xi) = \Big(\mathcal{M}(D_{\mathbb{II},r},\xi),\xi\Big) + \Big(\xi, \boldsymbol{u}\cdot\nabla\xi\Big) - \langle\xi,\xi\rangle_+ + \langle\xi,\xi\rangle_- + \langle\xi,\xi\rangle_+ \quad \forall\ \xi \in \mathbb{T}. \tag{2.88}$$

From (2.87) and (2.88), by summing up (2.87) and (2.88), we deduce

$$a_\lambda(\tilde{\boldsymbol{u}})(\xi,\xi) = \Big(\mathcal{M}(D_{\mathbb{II},r},\xi),\xi\Big) + \frac{1}{2}\left\{<\xi>_-^2 + <\xi>_+^2\right\} \quad \forall\ \xi \in \mathbb{T}. \tag{2.89}$$

We use the definition of thixotropy model $\mathcal{M}(\cdot,\cdot)$ to split the breakdown and the buildup contribution in the bilinear form as

$$a_\lambda(\tilde{\boldsymbol{u}})(\xi,\xi) = \Big(\mathcal{M}_a\ \xi,\xi\Big) + \Big(\mathcal{M}_b\sqrt{D_{\mathbb{II},r}(\boldsymbol{u})}\ \xi,\xi\Big) + \frac{1}{2}\left\{<\xi>_-^2 + <\xi>_+^2\right\} \quad \forall\ \xi \in \mathbb{T}. \tag{2.90}$$

Since the breakdown contribution is positive, we obtain the below bound

$$a_\lambda(\tilde{\boldsymbol{u}})(\xi,\xi) \geq \mathcal{M}_a\,\|\xi\|_0^2 + \frac{1}{2}\left\{<\xi>_-^2 + <\xi>_+^2\right\} \quad \forall\ \xi \in \mathbb{T}, \tag{2.91}$$

using the positivity of buildup parameter $\mathcal{M}_a$. With the positivity of the boundary norm, we obtain

$$a_\lambda(\tilde{\boldsymbol{u}})(\xi,\xi) \geq \mathcal{M}_a\,\|\xi\|_0^2 \quad \forall\ \xi \in \mathbb{T}. \tag{2.92}$$

Hence, with the assumption on the buildup, $\mathcal{M}_a > 0$, the bilinear form is positive and bounded from below.

Remark 1. For the case that the buildup parameter vanishes, that is $\mathcal{M}_a = 0$, we can use the lower bound with the boundary norm to proof instead the positive definiteness of $a_\lambda(\tilde{\boldsymbol{u}})(\cdot,\cdot)$, for specified physical systems.

We continue our proof steps to investigate the continuity. As the operator $a_\lambda(\tilde{\boldsymbol{u}})(\cdot,\cdot)$ is a bilinear form, for a given $\boldsymbol{u} \in \mathbb{V}_0$, the continuity and the boundedness are equivalent.

Continuity of $a_\lambda(\tilde{\boldsymbol{u}})(\cdot,\cdot)$: Let $\lambda, \xi \in \mathbb{T}$, we evaluate $|a_\lambda(\tilde{\boldsymbol{u}})(\cdot,\cdot)|$ to obtain

$$|a_\lambda(\tilde{\boldsymbol{u}})(\lambda,\xi)| \leq \left|\Big(\mathcal{M}_a\lambda,\xi\Big)\right| + \left|\Big(\mathcal{M}_b\sqrt{D_{\mathbb{I},r}(\boldsymbol{u})}\lambda,\xi\Big)\right| + \left|\Big(\lambda,\boldsymbol{u}\cdot\nabla\xi\Big)\right| + \left|\langle\lambda,\xi\rangle_+\right| \quad \forall\xi\in\mathbb{T}. \tag{2.93}$$

We use (L^∞, L^2, L^2) Hölder's inequality for the second and third terms in (2.93), we get

$$|a_\lambda(\tilde{\boldsymbol{u}})(\lambda,\xi)| \leq \mathcal{M}_a \|\lambda\|_0 \|\xi\|_0 + \mathcal{M}_b |\mathbf{D}(\boldsymbol{u})|_\infty \|\lambda\|_0 \|\xi\|_0 + |\boldsymbol{u}|_\infty \|\lambda\|_0 \|\xi\|_1 + <\lambda>_+^{\frac{1}{2}} <\xi>_+^{\frac{1}{2}} \tag{2.94}$$

Then, with the boundedness of zero norm and boundary norm with the one norm, we obtain

$$|a_\lambda(\tilde{\boldsymbol{u}})(\lambda,\xi)| \leq \Big(1 + \mathcal{M}_a + \mathcal{M}_b |\boldsymbol{u}|_{1,\infty} + |\boldsymbol{u}|_\infty\Big) \|\lambda\|_1 \|\xi\|_1 , \tag{2.95}$$

which concludes the continuity of $a_\lambda(\tilde{\boldsymbol{u}})(\cdot,\cdot)$ in the complete norm of the space $\mathbb{T}$.

Remark 2. The lower norm bound for $a_\lambda(\tilde{\boldsymbol{u}})(\cdot,\cdot)$ related to "coercivity" and upper norm bound for $a_\lambda(\tilde{\boldsymbol{u}})(\cdot,\cdot)$ related to continuity do not match.

Now, we proceed with the boundedness of $l_\lambda(\cdot)$.

Continuity of $l_\lambda(\cdot)$: Let $\lambda, \xi \in \mathbb{T}$, we evaluate $l_\lambda(\xi)$, use Hölder's inequality, to have the estimate

$$l_\lambda(\xi) = \Big(f_\lambda, \xi\Big) \leq \|f_\lambda\|_0 \|\xi\|_0 \leq \|f_\lambda\|_0 \|\xi\|_1 \quad \forall\xi\in\mathbb{T}. \tag{2.96}$$

Thus, the boundedness of $l_\lambda(\cdot)$.

The conditions for existence and uniqueness are satisfied, that is, $a_\lambda(\tilde{\boldsymbol{u}})(\cdot,\cdot)$ is positive bounded below (coerciveness in a weak norm), the bilinear $a_\lambda(\tilde{\boldsymbol{u}})(\cdot,\cdot)$ is continuous (bounded above with the complete norm), and the linear $l_\lambda(\cdot)$ is bounded. Then, there exists a unique solution $\lambda(\boldsymbol{u}) \in \mathbb{T}$ of the microstrucutre subproblem (2.39). Moreover, the solution is bounded with data. We use the coercivity of $a_\lambda(\tilde{\boldsymbol{u}})(\cdot,\cdot)$ (2.91), to have

$$\mathcal{M}_a \|\lambda\|_0^2 + \frac{1}{2}\langle\lambda\rangle^2 \leq \ a_\lambda(\tilde{\boldsymbol{u}})(\lambda,\lambda). \tag{2.97}$$

With the continuity of $l_\lambda(\cdot)$ (2.96), we get

$$a_\lambda(\tilde{\boldsymbol{u}})(\lambda,\lambda) = \ l_\lambda(\lambda) \leq \ \|f_\lambda\|_0 \|\lambda\|_0 . \tag{2.98}$$

We use the positivity of the boundary norm and the strict positivity of $\mathcal{M}_a$, on one hand, to have the estimate

$$\|\lambda\|_0 \leq \frac{1}{\mathcal{M}_a} \|f_\lambda\|_0 . \tag{2.99}$$

On other hand, we keep the general estimate

$$\mathcal{M}_a \|\lambda\|_0^2 + \frac{1}{2}\langle\lambda\rangle^2 \leq \frac{1}{\mathcal{M}_a} \|f_\lambda\|_0^2 . \tag{2.100}$$

Both estimates (2.99) and (2.100) express the continuous behavior of the microstructure solution on the data.

Remark 3. The boundedness of $a_\lambda(\tilde{\boldsymbol{u}})(\cdot,\cdot)$ from below by the L_2-norm and the boundary norms is a considerably weaker condition with respect to $\|\cdot\|_1$-norm which is the norm considered for the microstructure space $\mathbb{T}$.

Now, we introduce the space of bounded solutions of microstructure subproblem (2.39), which we denote by $\mathcal{BS}_{\mathcal{T}}$.

Definition 2. *For $r_\lambda \in \mathbb{R}^+$ such that $r_\lambda = \dfrac{\|\boldsymbol{f}_\lambda\|_0^2}{\mathcal{M}_a}$, we define the space of bounded microstructure solutions, $\mathcal{BS}_{\mathcal{T}}$, as*

$$\mathcal{BS}_{\mathcal{T}} = \left\{ \xi \in \mathbb{T} \mid \mathcal{M}_a \|\xi\|_0^2 + \frac{1}{2}\langle \xi \rangle^2 \leq \ r_\lambda \right\}. \tag{2.101}$$

We proceed with the investigation of the well-posedness of the coupled thixoviscoplastic problem.

2.4.5 Well-posedness of the Coupled Thixoviscoplastic Problem

The coupled thixoviscoplastic problem is multifield coupling. A straightforward way to demonstrate the well-posedness of multifield coupling is to construct a mapping acting on a set of admissible solutions and show the applicability of fixed point solution. We proceed in this context, to check the existence of fixed point solution.
Firstly, we introduce the convex set for the coupled field of bounded solutions, denoted by $\mathcal{BS}_{\mathcal{TVP}}$, a cross product set of bounded solution for viscoplastic subproblem, $\mathcal{BS}_{\mathcal{VP}}$, for a given microstructure (2.38), and bounded solution for microstructure subproblem, $\mathcal{BS}_{\mathcal{T}}$, for a given velocity (2.39), defined as

$$\mathcal{BS}_{\mathcal{TVP}} = \mathcal{BS}_{\mathcal{VP}} \times \mathcal{BS}_{\mathcal{T}}, \tag{2.102}$$

that is,

$$\mathcal{BS}_{\mathcal{TVP}} = \left\{ \tilde{\boldsymbol{\eta}} = (\boldsymbol{w}, \zeta) \in \mathbb{W}_0 = \mathbb{V}_0 \times \mathbb{T} \mid \|\boldsymbol{w}\|_1 \leq \ r_{\boldsymbol{u}},\ \mathcal{M}_a \|\zeta\|_0^2 + \frac{1}{2}\langle \zeta \rangle^2 \leq \ r_\lambda \right\}. \tag{2.103}$$

Secondly, we consider the mapping $\mathcal{TVP}$ from $\mathcal{BS}_{\mathcal{TVP}}$ to $\mathcal{BS}_{\mathcal{TVP}}$, defined as,

$$\tilde{\boldsymbol{u}} = \mathcal{TVP}(\tilde{\boldsymbol{\eta}}) \quad \forall\ \tilde{\boldsymbol{\eta}} \in \mathcal{BS}_{\mathcal{TVP}}. \tag{2.104}$$

We show that $\mathcal{TVP}$ admits a fixed point solution

$$\tilde{\boldsymbol{u}} = \mathcal{TVP}(\tilde{\boldsymbol{u}}). \tag{2.105}$$

We relate the mapping $\mathcal{TVP}$ to the coupled operator $\mathcal{A}_{\tilde{\boldsymbol{u}}}$, as follows

$$\mathcal{TVP} = \mathcal{A}_{\tilde{\boldsymbol{u}}} - \mathcal{A}_0. \tag{2.106}$$

$\mathcal{A}_0$ is the operator of the decoupled part of the thixotropic and viscoplastic equations which is completely continuous. Indeed, $\mathcal{A}_0$ is a self mapping in the closed bounded convex set $\mathcal{BS}_{\mathcal{TVP}}$. And the operator $\mathcal{TVP}$ is the coupled part of the thixotropic and viscoplastic equations (full thixotropic TVP) which is nonlinear contraction. In the following Corollary 1, we state that the operator $\mathcal{TVP}(\cdot)$ is a nonlinear contraction [17, 60].

Corollary 1. *The mapping $\tilde{\boldsymbol{\eta}} \to \mathcal{TVP}(\tilde{\boldsymbol{\eta}})$ is a nonlinear contraction in $\mathcal{BS}_{\mathcal{TVP}}$. That is,*

$$\|\mathcal{TVP}(\tilde{\boldsymbol{u}}) - \mathcal{TVP}(\tilde{\boldsymbol{v}})\|_1 \leq \ \phi(\|\tilde{\boldsymbol{u}} - \tilde{\boldsymbol{v}}\|_1) \quad \forall\ \tilde{\boldsymbol{u}}, \tilde{\boldsymbol{v}} \in \mathcal{BS}_{\mathcal{TVP}}, \tag{2.107}$$

where ϕ is positive real-valued continuous function, such that

$$\phi(r) < r \quad \text{for } r > 0. \tag{2.108}$$

Proof (Corollary 1).
Using the continuity expression of the operator $\mathcal{A}_{\tilde{\boldsymbol{u}}}$ from Proposition 3, we deduce that $\mathcal{TVP}(\cdot)$ is a nonlinear contraction on $\mathcal{BS}_{\mathcal{TVP}}$. The condition (2.108) on ϕ is obtained with the appropriate choice on data, which conclude the proof.

Remark 4. Here, in order to give the reader a better understanding by means of a close explicit "equivalent" expression of ϕ, we expand the boundaries term for the microstructure operator in Proposition 3

$$|a_\lambda(\tilde{\boldsymbol{u}})(\lambda,\zeta) - a_\lambda(\tilde{\boldsymbol{u}})(\xi,\zeta)| \leq \Big(\mathcal{M}_a + (\mathcal{M}_b+1)\,|\boldsymbol{u}|_{1,\infty}\Big)\,\|\lambda-\xi\|_0\,\|\zeta\|_1 + \langle|\boldsymbol{u}\cdot\boldsymbol{n}|\,\lambda-\xi\rangle_+\,\|\zeta\|_1 \tag{2.109}$$

$$+\Big(\mathcal{M}_b+1\Big)\,\|\xi\|_0\,\|\boldsymbol{u}-\boldsymbol{v}\|_{1,\infty}\,\|\zeta\|_1 + \langle|(\boldsymbol{u}-\boldsymbol{v})\cdot\boldsymbol{n}|\,\xi\rangle_+\,\|\zeta\|_1\,. \tag{2.110}$$

For the boundary term in (2.109) and (2.110), we use the Hölder's inequality, then trace inequality for velocity and microstructure alike for the term in (2.109), and trace inequality for velocity term only for the term in (2.110), to obtain

$$|a_\lambda(\tilde{\boldsymbol{u}})(\lambda,\zeta) - a_\lambda(\tilde{\boldsymbol{u}})(\xi,\zeta)| \leq \Big(\mathcal{M}_a + (\mathcal{M}_b+1)\,|\boldsymbol{u}|_{1,\infty}\Big)\,\|\lambda-\xi\|_0\,\|\zeta\|_1 + \mathcal{C}_{\rm tri}\,\|\boldsymbol{u}\|_{0,\infty}\,\|\lambda-\xi\|_1\,\|\zeta\|_1 \tag{2.111}$$

$$+\Big(\mathcal{M}_b+1\Big)\,\|\xi\|_0\,\|\boldsymbol{u}-\boldsymbol{v}\|_{1,\infty}\,\|\zeta\|_1 + \mathcal{C}_{\rm tri}\,\|\boldsymbol{u}-\boldsymbol{v}\|_{1,\infty}\,\langle\xi\rangle_+\,\|\zeta\|_1 \tag{2.112}$$

Then, we get an explicit expression as

$$\phi(r) = \mathcal{C}(|\boldsymbol{u}|_{1,\infty}, |\boldsymbol{v}|_{1,\infty}, \|\xi\|_{0,\infty}, \langle\xi\rangle_+, \|\lambda\|_{0,\infty})r, \tag{2.113}$$

where $\mathcal{C}$ is given as follows

$$\begin{aligned}\mathcal{C} =& \Big((2\eta_\infty\,\|\lambda\|_{0,\infty}) + (\tau_\infty(\|\lambda\|_{0,\infty}+\|\xi\|_{0,\infty})k\Big)^2 \\ &+ \Big(2\eta_\infty\,|\boldsymbol{v}|_{1,\infty} + \tau_\infty k\,|\boldsymbol{v}|_{1,\infty}\Big)^2 + \Big(\mathcal{M}_b+1\Big)\,|\boldsymbol{u}|_{1,\infty} + \mathcal{C}_{\rm tri}\,\|\boldsymbol{u}\|_{0,\infty}\Big)^2 \\ &+ \Big((\mathcal{M}_b+1)\,\|\xi\|_0 + \mathcal{C}_{\rm tri}\langle\xi\rangle_+\Big)^2.\end{aligned} \tag{2.114}$$

Clearly, the condition (2.108) on ϕ is satisfied with the appropriate choice on data.

We proceed with checking the continuity of $a_{\tilde{\boldsymbol{u}}}(\cdot)(\cdot,\cdot)$, which we state in Proposition 3.

Proposition 3 (Continuity). *For all $\tilde{\boldsymbol{u}} = (\boldsymbol{u},\lambda), \tilde{\boldsymbol{v}} = (\boldsymbol{v},\xi), \tilde{\boldsymbol{\eta}} = (\boldsymbol{\eta},\zeta) \in \mathbb{W}_0$, we have*

$$\begin{aligned}|a_{\boldsymbol{u}}(\tilde{\boldsymbol{u}})(\boldsymbol{u},\boldsymbol{\eta}) - a_{\boldsymbol{u}}(\tilde{\boldsymbol{v}})(\boldsymbol{v},\boldsymbol{\eta})| \leq& \Big((2\eta_0 + 2\eta_\infty\,\|\lambda\|_{0,\infty}) + (2\tau_0 + \tau_\infty(\|\lambda\|_{0,\infty}+\|\xi\|_{0,\infty})k)\Big)\,\|\boldsymbol{u}-\boldsymbol{v}\|_1\,\|\boldsymbol{\eta}\|_1 \\ &+ \Big(2\eta_\infty\,|\boldsymbol{v}|_{1,\infty} + \tau_\infty k\,|\boldsymbol{v}|_{1,\infty}\Big)\,\|\lambda-\xi\|_0\,\|\boldsymbol{\eta}\|_1\,.\end{aligned} \tag{2.115}$$

$$\begin{aligned}|a_\lambda(\tilde{\boldsymbol{u}})(\lambda,\zeta) - a_\lambda(\tilde{\boldsymbol{u}})(\xi,\zeta)| \leq& \Big(\mathcal{M}_a + (\mathcal{M}_b+1)\,|\boldsymbol{u}|_{1,\infty}\Big)\,\|\lambda-\xi\|_0\,\|\zeta\|_1 + \langle|\boldsymbol{u}\cdot\boldsymbol{n}|\,\lambda-\xi\rangle_+\,\|\zeta\|_1 \\ &+\Big(\mathcal{M}_b+1\Big)\,\|\xi\|_0\,\|\boldsymbol{u}-\boldsymbol{v}\|_{1,\infty}\,\|\zeta\|_1 + \langle|(\boldsymbol{u}-\boldsymbol{v})\cdot\boldsymbol{n}|\,\xi\rangle_+\,\|\zeta\|_1\,.\end{aligned} \tag{2.116}$$

For a detailed proof, we first introduce a lemma related the continuity of the coupled thixoviscoplastic problem in $\mathbb{R}^{d\times d}$.

2.4.6 Lemma Multifield Function Continuity in $\mathbb{R} \times \mathbb{R}^{d\times d}$

Lemma 3. *(Continuity) For all* $\mathfrak{X}, \mathcal{Y} \in B(0, r_{\boldsymbol{u}}) \subset \mathbb{R}^{d\times d}$, $\mathfrak{Z} \in \mathbb{R}^{d\times\, d}$, $\xi, \zeta, \chi \in [0,1]$, *and* $\tau(\cdot)$ *is a mapping defined as* $\tau\colon [0,1] \to [0, \mathbb{R}^+]$, *we have*

$$\left|\Big(\eta(\xi)\mathfrak{X} - \eta(\zeta)\mathcal{Y}, \mathfrak{Z}\Big)\right| \leq \Big((\eta_0 + \eta_\infty\,|\xi|)\,|\mathfrak{X} - \mathcal{Y}|_F + \eta_\infty\,|\mathcal{Y}|_F\,|\xi - \zeta|\Big)\,|\mathfrak{Z}|_F\,, \tag{2.117}$$

$$\left|\Big(\tau(\xi)\frac{\mathfrak{X}}{|\mathfrak{X}|_{F,r}} - \tau(\zeta)\frac{\mathcal{Y}}{|\mathcal{Y}|_{F,r}}, \mathfrak{Z}\Big)\right| \leq \Big((2\tau_0 + \tau_\infty(|\xi| + |\zeta|))k\,|\mathfrak{X} - \mathcal{Y}|_F + \tau_\infty k\,|\xi - \zeta|\,|\mathcal{Y}|_F\Big)\,|\mathfrak{Z}|_F\,, \tag{2.118}$$

$$\left|\Big(\xi\,|\mathfrak{X}|_F - \zeta\,|\mathcal{Y}|_F\,, \chi\Big)\right| \leq \Big(\,|\xi|\,|\mathfrak{X} - \mathcal{Y}|_F + |\xi - \zeta|\,|\mathcal{Y}|_F\Big)\,|\chi|\,. \tag{2.119}$$

Proof. (Lemma 3) let $\mathfrak{X}, \mathcal{Y} \in B(0, r_{\boldsymbol{u}}) \subset \mathbb{R}^{d\times d}$, $\mathfrak{Z} \in \mathbb{R}^{d\times\, d}$, and $\xi, \zeta \in [0,1]$,

Microstructure-viscous term We evaluate the left hand side of (2.117), and add and subtract the term $\eta(\xi)\mathcal{Y}$, to obtain

$$\Big(\eta(\xi)\mathfrak{X} - \eta(\zeta)\mathcal{Y}, \mathfrak{Z}\Big) = \Big(\eta(\xi)\,(\mathfrak{X} - \mathcal{Y})\,, \mathfrak{Z}\Big) + \Big(\,(\eta(\xi) - \eta(\zeta))\,\mathcal{Y}, \mathfrak{Z}\Big). \tag{2.120}$$

Then, we use Hölder's inequality, take an upper bound of $\eta(\cdot)$ for the first term of right hand side of equality (2.120), and simply we use the definition of $\eta(\cdot)$ for the second term of right hand side of equality (2.120), to obtain

$$\left|\Big(\eta(\xi)\mathfrak{X} - \eta(\zeta)\mathcal{Y}, \mathfrak{Z}\Big)\right| \leq \Big((\eta_0 + \eta_\infty\,|\xi|)\,|\mathfrak{X} - \mathcal{Y}|_F + \eta_\infty\,|\mathcal{Y}|_F\,|\xi - \zeta|\Big)\,|\mathfrak{Z}|_F\,. \tag{2.121}$$

This conclude the auxiliary result of continuity of multifield microstructure-viscous function.

Microstructure-plastic term We evaluate the left hand side of (2.118), add and subtract the term $\tau(\xi)\dfrac{\mathcal{Y}}{|\mathfrak{X}|_{F,r}}$, segregate terms as

$$\Big(\tau(\xi)\frac{\mathfrak{X}}{|\mathfrak{X}|_{F,r}} - \tau(\zeta)\frac{\mathcal{Y}}{|\mathcal{Y}|_{F,r}}, \mathfrak{Z}\Big) = \Big(\tau(\xi)\frac{\mathfrak{X}}{|\mathfrak{X}|_{F,r}} - \tau(\xi)\frac{\mathcal{Y}}{|\mathfrak{X}|_{F,r}}, \mathfrak{Z}\Big) \tag{2.122}$$

$$+ \Big(\tau(\xi)\frac{\mathcal{Y}}{|\mathfrak{X}|_{F,r}} - \tau(\zeta)\frac{\mathcal{Y}}{|\mathcal{Y}|_{F,r}}, \mathfrak{Z}\Big). \tag{2.123}$$

We manage a common denominator for the term (2.123), and rearrange terms as

$$\Big(\tau(\xi)\frac{\mathcal{Y}}{|\mathfrak{X}|_{F,r}} - \tau(\zeta)\frac{\mathcal{Y}}{|\mathcal{Y}|_{F,r}}, \mathfrak{Z}\Big) = \Big(\tau(\xi)\frac{|\mathcal{Y}|_{F,r}\,\mathcal{Y}}{|\mathcal{Y}|_{F,r}\,|\mathfrak{X}|_{F,r}} - \tau(\zeta)\frac{|\mathfrak{X}|_{F,r}\,\mathcal{Y}}{|\mathcal{Y}|_{F,r}\,|\mathfrak{X}|_{F,r}}, \mathfrak{Z}\Big) \tag{2.124}$$

$$= \Big(\frac{1}{|\mathfrak{X}|_{F,r}}\Big(\tau(\xi)\,|\mathcal{Y}|_{F,r} - \tau(\zeta)\,|\mathfrak{X}|_{F,r}\Big)\frac{\mathcal{Y}}{|\mathcal{Y}|_{F,r}}, \mathfrak{Z}\Big), \tag{2.125}$$

then, add and subtract the term $\tau(\zeta)\,|\mathcal{Y}|_{F,r}$ for the term $\tau(\xi)\,|\mathcal{Y}|_{F,r} - \tau(\zeta)\,|\mathfrak{X}|_{F,r}$, in (2.125) as

$$\tau(\xi)\,|\mathcal{Y}|_{F,r} - \tau(\zeta)\,|\mathfrak{X}|_{F,r} = (\tau(\xi) - \tau(\zeta))\,|\mathcal{Y}|_{F,r} - \tau(\zeta)(|\mathfrak{X}|_{F,r} - |\mathcal{Y}|_{F,r}), \tag{2.126}$$

to obtain

$$\Big(\tau(\xi)\frac{\mathfrak{X}}{|\mathfrak{X}|_{F,r}} - \tau(\zeta)\frac{\mathcal{Y}}{|\mathcal{Y}|_{F,r}}, \mathfrak{Z}\Big) = \Big(\frac{\tau(\xi)}{|\mathfrak{X}|_{F,r}}\mathfrak{X} - \mathcal{Y}, \mathfrak{Z}\Big) - \Big(\frac{\tau(\zeta)}{|\mathfrak{X}|_{F,r}}\Big(|\mathfrak{X}|_{F,r} - |\mathcal{Y}|_{F,r}\Big)\frac{\mathcal{Y}}{|\mathcal{Y}|_{F,r}}, \mathfrak{Z}\Big) \tag{2.127}$$

$$+ \Big(\frac{\tau(\xi) - \tau(\zeta)}{|\mathfrak{X}|_{F,r}}\mathcal{Y}, \mathfrak{Z}\Big) \tag{2.128}$$

Now, we apply the conditions on the approximation norm, (2.45) for the term $\dfrac{\mathcal{Y}}{|\mathcal{Y}|_{F,r}}$, (2.46) for the term $|\mathcal{X}|_{F,r} - |\mathcal{Y}|_{F,r}$, in (2.127), and (2.55) for the term $\dfrac{1}{|\mathcal{X}|_{F,r}}$ in (2.127) and (2.128), and we take an upper bound of $\tau(\cdot)$ in (2.127), to obtain

$$\begin{aligned}\left|\Big(\tau(\xi)\frac{\mathcal{X}}{|\mathcal{X}|_{F,r}} - \tau(\zeta)\frac{\mathcal{Y}}{|\mathcal{Y}|_{F,r}}, \mathcal{X}-\mathcal{Y}\Big)\right| \leq (2\tau_0 + \tau_\infty(|\xi|+|\zeta|))k\,|\mathcal{X}-\mathcal{Y}|_F\,|\mathcal{Z}|_F \\ + \tau_\infty k\,|\mathcal{Y}|_F\,|\xi-\zeta|\,|\mathcal{Z}|_F\,,\end{aligned} \tag{2.129}$$

which conclude the continuity of multifield microstructure-plastic function (2.118).

Microstructure-breakdown term We evaluate the left hand side of (2.117), add and subtract the term $\xi\,|\mathcal{Y}|_F$, to obtain

$$\Big(\xi\,|\mathcal{X}|_F - \zeta\,|\mathcal{Y}|_F\,,\chi\Big) = \Big(\xi(|\mathcal{X}|_F - |\mathcal{Y}|_F),\chi\Big) + \Big((\xi-\zeta)\,|\mathcal{Y}|_F\,,\chi\Big). \tag{2.130}$$

We use Hölder's inequality, and the inverse inequality on the norm $|\cdot|_F$, to obtain

$$\left|\Big(\xi\,|\mathcal{X}|_F - \zeta\,|\mathcal{Y}|_F\,,\mathcal{Z}\Big)\right| = \Big(\,|\xi|\,|\mathcal{X}-\mathcal{Y}|_F + |\xi-\zeta|\,|\mathcal{Y}|_F\,\Big)\,|\chi|\,. \tag{2.131}$$

After concluding the auxiliary results of the continuity of multivalued functions in $\mathbb{R}\times\mathbb{R}^{d\times d}$, microstructure-viscosity, microstructure-plastic, and microstructure-buildup, we proceed with the continuity of the operator $a_{\tilde{\boldsymbol{u}}}(\cdot)(\cdot,\cdot)$.

We proceed with the investigation of the mapping $\mathcal{TVP}(\cdot)$ via the property of continuity of the coupled operator $a_{\tilde{\boldsymbol{u}}}(\cdot)(\cdot,\cdot)$.

Proof of Continuity Proposition 3

The coupled form $a_{\tilde{\boldsymbol{u}}}(\cdot)(\cdot,\cdot)$ is an additive form of $a_{\boldsymbol{u}}(\cdot)(\cdot,\cdot)$ and $a_\lambda(\cdot)(\cdot,\cdot)$. Thus, the continuity of $a_{\tilde{\boldsymbol{u}}}(\cdot)(\cdot,\cdot)$ is due to continuity of the forms $a_{\boldsymbol{u}}(\cdot)(\cdot,\cdot)$ and $a_\lambda(\cdot)(\cdot,\cdot)$.

Proof. We start with the continuity of $a_{\boldsymbol{u}}(\cdot)(\cdot,\cdot)$.
Continuity of $a_{\boldsymbol{u}}(\cdot)(\cdot,\cdot)$: For all $\boldsymbol{u},\boldsymbol{v},\boldsymbol{\eta}\in\mathbb{V}_0$, $\lambda,\xi\in\mathbb{T}$, we evaluate the difference $a_{\boldsymbol{u}}(\tilde{\boldsymbol{u}})(\boldsymbol{u},\boldsymbol{\eta}) - a_{\boldsymbol{u}}(\tilde{\boldsymbol{v}})(\boldsymbol{v},\boldsymbol{\eta})$,

$$a_{\boldsymbol{u}}(\tilde{\boldsymbol{u}})(\boldsymbol{u},\boldsymbol{\eta}) - a_{\boldsymbol{u}}(\tilde{\boldsymbol{v}})(\boldsymbol{v},\boldsymbol{\eta}) = \Big(2\mu(D_{\mathrm{II},r}(\boldsymbol{u}),\lambda)\mathbf{D}(\boldsymbol{u}),\mathbf{D}(\boldsymbol{\eta})\Big) - \Big(2\mu(D_{\mathrm{II},r}(\boldsymbol{v}),\xi)\mathbf{D}(\boldsymbol{v}),\mathbf{D}(\boldsymbol{\eta})\Big), \tag{2.132}$$

then, segregate the viscous term, and the plastic term, as follows

$$a_{\boldsymbol{u}}(\tilde{\boldsymbol{u}})(\boldsymbol{u},\boldsymbol{\eta}) - a_{\boldsymbol{u}}(\tilde{\boldsymbol{v}})(\boldsymbol{v},\boldsymbol{\eta}) = \Big(2\eta(\lambda)\mathbf{D}(\boldsymbol{u}),\mathbf{D}(\boldsymbol{\eta})\Big) - \Big(2\eta(\xi)\mathbf{D}(\boldsymbol{v}),\mathbf{D}(\boldsymbol{\eta})\Big) \tag{2.133}$$

$$+ \Big(\tau(\lambda)\frac{\sqrt{2}}{\sqrt{D_{\mathrm{II},r}(\boldsymbol{u})}}\mathbf{D}(\boldsymbol{u}),\mathbf{D}(\boldsymbol{\eta})\Big) - \Big(\tau(\xi)\frac{\sqrt{2}}{\sqrt{D_{\mathrm{II},r}(\boldsymbol{v})}}\mathbf{D}(\boldsymbol{v}),\mathbf{D}(\boldsymbol{\eta})\Big) \tag{2.134}$$

We use microstructure-viscous multifield continuity (2.117) for the term (2.133) and microstructure-plastic continuity (2.118) for the term (2.134) (lemma 3)

$$\begin{aligned}|a_{\boldsymbol{u}}(\tilde{\boldsymbol{u}})(\boldsymbol{u},\boldsymbol{\eta}) - a_{\boldsymbol{u}}(\tilde{\boldsymbol{v}})(\boldsymbol{v},\boldsymbol{\eta})| \leq \Big((2\eta_0 + 2\eta_\infty\,\|\lambda\|_{0,\infty})\,\|\boldsymbol{u}-\boldsymbol{v}\|_1 + 2\eta_\infty\,|\boldsymbol{v}|_{1,\infty}\,\|\lambda-\xi\|_0\Big)\,\|\boldsymbol{\eta}\|_1 \\ + \Big((2\tau_0+\tau_\infty(\|\lambda\|_{0,\infty}+\|\xi\|_{0,\infty})k\,\|\boldsymbol{u}-\boldsymbol{v}\|_1 + \tau_\infty k\,\|\lambda-\xi\|_0\,|\boldsymbol{v}|_{1,\infty}\Big)\,\|\boldsymbol{\eta}\|_1\,.\end{aligned} \tag{2.135}$$

We rearrange the terms as follows

$$|a_{\boldsymbol{u}}(\tilde{\boldsymbol{u}})(\boldsymbol{u},\boldsymbol{\eta}) - a_{\boldsymbol{u}}(\tilde{\boldsymbol{v}})(\boldsymbol{v},\boldsymbol{\eta})| \leq \Big((2\eta_0 + 2\eta_\infty \|\lambda\|_{0,\infty}) + (2\tau_0 + \tau_\infty(\|\lambda\|_{0,\infty} + \|\xi\|_{0,\infty})k)\Big) \|\boldsymbol{u}-\boldsymbol{v}\|_1 \|\boldsymbol{\eta}\|_1 + \Big(2\eta_\infty |\boldsymbol{v}|_{1,\infty} + \tau_\infty k |\boldsymbol{v}|_{1,\infty}\Big) \|\lambda - \xi\|_0 \|\boldsymbol{\eta}\|_1 \tag{2.136}$$

which concludes the proof of continuity of $a_{\tilde{\boldsymbol{u}}}(\cdot)(\cdot,\cdot)$.

Now, we proceed with the continuity of the form $a_\lambda(\cdot)(\cdot,\cdot)$

Continuity of $a_\lambda(\cdot)(\cdot,\cdot)$: For all $\boldsymbol{u},\boldsymbol{v},\boldsymbol{\eta} \in \mathbb{V}_0$, $\lambda,\xi,\zeta \in \mathbb{T}$, we evaluate the difference $a_\lambda(\tilde{\boldsymbol{u}})(\lambda,\zeta) - a_\lambda(\tilde{\boldsymbol{v}})(\xi,\zeta)$,

$$a_\lambda(\tilde{\boldsymbol{u}})(\lambda,\zeta) - a_\lambda(\tilde{\boldsymbol{u}})(\xi,\zeta) = \Big(\mathcal{M}(D_{\mathbb{II},r}(\boldsymbol{u}),\lambda),\zeta\Big) - \Big(\lambda, \boldsymbol{u}\cdot\nabla\zeta\Big) + \langle|\boldsymbol{u}\cdot\boldsymbol{n}|\,\lambda,\zeta\rangle_+ \tag{2.137}$$

$$- \Big(\mathcal{M}(D_{\mathbb{II},r}(\boldsymbol{v}),\xi),\zeta\Big) + \Big(\xi,\boldsymbol{v}\cdot\nabla\zeta\Big) - \langle|\boldsymbol{v}\cdot\boldsymbol{n}|\,\xi,\zeta\rangle_+ \tag{2.138}$$

We use the definition of thixotropic model, rearrange the convective terms and the boundary terms as

$$a_\lambda(\tilde{\boldsymbol{u}})(\lambda,\zeta) - a_\lambda(\tilde{\boldsymbol{v}})(\xi,\zeta) = \Big((\mathcal{M}_a + \mathcal{M}_b D_{\mathbb{II},r}(\boldsymbol{u}))\ \lambda,\zeta\Big) - \Big((\mathcal{M}_a + \mathcal{M}_b D_{\mathbb{II},r}(\boldsymbol{v}))\ \xi,\zeta\Big) \tag{2.139}$$

$$- \Big((\lambda-\xi), \boldsymbol{u}\cdot\nabla\zeta\Big) - \Big(\xi, (\boldsymbol{u}-\boldsymbol{v})\cdot\nabla\zeta\Big) \tag{2.140}$$

$$+ \langle|\boldsymbol{u}\cdot\boldsymbol{n}|\,(\lambda-\xi),\zeta\rangle_+ + \langle(|\boldsymbol{u}\cdot\boldsymbol{n}|\,\xi,\zeta\rangle_+ - \langle|\boldsymbol{v}\cdot\boldsymbol{n}|)\xi,\zeta\rangle_+ \tag{2.141}$$

We use microstructure-buildup multifield continuity (2.119) for the term (2.139), followed with L^2–L^∞–L^2 Hölder's inequality for the tri-linear buildup, L^2–L^∞–L^2 Hölder's inequality for the tri-linear convective terms (2.140), and Hölder's inequality for the boundary terms (2.141) and boundedness from above of the boundary norm with one norm to obtain

$$|a_\lambda(\tilde{\boldsymbol{u}})(\lambda,\zeta) - a_\lambda(\tilde{\boldsymbol{u}})(\xi,\zeta)| \leq \Big(\mathcal{M}_a + (\mathcal{M}_b+1)\,|\boldsymbol{u}|_{1,\infty}\Big) \|\lambda-\xi\|_0 \|\zeta\|_1 + \mathcal{M}_b \|\xi\|_0 |\boldsymbol{u}-\boldsymbol{v}|_{1,\infty} \|\zeta\|_1 \tag{2.142}$$

$$+ \|\lambda-\xi\|_0 \|\boldsymbol{u}\|_\infty \|\zeta\|_1 + \|\xi\|_0 \|\boldsymbol{u}-\boldsymbol{v}\|_\infty \|\zeta\|_1 \tag{2.143}$$

$$+ \langle|\boldsymbol{u}\cdot\boldsymbol{n}|\,\lambda-\xi\rangle_+ \|\zeta\|_1 + \langle|(\boldsymbol{u}-\boldsymbol{v})\cdot\boldsymbol{n}|\,\xi\rangle_+ \|\zeta\|_1\,. \tag{2.144}$$

We rearrange the terms as follows

$$|a_\lambda(\tilde{\boldsymbol{u}})(\lambda,\zeta) - a_\lambda(\tilde{\boldsymbol{u}})(\xi,\zeta)| \leq \Big(\mathcal{M}_a + (\mathcal{M}_b+1)\,|\boldsymbol{u}|_{1,\infty}\Big) \|\lambda-\xi\|_0 \|\zeta\|_1 + \langle|\boldsymbol{u}\cdot\boldsymbol{n}|\,\lambda-\xi\rangle_+ \|\zeta\|_1 + \Big(\mathcal{M}_b+1\Big) \|\xi\|_0 \|\boldsymbol{u}-\boldsymbol{v}\|_{1,\infty} \|\zeta\|_1 + \langle|(\boldsymbol{u}-\boldsymbol{v})\cdot\boldsymbol{n}|\,\xi\rangle_+ \|\zeta\|_1\,. \tag{2.145}$$

Remark 5. To remain within the set of bounded solutions, we used L^2–L^∞–L^2 Hölder's inequality for the tri-linear forms involving the microstructure, instead of using the argument of the continuous embedding of $H^1(\Omega)$ in $L^4(\Omega)$. As consequence, we require extra regularity for velocity.
The theorem used for the well-posedness of the coupled TVP problem guarantee only the existence of the solution, while the uniqueness remains an open question.

2.5 Approximation of Thixoviscoplastic problem

We set the approximate thixoviscoplastic problem in a general abstract conforming framework, then we proceed with the well-posedness question.

2.5.1 Abstract Setting

We start by introducing the finite dimensional subspaces $\mathbb{T}_h \subset \mathbb{T}, \mathbb{V}_h \subset \mathbb{V}, \mathbb{Q}_h \subset \mathbb{Q}$, and $\mathbb{W}_h := \mathbb{V}_h \times \mathbb{T}_h \subset \mathbb{W}$, with the superscript h being a parameter dependent on the mesh spacing.

We set $\tilde{\boldsymbol{u}}_h = (\boldsymbol{u}_h, \lambda_h), \tilde{\boldsymbol{v}}_h = (\boldsymbol{v}_h, \xi_h)$. The approximated TVP problem is to seek an approximated solution $(\tilde{\boldsymbol{u}}_h, p_h) \in \mathbb{W}_h \times \mathbb{Q}_h$ such that

$$a_{\tilde{\boldsymbol{u}}}(\tilde{\boldsymbol{u}}_h)(\tilde{\boldsymbol{u}}_h, \tilde{\boldsymbol{v}}_h) + b(\boldsymbol{v}_h, p_h) - b(\boldsymbol{u}_h, q_h) = l(\tilde{\boldsymbol{v}}_h) \quad \forall (\tilde{\boldsymbol{v}}_h, q_h) \in \mathbb{W}_h \times \mathbb{Q}_h, \tag{2.146}$$

equivalenty,

$$\begin{cases} a_{\tilde{\boldsymbol{u}}}(\tilde{\boldsymbol{u}}_h)(\tilde{\boldsymbol{u}}_h, \tilde{\boldsymbol{v}}_h) + b(\boldsymbol{v}_h, p_h) = l(\tilde{\boldsymbol{v}}_h) & \forall\, \tilde{\boldsymbol{v}}_h \in \mathbb{W}_h, \\ b(\boldsymbol{u}_h, q_h) = 0 & \forall\, q_h \in \mathbb{Q}_h, \end{cases} \tag{2.147}$$

and in operator form, assuming $\mathcal{B}\mathbb{V}_h \subset \mathbb{Q}_h'$,

$$\begin{cases} \mathcal{A}_{\tilde{\boldsymbol{u}}}(\tilde{\boldsymbol{u}}_h)\tilde{\boldsymbol{u}}_h + \mathcal{B}^{\mathrm{T}} p_h = \boldsymbol{f}_{\tilde{\boldsymbol{u}}} & \text{on } \mathbb{W}_h', \\ \mathcal{B}\boldsymbol{u}_h = 0 & \text{on } \mathbb{Q}_h', \end{cases} \tag{2.148}$$

Now, we proceed with the well-posedness of the approximate TVP problem.

2.5.2 Well-posedeness of the Approximate TVP Problem

The approximation of TVP problem, in its general abstract form using conforming framework, is to seek an approximated solution $(\tilde{\boldsymbol{u}}_h, p_h) \in \mathbb{W}_h \times \mathbb{Q}_h$, such that

$$a_{\tilde{\boldsymbol{u}}}(\tilde{\boldsymbol{u}}_h)(\tilde{\boldsymbol{u}}_h, \tilde{\boldsymbol{v}}_h) + b(\boldsymbol{v}_h, p_h) - b(\boldsymbol{u}_h, q_h) = l(\tilde{\boldsymbol{v}}_h) \quad \forall (\tilde{\boldsymbol{v}}_h, q_h) \in \mathbb{W}_h \times \mathbb{Q}_h, \tag{2.149}$$

The problem that we have to solve here is the existence and uniqueness of the solution $(\tilde{\boldsymbol{u}}_h, p_h)$. We assume that the $\inf - \sup$ condition for the pair $(\mathbb{V}_h, \mathbb{Q}_h)$ is satisfied, that is

$$\exists \beta > 0 \,\text{s.t.}\, \sup_{\boldsymbol{v}_h \in \mathbb{V}_h} \frac{b(\boldsymbol{v}_h, q_h)}{\|\boldsymbol{v}_h\|} \geq \beta \, \|q_h\|_{\mathbb{Q}/\ker \mathcal{B}^{\mathrm{T}}} \quad \forall q_h \in \mathbb{Q}_h, \tag{2.150}$$

where β is independent of h. The results concerning existence, uniqueness, and boundedness of the solution with the data of the approximate problem are stated in the following theorem.

Theorem 2 (Well-posedness: Approximate problem). *Let $\boldsymbol{f}_{\boldsymbol{u}} \in (L^2(\Omega))^2$ and $f_\lambda \in L^2(\Omega)$, then the thixoviscoplastic problem (2.21) has a solution $(\tilde{\boldsymbol{u}}_h, p_h) = (\lambda_h, \boldsymbol{u}_h, p_h) \in \mathbb{W}_h \times \mathbb{Q}_h$. And it satisfies the estimate*

$$\|\boldsymbol{u}_h\|_1 \leq \frac{1}{\eta_0 \mathcal{C}_K} \|\boldsymbol{f}_{\boldsymbol{u}}\|_0 \,, \tag{2.151}$$

$$\|p_h\|_0 \leq \frac{1}{\beta}\Big(1 + \frac{2\,(\eta_\infty + k\tau_\infty)}{\eta_0 \mathcal{C}_K}\Big) \|\boldsymbol{f}_{\boldsymbol{u}}\|_0 \,, \tag{2.152}$$

$$\|\lambda_h\|_0 \leq \frac{1}{\mathcal{M}_a} \|f_\lambda\|_0 \,, \tag{2.153}$$

$$\mathcal{M}_a \|\lambda_h\|_0^2 + \frac{1}{2}\langle \lambda_h \rangle^2 \leq \frac{1}{\mathcal{M}_a} \|f_\lambda\|_0^2 . \tag{2.154}$$

where $\mathcal{C}_K$ denotes the Korn's inequality constant, and β is the Ladyzhenskaya-Babuška-Brezzi (LBB) constant.

Proof. For the proof, we follow the same steps as for the proof of Theorem 1 including assumptions.

2.6 Concluding Remarks

We presented, in this chapter, the FEM well-posedness of thixoviscoplastic flow problems.

We started by introducing the variational principle and functional spaces in the context of shear rate independent plastic viscosity, that is the plastic viscosity is exclusively dependent on microstructure $\eta = \eta(\lambda)$, and microstructure space as velocity space. Then, we expressed the continuous TVP problems in a classical abstract setting of saddle point problems based on the incompressibility constraint, and the approximated one in conforming framework.

The existence and uniqueness of the microstructure and viscoplastic subproblems are treated in parallel manner. For the viscoplastic subproblem, we used the *Lemma plastic monotonicity in* $\mathbb{R}^{d\times d}$ to demonstrate the monotonicity property for the nonlinear diffusion operator. For the microstructure subproblem, for a given divergence-free velocity, we used the weak coercivity and the continuity of the microstructure bilinear form. Then, for the multifield coupled TVP problem, we rewrite the coupled multifield operator as a sum of completely continuous, and a nonlinear contraction operators, then used fixed point Theorem.

3

Monolithic Newton-Multigrid Thixoviscoplastic Solver

We are concerned, in this chapter, with the development of a finite element method (FEM) thixoviscoplastic (TVP) solver based on monolithic Newton-multigrid method to tackle TVP generalized Stokes equations. In our approach, we treat the nonlinearity of the problem in black box framework using an adaptive combined discrete Newton's method and monolithic geometric multigrid (MG) solver. The linear systems inside the outer nonlinear iterations are solved in a block Gauss-Seidel way, where the construction of the blocks is based on incompressibility constraint. Furthermore, with our choice of *discontinuous* linear pressure, we efficiently handle the problem coupling locally. And to maintain the solver efficiency with the fact of noncoupling of pressure and microstructure, we collocate the microstructure with the velocity in the quadratic interpolation.

3.1 Introduction

In this chapter, we intend to develop a Newton-multigrid FEM solver for thixoviscoplastic flows. As we use the FEM quasi-Newtonian modeling approach [63], which requires a robust solver with respect to regularization parameter to obtain accurate numerical solutions, we opt for a strategy with combined adaptive discrete Newton's method and a monolithic geometric multigrid solver to delicately handle the regularization issue. The adaptivity related to discrete Newton's method is due to the adaptive step-size in finite difference for the approximation of Jacobian, while accuracy or convergence of linear multigrid solver is made dependently on the accuracy or convergence of the nonlinear solver. Furthermore, we use local pressure Schur complement (LPSC) to handle linearized saddle point problems inside the outer Newton sweeps [32, 76, 79]. The resulting algorithm is a block Gauss-Seidel iteration's process, where we base the construction of the blocks on incompressibility constraint. On one hand, we opt for discontinuous linear pressure FEM approximation P_1^{disc} for its advantageous coincides of degree of freedoms with the choices of the blocks for Gauss-Seidel for an efficient treatment of the problem coupling locally. On the other hand, due to noncoupling of pressure and microstructure, we collocate velocity and microstructure with the same FEM quadratic interpolation Q_2.

The remainder of the chapter is structured as follows, we devote Section §2 to FEM discretization. We use the stable Stokes pair (Q_2, P_1^{disc}) for velocity and pressure approximations as a long-standing robust choice in numerical simulations for incompressible flow problems [30, 31, 42, 64]. Furthermore, to

maintain the solver efficiency for generalized TVP Stokes problems, we choose the same Q_2 interpolation for microstructure as for velocity, which impose some theoretical challenges for the approximations of the microstructure equation of nonmatching of the coercivity with the space's norm. We overcome these challenges with stabilization, that is edge-oriented jump of the gradient to upgrade the coercivity to match the space norm. It is consistent with FEM discretization, linear with respect to the problem, and in addition, it enhances the solver's efficiency [62, 77].

Then, in Section §3, we treat the discrete system with an adaptive combined discrete Newton's method and a monolithic geometric multigrid solver. The solver has two folds with respect to adaptivity: the one related to discrete Newton's method via the step-size in finite difference for the Jacobian approximation, while the other is related to a linear multigrid solver via the dependency of its accuracy or convergence on the accuracy or the convergence of nonlinear solver. We start by giving the inspiring idea for the adaptivity in Jacobian approximation from adaptive operator-splitting of the Jacobian [54, 56], that is, an adaptivity with respect to the choice of directions in finite difference, followed by adaptive strategy, that we use in this work, via the step-length control parameter in finite difference for the Jacobian approximation. The algorithm is solely dependent on the actual rate of nonlinear residual convergence. Therefore, the accuracy requirement for the convergence of the linear solver is made optimal accordingly. As a consequence, we avoid unnecessary iterations feeding singularities far away from a higher convergence rate, or lack of iterations for the completeness of nonlinear convergence in the radius of Newton's quadratic convergence.

In Section §3.1, we concretize the monolithic geometric multigrid solver on our FEM discretization choice. We give the multigrid components, that is two level algorithm, grid transfer operators, and smoothers. Subsection §3.5.1 is devoted to two level algorithm as a base for the different multigrid cycles, namely V-cycle, W-cycle, and F-cycle [20]. Then, in Subsection §3.5.2 we present the inter grid transfer operators, namely restrictions and prolongations, in geometric context and its corresponding algebraic counterpart. The smoothers are explained in Subsection §3.5.3, they are local pressure Schur complement schemes, which are generalization of Vanka-type smoothers for our TVP coupled systems with the typical saddle point character [31, 68, 76, 79]. They are simple iterative relaxation methods that solve directly on element level, one element or a patch of elements, and perform an outer block Gauss-Seidel iteration. In other words, the choices of the blocks for the linearized TVP systems are based on the pressure degrees of freedom equivalently on the incompressibility constraint. The local character of this procedure, together with a global defect-correction mechanism on one hand, and the choice of discontinuous FE approximations for pressure on the other hand, results in an efficient solver for the TVP problem.

The summarizing Section §3.4, highlights the conclusions and main results of the chapter. Firstly, we chose the most efficient and practical FEM discretization for incompressible Stokes equations, and we integrate the remaining field for thixoviscoplastic flow problems to maintain the choice's practicality. As a consequence, the coupled field of velocity and microstructure is treated as a unified 'upgraded velocity' field in the classical context of Stokes equations. Secondly, we present a black box nonlinear solver based on adaptive discrete Newton's method, where its adaptivity is solely dependent on the actual rate of the nonlinear residual convergence. Beside that, the linear solver is made to achieve the optimal convergence accordingly, which results in a singularity-free convergence process and a robust solver with respect to the starting guess. Thirdly, we present the geometric multigrid ingredient. Then, we introduce the smoother based on the local pressure Schur complement which leads to block Gauss-Seidel iteration's process. The local handling of the problem coupling with the choice of discontinuous FE approximations for pressure gives rise to an efficient TVP solver.

3.2 Finite Element Discretization

We devote this Section §2 to FEM discretization. We use the stable Stokes pair (Q_2, P_1^{disc}) for velocity and pressure approximations as a long-standing robust choice in numerical simulations for incompressible flow problems [3, 15, 42]. Furthermore, to maintain the solver efficiency for the generalized TVP Stokes problems, we choose the same Q_2 interpolation for the microstructure as for velocity, which impose some theoretical challenges for microstructure equation of nonmatching of the coercivity with the space's norm [26, 27]. We overcome these challenges with stabilization, that is gradient's inter-element jumps, named concisely edge-oriented stabilization, to upgrade the microstructure form in a manner that the coercivity matches the space norm and stabilize convections. Furthermore, it is consistent with FEM discretization, linear with respect to the problem, and in addition, it enhances the solver's efficiency [62, 77].

Let the domain Ω be partitioned by a grid $\mathcal{T}_h$ which are assumed to be quadrilaterals. For an element $K \in \mathcal{T}_h$, we denote by $\mathcal{E}(K)$ the set of all 1-dimensional edges of K, and by $\mathcal{E}_i$ the set of all interior element edges of the grid $\mathcal{T}_h$

$$\mathcal{E}_i := \bigcup_{k \in \mathcal{T}_h} \{E \in \mathcal{E}(K) \mid E \cap \partial\Omega = \emptyset\}. \tag{3.1}$$

We define the conforming finite element spaces $\mathbb{V}_h \subset \mathbb{V}$, and $\mathbb{Q}_h \subset \mathbb{Q}$ as follows:

$$\mathbb{V}_h = \left\{ \boldsymbol{v}_h \in \mathbb{V}, \boldsymbol{v}_{h|K} \in \ (Q_r(K))^2 \forall\ K \in \mathcal{T}_h,\ \boldsymbol{v}_h = 0 \text{ on } \partial\Omega_h \right\}, \tag{3.2}$$

$$\mathbb{T}_h = \left\{ \xi_h \in \mathbb{T}, \xi_{h|K} \in \ Q_r(K) \forall\ K \in \mathcal{T}_h \right\}, \tag{3.3}$$

$$\mathbb{Q}_h = \left\{ q_h \in \mathbb{Q}, q_{h|K} \in \ P_{r-1}^{\text{disc}}(K) \forall\ K \in \mathcal{T}_h \right\}, \tag{3.4}$$

where Q_r and P_r are polynomials with maximum power in each coordinate less or equal r, and total power less or equal r, respectively. In what follows, the polynomial power r is set to equal 2. Figure 3.1 exposes the distribution of degrees of freedom for the flow fields.

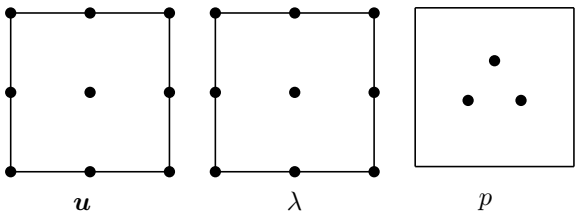

Fig. 3.1: **FEM pair for thixoviscoplastic flow problem:** Higher order FEM pair $Q_2/Q_2/P_1^{disc}$.

Remark 6. Higher order FEM choice for velocity counterbalances the regularization impact, while microstructure is collocated with velocity degrees of freedom for efficiency reason due to noncoupling of microstructure and pressure.

We set $\mathbb{W}_h := \mathbb{T}_h \times \mathbb{V}_h$, $\tilde{\boldsymbol{u}}_h = (\lambda_h, \boldsymbol{u}_h)$, $\tilde{\boldsymbol{v}}_h = (\xi_h, \boldsymbol{v}_h)$, and define the coupled velocity-microstructure form on $\mathbb{W}_h \times \mathbb{W}_h$ as follows

$$a_{\tilde{\boldsymbol{u}}}(\tilde{\boldsymbol{u}}_h)(\tilde{\boldsymbol{u}}_h, \tilde{\boldsymbol{v}}_h) = a_{\boldsymbol{u}}(\tilde{\boldsymbol{u}}_h)(\boldsymbol{u}_h, \boldsymbol{v}_h) + a_\lambda(\tilde{\boldsymbol{u}}_h)(\lambda_h, \xi_h) \quad \forall\ (\tilde{\boldsymbol{u}}_h, \tilde{\boldsymbol{v}}_h) \in \mathbb{W}_h \times \mathbb{W}_h. \tag{3.5}$$

The stabilized approximated TVP problem reads: *Find* $(\tilde{\boldsymbol{u}}_h, p_h) \in \mathbb{W}_h \times \mathbb{Q}_h$, *such that*

$$a_{\tilde{\boldsymbol{u}}}(\tilde{\boldsymbol{u}}_h)(\tilde{\boldsymbol{u}}_h, \tilde{\boldsymbol{v}}_h) + j_{\tilde{\boldsymbol{u}}}(\tilde{\boldsymbol{u}}_h)(\tilde{\boldsymbol{u}}_h, \tilde{\boldsymbol{v}}_h) + b(\boldsymbol{v}_h, p_h) - b(\boldsymbol{u}_h, q_h) = 0, \quad \forall\ (\tilde{\boldsymbol{v}}_h, q_h) \in \mathbb{W}_h \times \mathbb{Q}_h. \tag{3.6}$$

The stabilization term $j_{\tilde{\boldsymbol{u}}}(\cdot)(\cdot,\cdot)$ is a bilinear form for the coupled field

$$j_{\tilde{\boldsymbol{u}}}(\tilde{\boldsymbol{u}}_h)(\tilde{\boldsymbol{u}}_h, \tilde{\boldsymbol{v}}_h) := j_{\boldsymbol{u}}(\tilde{\boldsymbol{u}}_h)(\boldsymbol{u}_h, \boldsymbol{v}_h) + j_{\lambda}(\tilde{\boldsymbol{u}}_h)(\lambda_h, \xi_h). \tag{3.7}$$

The stabilization (3.7) consists of the penalization of the inter-element gradient's jumps which we term edge-oriented stabilization. The bilinear velocity edge-oriented stabilization $j_{\boldsymbol{u}}(\cdot,\cdot)$ is defined as follows [65, 77]

$$j_{\boldsymbol{u}}(\tilde{\boldsymbol{u}}_h)(\boldsymbol{u}_h, \boldsymbol{v}_h) \ = \sum_{E \in \mathcal{E}_i} \gamma_{\boldsymbol{u}} |E|^2 \int_E [\nabla \boldsymbol{u}_h] : [\nabla \boldsymbol{v}_h]\, d\sigma \quad \forall\ \boldsymbol{u}_h, \boldsymbol{v}_h \in \mathbb{V}_h, \tag{3.8}$$

and similarly we define the microstructure edge-oriented stabilization $j_{\lambda}(\cdot,\cdot)$

$$j_{\lambda}(\tilde{\boldsymbol{u}}_h)(\lambda_h, \xi_h) \ = \sum_{E \in \mathcal{E}_i} \gamma_{\lambda} |E|^2 \int_E [\nabla \lambda_h]\, [\nabla \xi_h]\, d\sigma \quad \forall\ \lambda_h, \xi_h \in \mathbb{T}_h. \tag{3.9}$$

Where $\gamma_{\boldsymbol{u}}$ and γ_{λ} are user-given parameters with problem dependent optimal choice.

The stabilization term (3.7) is consistent, linear with respect to the flow field, and enhances the solver efficiency. The bilinear velocity edge-oriented stabilization term (3.8) is typically used for convection dominated flow problems to stabilize high Reynolds number flows. And, the bilinear microstructure edge-oriented stabilization term (3.9) is used here mainly to cover the coercivity of microstructure in the strong norm.

On the one hand, higher order choice for velocity counterbalances the regularization impact, and stabilization, on the other hand enhances the coercivity to match the complete norm of the microstructure space $\mathbb{T}$ equivalently as one-norm. That is the triple norm defined on the microstructure space

$$|\!|\!| \xi_h |\!|\!|^2 = \|\xi_h\|_0^2 + j_{\lambda}(\xi_h, \xi_h) \quad \forall\ \xi_h \in \mathbb{T}_h. \tag{3.10}$$

Furthermore, the stabilization (3.9) term is expected to recover the optimal order of convergence for microstructure with respect to the triple norm (3.10) [19, 9, 12]. The detailed corresponding analysis goes beyond the goal of this thesis.

The FEM discretization of the thixoviscoplastic problem is done to take care mainly of saddle point character related to incompressibility only, while microstructure is collocated with velocity degrees of freedom for solver efficiency due to noncoupling of microstructure and pressure fields. In order to deal with the dependency of solutions on regularization parameter, we opt for higher order Q_2 choice for velocity to counterbalance the regularization impact. The discontinuous choice for the pressure discretization P_1^{disc} is consistent with its natural regularity requirement and practical with respect to our choice for a monolithic solution approach. The edge-oriented stabilization, as a penalization of inter-element gradient jumps, is mainly driven by the lack of coercivity of $a_{\lambda}(\cdot)(\cdot,\cdot)$ in a strong norm.

The resulting nonlinear discrete system based on this FEM discretization choice is then linearized in Section §3.3 in a black box manner using discrete adaptive Newton's method.

3.3 Discrete Adaptive Newton's Method

This section is concerned with the treatment of the discrete nonlinear TVP system with an adaptive combined discrete Newton's method and monolithic geometric multigrid solver. The adaptivity for discrete Newton's method is done via the step-size in finite difference for the Jacobian approximation. Moreover, it is symbiotically connected to linear multigrid solver through the dependency of its accuracy or convergence on the accuracy or the convergence of nonlinear solver.

Let $\{\varphi_i, i = 1, 2, \ldots, \mathtt{dim}\mathbb{W}_h\}$ and $\{\psi_i,\ i = 1, \ldots, \mathtt{dim}\mathbb{Q}_h\}$ denote the basis of the spaces $\mathbb{W}_h$ and $\mathbb{Q}_h$, respectively.
The nonlinear discrete residuals for the system (3.6) is denoted by $\mathcal{R}(\mathcal{U}) \in \mathbb{R}^{\mathtt{dim}\mathbb{W}_h + \mathtt{dim}\mathbb{Q}_h}$ and is given as follows:

$$R(\mathcal{U}) = (\mathcal{R}_{\boldsymbol{u}}(\boldsymbol{u}, \lambda, p), \mathcal{R}_{\lambda}(\boldsymbol{u}, \lambda), \mathcal{R}_p(\boldsymbol{u}, p)), \tag{3.11}$$

rewritten in a more compact form as:

$$R(\mathcal{U}) = (\mathcal{R}_{\tilde{\boldsymbol{u}}}(\tilde{\boldsymbol{u}}, p), \mathcal{R}_p(\tilde{\boldsymbol{u}}, p)), \tag{3.12}$$

with the vector $\mathcal{U} = (\boldsymbol{u}, \lambda, p) = (\tilde{\boldsymbol{u}}, p) \in \mathbb{W}_h \times \mathbb{Q}_h$, which is expressed concisely as:

$$\mathcal{U} = \sum_{i=1}^{\mathtt{dim}\mathbb{W}_h} \tilde{\boldsymbol{u}}_i \varphi_i + \sum_{i=1}^{\mathtt{dim}\mathbb{Q}_h} p_i \psi_i, \quad \tilde{\boldsymbol{u}}_i, p_i \in \mathbb{R}. \tag{3.13}$$

The nonlinear iteration is updated with the correction $\delta\mathcal{U}, \mathcal{U}^{l+1} = \mathcal{U}^l + \delta\mathcal{U}$. Then, the Newton linearization gives the following approximation for the residuals:

$$\mathcal{R}(\mathcal{U}^{l+1}) = \mathcal{R}(\mathcal{U}^l + \delta\mathcal{U}) \simeq \mathcal{R}(\mathcal{U}^l) + \left(\frac{\partial \mathcal{R}(\mathcal{U}^l)}{\partial \mathcal{U}}\right) \delta\mathcal{U}. \tag{3.14}$$

The Newton's method iterations, assuming invertible Jacobians, are given as follows:

$$\mathcal{U}^{l+1} = \mathcal{U}^l - \omega_l \left(\frac{\partial \mathcal{R}(\mathcal{U}^l)}{\partial \mathcal{U}}\right)^{-1} \mathcal{R}(\mathcal{U}^l). \tag{3.15}$$

The damping parameter $\omega_l \ \in (0, 1]$ is chosen such that

$$\left\|\mathcal{R}(\mathcal{U}^{l+1})\right\| \leq \left\|\mathcal{R}(\mathcal{U}^l)\right\|. \tag{3.16}$$

The damping parameter is not sufficient for the convergence of this type of highly nonlinear problem, either due to the presence of Jacobian's singularities related to the problem or simply by being out of the domain of Newton convergence [54, 62]. We use a generalized Newton's method, which consists of using an approximation of Jacobians far away from the range of the quadratic convergence of the Newton's method or close to singularities and an accurate approximation of Jacobian in the quadratic region of convergence in an adaptive manner with respect to residual convergence.

In next Subsection §3.3.1, we present the adaptive strategy by operator-splitting of Jacobian, followed by the adaptive strategy throughout the adaptive step-size control parameter for Jacobian approximation in Subsection §3.3.2.

3.3.1 Adaptive Newton via Operator-adaptive Splitting

Based on a priori analysis of the Jacobian's property, the Jacobian is splitted into a direct sum of corresponding operators with different properties; for details we refer to the work [53, 54], as follows: Firstly, by splitting the Jacobian as a sum of two operators and perform a Jacobian approximation for each as follows:

$$\left(\frac{\partial \mathcal{R}(\mathcal{U}^l)}{\partial\, \mathcal{U}}\right) = \left(\frac{\partial \tilde{\mathcal{R}}(\mathcal{U}^l)}{\partial \mathcal{U}}\right) + \delta_l \left(\frac{\partial \hat{\mathcal{R}}(\mathcal{U}^l)}{\partial \mathcal{U}}\right). \tag{3.17}$$

Secondly, by selecting a specific field or part of it $\mathcal{U} = (\tilde{\mathcal{U}}, \hat{\mathcal{U}})$ and just perform the Jacobian calculation with such a specific field or part of it, as follows:

$$\left(\frac{\partial \mathcal{R}(\mathcal{U}^l)}{\partial\, \mathcal{U}}\right) = \left(\frac{\partial \mathcal{R}(\mathcal{U}^l)}{\partial \tilde{\mathcal{U}}}\right) + \delta_l \left(\frac{\partial \mathcal{R}(\mathcal{U}^l)}{\partial \hat{\mathcal{U}}}\right). \tag{3.18}$$

Increasing the contribution from the second operator on the right side of the equation (3.17, 3.18) improves the convergence behavior, but this contribution needs to remain under control. Furthermore, the relative changes of the residual give precious information about the singularity of the Jacobian. The larger the relative changes in the residual with the first operator on the right side of equation (3.17, 3.18) the smaller the relative changes of δ_l should be, and vice versa. The operator's damping parameter $\delta_l \in (0, 1]$ is solely dependent on the rate of actual residual convergence

$$r_l := \frac{\|\mathcal{R}(\mathcal{U}^l)\|}{\|\mathcal{R}(\mathcal{U}^{l-1})\|}, \tag{3.19}$$

with the following nonlinear increment's update function $i_{\mathrm{a}}(\cdot)$ for the operator's damping parameter

$$\frac{\delta_{l+1}}{\delta_l} = i_{\mathrm{a}}(r_l), \tag{3.20}$$

where the numerical simulations, see [54], give raise to an analytic expression for the nonlinear increment's update function as follows

$$i_{\mathrm{a}}(r_l) = 0.2 + \frac{4}{0.7 + \exp(1.5 r_l)}. \tag{3.21}$$

It is worth mentioning that the operator-related damped Jacobian method is originally developed for the continuous Newton's method [62]. This method is successfully applied for different complex flow problems [56]. In the context of discrete Newton, it can also be used with directional differencing, where the direction is chosen appropriately to provide the splitting as in (3.18), or simply by splitting the nonlinear residual as in (3.17) . In this work, we rather go for the adaptive strategy in the discrete Newton based on step-length control in the finite difference approximation of the Jacobian, subsection §3.3.2.

3.3.2 Adaptive Newton via Adaptive Step-length Control Parameter

The adaptive discrete Newton method used in the current work is based on adaptive step-length control in finite difference of discrete residual, for details we refer to the work [35, 36]. The method does not require any a priori analysis of the Jacobian, it is a pure black box method. The Jacobian matrix $\left(\frac{\partial \mathcal{R}(\mathcal{U}^l)}{\partial \mathcal{U}}\right)$ is approximated using the finite differences along the unit coordinate directions as

$$\left(\frac{\partial \mathcal{R}(\mathcal{U}^l)}{\partial \mathcal{U}}\right)_{ij} \approx \frac{\mathcal{R}_i(\mathcal{U}^l + \varepsilon_l \boldsymbol{e}_j) - \mathcal{R}_i(\mathcal{U}^l - \varepsilon_l \boldsymbol{e}_j)}{2\varepsilon_l}, \tag{3.22}$$

where $\boldsymbol{e}_j$ is the vector with unit j-th component and zero otherwise. The parameter ε_l is updated according to the rate of the actual residual convergence r_l

$$\frac{\varepsilon_{l+1}}{\varepsilon_l} = j_{\mathrm{a}}(r_l). \tag{3.23}$$

The Jacobian given by finite difference formula (3.22) is different from the Jacobian given by operator-adapted splitting formulas (3.17, 3.18). Nevertheless, the feedback for the singularity is similar and it is given by the rate of the actual residual convergence (3.19). As consequence, we opt for the inversely proportional nolinear increment's update function; In the former, it allows for a bigger step-length parameter ε to remove numerical instabilities, while in the latter it reduces the contribution part responsible for such instabilities.

We briefly present the main steps for the solver in Algorithm 1.

Algorithm 1: Discrete adaptive Newton via step-length control parameter

Result: $\mathcal{U}^{l+1} = \mathcal{U}^l - \omega_l \delta\mathcal{U}^l$, $\omega_l \in (0, 1]$
$r_0 = \left\|\mathcal{R}(\mathcal{U}^0)\right\|$, $\varepsilon_0^{\pm}$;
while $r_l \geq r_c$;
do

- (i) **Calculate convergence rate** $r_l = \frac{\left\|\mathcal{R}(\mathcal{U}^l)\right\|}{\left\|\mathcal{R}(\mathcal{U}^{l-1})\right\|}$;
- (ii) **Step-length size update** $\varepsilon_{l+1}^{\pm} = j_{\mathrm{a}}(r_l)\varepsilon_l^{\pm}$;
- (iii) **Calculate FD Jacobian** $\left[\mathcal{J}(\mathcal{U}^l)\right]_{ij} \approx \frac{\left(\mathcal{R}_i(\mathcal{U}^l + \varepsilon_l^+ \boldsymbol{e}_j) - \mathcal{R}_i(\mathcal{U}^l - \varepsilon_l^- \boldsymbol{e}_j)\right)}{\varepsilon_l^+ + \varepsilon_l^-}$;
- (iv) **Solve via MG** $\mathcal{J}(\mathcal{U}^l)\delta\mathcal{U}^l = \mathcal{R}(\mathcal{U}^l)$;

end

Remark 7. The damping parameter ω_l is set to unity, since it is not enough for convergence of the Algorithm 1. The feedback singularity is given by the rate of the actual residual convergence r_l in (i). Thus, the increment's update function $j_{\mathrm{a}}(r_l)$ in (ii) is chosen in a way to allow for bigger step-length parameter $\varepsilon^{\pm}$ to remove numerical instabilities and a smaller one in the region of quadratic convergence, it turns out that it is sufficient to take $j_{\mathrm{a}} = 1/i_{\mathrm{a}}$, numerical tests supporting this choice can be found in [36]. The finite difference scheme in (iii) is made to switch flexibly between backward finite difference ($\varepsilon_l^+ = 0$), forward finite difference ($\varepsilon_l^- = 0$), and central finite difference ($\varepsilon_l^- = \varepsilon_l^+ \neq 0$). To solve the linear system (iv), we use monolithic adaptive geometric multigrid methods, where the convergence of the linear solver is made flexible to match the optimal accuracy of the nonlinear solver by means of the rate of the actual residual convergence [62]. The analysis of the global convergence property of the algorithm and the smoothing property of multigrid goes beyond the interest of this thesis.

An integral part of the efficiency of Algorithm 1 is its symbiotic connection to the linear solver. In the following Section §3.4, we concretize the application for monolithic geometric multigrid for the linearized thixoviscoplastic system on our FEM discretization choice.

3.4 Monolithic Multigrid Linear Solver

Multigrid methods (MG) effectively damp both high- and low-frequency components of errors, using effectively the complementary processes of relaxation/smoothing and coarse-grid correction [76]. In this thesis, we intend to take the maximum advantage of this property in the context of linearized TVP Stokes equations. As the TVP flow problem is highly nonlinear coupled for velocity and microstructure flow fields on one hand, and incompressible on the other hand, we favor, in this work, the coupling treatment of the flow fields. That is, we intend to apply a monolithic multigrid algorithm for the linearized TVP problem in the context of our FEM discretization choice. In this regard, we opt for the geometric variant of monolithic multigrid, as ready-to-use in FEM context [76].

A close look to the linearized TVP problem (3.25), shows a typical saddle-point type structure of the following form:

$$\begin{pmatrix} \dfrac{\partial \mathcal{R}_{\tilde{\boldsymbol{u}}}(\tilde{\boldsymbol{u}})}{\partial \tilde{\boldsymbol{u}}} & \dfrac{\partial \mathcal{R}_{\tilde{\boldsymbol{u}}}(\tilde{\boldsymbol{u}})}{\partial p} \\ \dfrac{\partial \mathcal{R}_{p}(\tilde{\boldsymbol{u}})}{\partial \tilde{\boldsymbol{u}}} & 0 \end{pmatrix}. \tag{3.24}$$

Indeed, the linearized systems to be solved at each nonlinear sweep with a symbolic Jacobian calculation are given as follows:

$$\left(\frac{\partial \mathcal{R}(\mathcal{U})}{\partial \mathcal{U}}\right) \delta\mathcal{U} = \begin{pmatrix} \dfrac{\partial \mathcal{R}_{\tilde{\boldsymbol{u}}}(\tilde{\boldsymbol{u}})}{\partial \tilde{\boldsymbol{u}}} & \dfrac{\partial \mathcal{R}_{\tilde{\boldsymbol{u}}}(\tilde{\boldsymbol{u}})}{\partial p} \\ \dfrac{\partial \mathcal{R}_{p}(\tilde{\boldsymbol{u}})}{\partial \tilde{\boldsymbol{u}}} & 0 \end{pmatrix} \begin{pmatrix} \delta\tilde{\boldsymbol{u}} \\ \delta p \end{pmatrix} = - \begin{pmatrix} \mathcal{R}_{\tilde{\boldsymbol{u}}} \\ \mathcal{R}_{p} \end{pmatrix}. \tag{3.25}$$

The main focus of this section is to adapt monolithic geometric multigrid methods for linearized TVP Stokes equations on our FEM discretization choice, that is, the pair (Q_2, P_1^{disc}) for $(\tilde{\boldsymbol{u}}, p)$.

The following subsections are dedicated to the multigrid components, that is two-level algorithm, inter grid transfer operators, and smoothers. In Subsection §3.4.1, we start by two-level algorithm as a base for different multigrid cycles, V-cycle, W-cycle, and F-cycle.

3.4.1 Two-Level Algorithm

We consider the linear saddle-point problem (3.25) which we rewrite in the following manner:

$$\mathcal{J}\delta\mathcal{U} = \mathcal{R}. \tag{3.26}$$

Let $\{\mathcal{T}_{h_k}\}$ be a family of hierarchy multilevel triangulations associated with mesh size h_k, that is, each element triangulation $\mathcal{T}_{h_{k-1}}$ on level $k-1$ is split into 2^d $(d=2)$ new elements to get triangulations $\mathcal{T}_{h_k}$ on level k, which are denoted by $\sigma_i(K)$, $i = 1, \ldots, 2^d$, see Figure 3.2.

We set $\mathcal{W}_k := \mathbb{R}^{\dim \mathbb{W}_{h_k}}$, $\mathcal{Q}_k := \mathbb{R}^{\dim \mathbb{Q}_{h_k}}$, $\mathcal{V}_k := \mathcal{W}_k \times \mathcal{Q}_k$ and let $\boldsymbol{\mathcal{I}}_k^{k-1}$ and $\boldsymbol{\mathcal{I}}_{k-1}^{k}$ denote the grid transfer operators, $\boldsymbol{\mathcal{I}}_k^{k-1} : \mathcal{V}_k \longrightarrow \mathcal{V}_{k-1}$ and $\boldsymbol{\mathcal{I}}_{k-1}^{k} : \mathcal{V}_{k-1} \longrightarrow \mathcal{V}_k$. The parameters $\nu_1, \nu_2 \geq 0$ denote the number of pre- and post-smoothing steps, respectively.

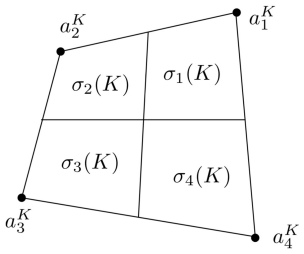

Fig. 3.2: **Multilevel refinement:** Refinement of element K into sub-elements $\sigma_i(K)$, $i = 1, \ldots, 2^d$, [48].

The k^{th} level iteration $MG(k, \delta\mathcal{U}_0, \mathcal{R})$ of the multigrid algorithm with an initial guess $\delta\mathcal{U}_0$ yields an approximation to $\delta\mathcal{U}_k$, the solution of

$$\mathcal{J}_k \delta\mathcal{U} = \mathcal{R} \tag{3.27}$$

One step can be described concisely throughout the multi-level algorithm in Figure 3.3.

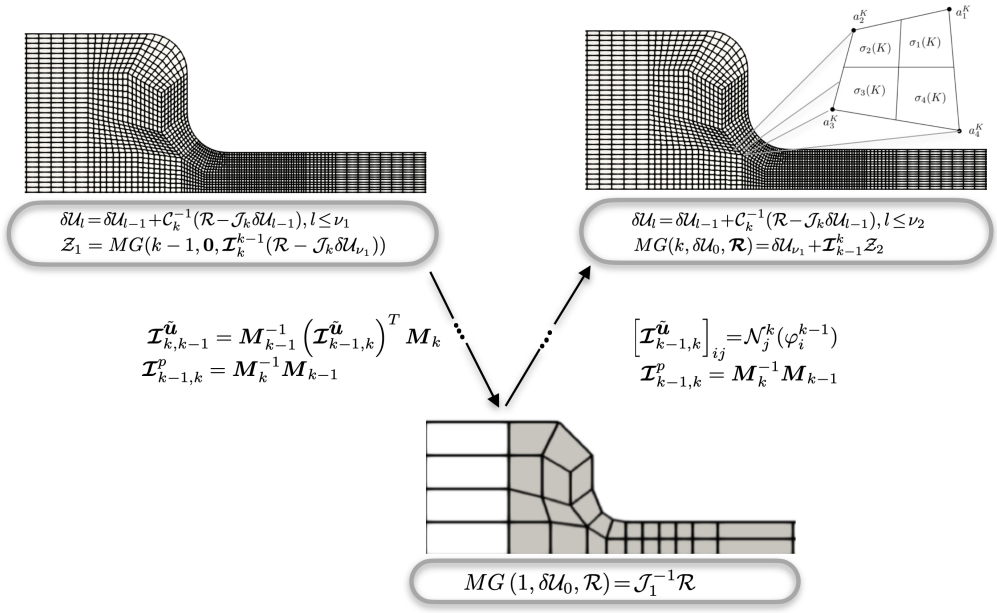

Fig. 3.3: **Monolithic Geometric MG solver:** Multigrid algorithm on a mesh-slice of 4:1 contraction configuration.

We present the details of the algorithm for different multigrid cycles as follows (for details we refer to the work [21]):
For $k = 1$ on the coarsest level, the direct solver is used

$$MG(1, \delta\mathcal{U}_0, \mathcal{R}) = \mathcal{J}_1^{-1}\mathcal{R}. \tag{3.28}$$

For $k > 1$, there are three steps.
Pre-smoothing step. Let $\delta\mathcal{U}^l \in \mathcal{V}_k$ be defined by

$$\delta\mathcal{U}^l = \delta\mathcal{U}^{l-1} + \mathcal{C}_k^{-1}\left(\mathcal{R} - \mathcal{J}_k\delta\mathcal{U}^{l-1}\right), \quad 1 \le l \le \nu_1. \tag{3.29}$$

where $\rho(\mathcal{C}_k^{-1}\mathcal{J}_k) \le \rho(\mathcal{J}_k)$, and ρ denotes the spectral radius.
Correction step. Let $\tilde{\mathcal{R}} = \boldsymbol{\mathcal{I}}_k^{k-1}(\mathcal{R} - \mathcal{J}_k\delta\mathcal{U}_{\nu_1})$ and $\mathcal{Z}_i \in \mathcal{V}_{k-1}$, $0 \le i \le p, p = 1$ or $p = 2$, be defined as $\mathcal{Z}_0 = 0$,

For V-cycle

$$\mathcal{Z}_1 = MG_V(k-1, \mathcal{Z}_0, \tilde{\mathcal{R}}), \tag{3.30}$$

For W-cycle

$$\begin{aligned} \mathcal{Z}_1 &= MG_W(k-1, \mathcal{Z}_0, \tilde{\mathcal{R}}), \\ \mathcal{Z}_2 &= MG_W(k-1, \mathcal{Z}_1, \tilde{\mathcal{R}}), \end{aligned} \tag{3.31}$$

which is the result of applying in the coarse grid correction step the $(k-1)^{th}$ level algorithm twice.

For F-cycle

$$\begin{aligned} \mathcal{Z}_1 &= MG_F(k-1, \mathcal{Z}_0, \tilde{\mathcal{R}}), \\ \mathcal{Z}_2 &= MG_V(k-1, \mathcal{Z}_1, \tilde{\mathcal{R}}), \end{aligned} \tag{3.32}$$

which results of applying in the coarse grid correction step the $(k-1)^{th}$ level F-cycle algorithm once, and then the $(k-1)^{th}$ level V-cycle algorithm once.

Final output:

$$MG(k, \delta\mathcal{U}_0, \mathcal{R}) = \delta\mathcal{U}_{\nu_1} + \boldsymbol{\mathcal{I}}_{k-1}^{k}\mathcal{Z}_p, \quad (p = 1 \text{ or } p = 2). \tag{3.33}$$

Post-smoothing step. Let $\delta\mathcal{U}^l \in \mathcal{V}_k$ be defined by

$$\delta\mathcal{U}^l = \delta\mathcal{U}^{l-1} + \mathcal{C}_k^{-1}\left(\mathcal{R} - \mathcal{J}_k\delta\mathcal{U}^{l-1}\right), \quad 1 \le l \le \nu_2. \tag{3.34}$$

Remark 8. For $p = 1$ we get the standard V(ν_1, ν_2)-cycle, while for $p = 2$ we get W(ν_1, ν_2)-cycle, resp. F(ν_1, ν_2)-cycle, by applying in the coarse grid correction step the $(k-1)^{th}$ level algorithm twice, resp. the $(k-1)^{th}$ level F-cycle algorithm once, and then the $(k-1)^{th}$ level V-cycle algorithm once [20, 21].

We proceed now, in Subsection §3.5.2, with intergrid transfer operators concretized to our FEM discretization choice, Q_2 and P_1^{disc}. We present the operators, restrictions and prolongations, in a geometric context with a clear mathematical formulation for further analysis of multigrid properties, which goes beyond the interest of the current thesis.

3.4.2 Grid Transfer Operators

Multigrid method requires intergrid transfer operators mapping data between the grid hierarchy $\mathcal{T}_{h_k}$ and $\mathcal{T}_{h_{k-1}}$. We are using geometric transfer between FE spaces [70, 71]. The coarse-to-fine grid (prolongation) operator $\mathcal{I}_{k-1}^{k}$ maps functions defined on the coarser grid level $k-1$ into a functions defined on a finer grid level k, while the fine-to-coarse grid (restriction) operator $\mathcal{I}_{k}^{k-1}$ maps functions defined on the finer grid level k into functions defined on a coarser grid level $k-1$.

$$\mathcal{I}_k^{k-1} = (\mathcal{I}_{k,k-1}^{\tilde{\boldsymbol{u}}}, \mathcal{I}_{k,k-1}^{p}) \tag{3.35}$$

$$\mathcal{I}_{k-1}^{k} = (\mathcal{I}_{k-1,k}^{\tilde{\boldsymbol{u}}}, \mathcal{I}_{k-1,k}^{p}) \tag{3.36}$$

where

$$\begin{aligned} &\mathcal{I}^{\tilde{\boldsymbol{u}}}_{k,k-1} : \mathbb{W}_{h_k} \longrightarrow \mathbb{W}_{h_{k-1}}, \quad \mathcal{I}^{\tilde{\boldsymbol{u}}}_{k-1,k} : \mathbb{W}_{h_{k-1}} \longrightarrow \mathbb{W}_{h_k}, \\ &\mathcal{I}^{p}_{k,k-1} : \mathbb{Q}_{h_k} \longrightarrow \mathbb{Q}_{h_{k-1}}, \quad \mathcal{I}^{p}_{k-1,k} : \mathbb{Q}_{h_{k-1}} \longrightarrow \mathbb{Q}_{h_k}. \end{aligned} \tag{3.37}$$

The prolongation operator, $\mathcal{I}^{\tilde{\boldsymbol{u}}}_{k-1,k} : \mathbb{W}_{h_{k-1}} \longrightarrow \mathbb{W}_{h_k}$, is the coarse-to-fine grid mapping for velocity and microstructure.

Velocity and microstructure fields. Since we approximate velocity and microstructure with conforming quadratic finite element, the finite element space on a coarser level is a subspace of the finite element space on a finer level $\mathbb{W}_{h_{k-1}} \subset \mathbb{W}_{h_k}$ $(k \geq 1)$. Therefore, $\mathcal{I}^{\tilde{\boldsymbol{u}}}_{k-1,k}$ is the natural embedding of $\mathbb{W}_{h_{k-1}}$ into $\mathbb{W}_{h_k}$ in $L^2(\Omega)$. Furthermore, any coarse grid function $\tilde{\boldsymbol{u}}_{k-1} \in \mathcal{W}_{k-1}$ can be expressed in terms of fine grid basis functions

$$\tilde{\boldsymbol{u}}_{k-1} = \sum_{j=1}^{\mathtt{dim}\mathbb{W}_{h_{k-1}}} \tilde{\boldsymbol{u}}_{j,k-1}\varphi^{k-1}_j = \sum_{j=1}^{\mathtt{dim}\mathbb{W}_{h_k}} \tilde{\boldsymbol{u}}_{j,k}\varphi^{k}_j. \tag{3.38}$$

Using the dual basis, $\{\mathcal{N}^k_i, i = 1, \ldots, \mathtt{dim}\mathbb{W}_{h_k}\}$, associated with the basis $\{\varphi^k_i, i = 1, \ldots, \mathtt{dim}\mathbb{W}_{h_k}\}$ of FE space $\mathbb{W}_{h_k}$, that is

$$\mathcal{N}^k_j(\varphi^k_i) = \delta_{ij}, \; \forall \; i, j = 1, \ldots, \mathtt{dim}\mathbb{W}_{h_k}$$

where δ_{ij} is the Kronecker delta function, we get

$$\tilde{\boldsymbol{u}}_{i,k} = \sum_{j=1}^{\mathtt{dim}\mathbb{W}_{h_{k-1}}} \tilde{\boldsymbol{u}}_{j,k-1}\mathcal{N}^k_j(\varphi^{k-1}_i). \tag{3.39}$$

The entries of its matrix representation $\boldsymbol{\mathcal{I}}^{\tilde{\boldsymbol{u}}}_{k-1,k} \in \mathcal{W}_k \times \mathcal{W}_{k-1}$ are, the coarse grid shape functions evaluated at the fine-grid vertices,

$$\left[\boldsymbol{\mathcal{I}}^{\tilde{\boldsymbol{u}}}_{k-1,k}\right]_{ij} = \mathcal{N}^k_j(\varphi^{k-1}_i). \tag{3.40}$$

The restriction operator, $\mathcal{I}^{\tilde{\boldsymbol{u}}}_{k,k-1} : \mathbb{W}_{h_k} \longrightarrow \mathbb{W}_{h_{k-1}}$, is the fine-to-coarse grid mapping for microstructure and velocity. We use the L^2-projection. Its matrix representation, $\boldsymbol{\mathcal{I}}_{k,k-1}$ with respect to the basis $\{\varphi^{k-1}_i, i = 1, \ldots, \mathtt{dim}\mathbb{W}_{h_{k-1}}\}$ and $\{\varphi^k_i, i = 1, \ldots, \mathtt{dim}\mathbb{W}_{h_k}\}$ is obtained using the embedding $\mathcal{I}^k_{k-1}$ as follows:

$$\boldsymbol{\mathcal{I}}^{\tilde{\boldsymbol{u}}}_{k,k-1} = \mathbf{M}^{-1}_{k-1}(\boldsymbol{\mathcal{I}}^{\tilde{\boldsymbol{u}}}_{k-1,k})^T\mathbf{M}_k \tag{3.41}$$

where $\mathbf{M}_{k-1}$ and $\mathbf{M}_k$ are mass matrices at level $k-1$ and k, respectively. Therefore, The transpose of the prolongation matrix is indeed the restriction matrix

$$\mathcal{R}_{k-1} = (\boldsymbol{\mathcal{I}}^{\tilde{\boldsymbol{u}}}_{k-1,k})^T\mathcal{R}_k. \tag{3.42}$$

Pressure field. The pressure is approximated by a discontinuous linear finite element, P^{disc}_1. Therefore, the multilevel FE approximation spaces for the pressure are nested, $\mathbb{Q}_{h_{k-1}} \subset \mathbb{Q}_{h_k}$. The prolongation operator for the pressure, $\mathcal{I}^p_{k-1,k} : \mathbb{Q}_{h_{k-1}} \longrightarrow \mathbb{Q}_{h_k}$, is defined in terms of the local L^2-inner product projection operator; for all $q \in P^{\text{disc}}_1(K)$ there holds $q \in P^{\text{disc}}_1(\sigma_l(K)), l = 1, \cdots, 2^d)$. Then,

$$\sum_{l=1}^{2^d} \int_{\sigma_l(K)} \mathcal{I}^p_{k-1,k} p_{k-1} q \, d\Omega = \int_K p_{k-1} q \, d\Omega, \qquad \forall K \in \mathcal{T}_{h_{k-1}}. \tag{3.43}$$

Its matrix representation is given in terms of the mass matrices with respect to the basis of $\mathbb{Q}_{h_k}$ and $\mathbb{Q}_{h_{k-1}}$ as follows:

$$\boldsymbol{\mathcal{I}}^{p}_{k-1,k} = \mathbf{M}_{k}^{-1}\mathbf{M}_{k-1}. \tag{3.44}$$

Indeed, let a coarse grid function $p_{k-1} \in \mathcal{Q}_{k-1}$, be expanded in terms of fine grid basis functions

$$p_{k-1} = \sum_{j=1}^{\dim\mathbb{Q}_{h_{k-1}}} p_{j,k-1}\psi_{j}^{k-1} = \sum_{j=1}^{\dim\mathbb{Q}_{h_{k}}} p_{j,k}\psi_{j}^{k}. \tag{3.45}$$

For each element $K \in \mathcal{T}_{h_{k-1}}$ and each basis function ψ_{i}^{k-1} of $P_{1}^{\text{disc}}(K)$, we have

$$\begin{aligned}\int_{\sigma_l(K)} p_{k-1}\psi_{i}^{k-1}\,d\Omega &= \sum_{j=1}^{\dim P_{1}^{\text{disc}}} p_{j,k-1}\int_{\sigma_l(K)}\psi_{j}^{k-1}\psi_{i}^{k-1}\,d\Omega, \quad \forall l = 1,\cdots,2^{d}\\ &= \sum_{j=1}^{\dim P_{1}^{\text{disc}}} p_{j,k}\int_{\sigma_l(K)}\psi_{j}^{k}\psi_{i}^{k-1}\,d\Omega, \qquad \forall l = 1,\cdots,2^{d}.\end{aligned} \tag{3.46}$$

Summing-up over the sub-elements, $\sigma_l(K)(l = 1,\cdots,2^{d})$, there holds

$$\sum_{j=1}^{\dim P_{1}^{\text{disc}}} p_{j,k-1}\int_{K}\psi_{j}^{k-1}\psi_{i}^{k-1}\,d\Omega = \sum_{l=1}^{2^{d}}\sum_{j=1}^{\dim P_{1}^{\text{disc}}} p_{j,k}\int_{\sigma_l(K)}\psi_{j}^{k}\psi_{i}^{k-1}\,d\Omega. \tag{3.47}$$

Hence,

$$\mathbf{M}_{k-1}p_{k-1|K} = \sum_{l=1}^{2^{d}}\mathbf{M}_{k}p_{k|\sigma_l(K)}. \tag{3.48}$$

We get the fine mesh coefficient vector, p_k, via the local mass matrices.

The restriction operator for the pressure, $\mathcal{I}^{p}_{k,k-1} : \mathbb{Q}_{h_k} \longrightarrow \mathbb{Q}_{h_{k-1}}$, is the transpose counterpart of the prolongation w.r.t. L^2; for all $K \in \mathcal{T}_{h_{k-1}}$ and $q \in P_{1}^{\text{disc}}(K)$

$$\int_{K}\mathcal{I}^{p}_{k,k-1}p_{k}q\,d\Omega = \sum_{l=1}^{2^{d}}\int_{\sigma_l(K)} p_{k}\,\mathcal{I}^{p}_{k-1,k}q\,d\Omega. \tag{3.49}$$

Its matrix representation is given in terms of the mass matrices with respect to the bases of $\mathbb{Q}_{h_k}$ and $\mathbb{Q}_{h_{k-1}}$ as follows:

$$\boldsymbol{\mathcal{I}}^{p}_{k,k-1} = \mathbf{M}_{k-1}^{-1}\mathbf{M}_{k}. \tag{3.50}$$

Remark 9. For velocity and microstructure fields, there is no need for the evaluation of neither the mass matrix $\mathbf{M}_{k-1}$ nor its inversion. In addition, the coarse grid matrix can be expressed in terms of the fine grid matrix as follows:

$$\mathcal{J}^{\tilde{\boldsymbol{u}}}_{k-1} = (\boldsymbol{\mathcal{I}}^{\tilde{\boldsymbol{u}}}_{k-1,k})^{T}\mathcal{J}^{\tilde{\boldsymbol{u}}}_{k}\boldsymbol{\mathcal{I}}^{\tilde{\boldsymbol{u}}}_{k-1,k}. \tag{3.51}$$

The pressure is cross-element wise disconnected. Thus, only the local mass matrices are in play.

Lastly, we continue with the presentation of the smoother steps in multigrid in Subsection §3.5.3. As we are bounded with the strong nonlinear coupling of the TVP problem, we are using Local pressure Schur complement approach to efficiently tackle flow fields coupling locally.

3.4.3 Local Pressure Schur Complement Approach

Local Pressure Schur complement (LPSC) schemes are generalizations of Vanka-type smoothers for coupled systems of typical saddle point type, which we encounter so far in TVP flow problems [76, 79]. They are simple iterative relaxation methods that solve directly on the element level, one element or a patch of elements, and perform an outer block Gauss-Seidel iteration. The choice of the blocks for such systems is based on the incompressibility constraint, or equivalently, on the pressure degrees of freedom. As a consequence, an efficient solver for the TVP problem is obtained due to the local character of the algorithm beside the global defect-correction mechanism on the one hand, and due to our choice for discontinuous FE discretization for the pressure on the other hand.

Here, we content to explain mathematically the mechanism of the LPSC approach for solving TVP problems [76, 79]. Since the choices of the blocks are based on the incompressibility constraint and due to noncoupling between the pressure and microstructure, we collocate the microstructure and velocity flow fields and rewrite the Jacobian, omitting the grid level indices, due to the level grid hierarchy independence of the smoothing steps, as follows:

$$\left(\frac{\partial \mathcal{R}(\mathcal{U})}{\partial \mathcal{U}}\right) = \begin{pmatrix} \dfrac{\partial \mathcal{R}_{\tilde{\boldsymbol{u}}}(\tilde{\boldsymbol{u}})}{\partial \tilde{\boldsymbol{u}}} & \dfrac{\partial \mathcal{R}_{\tilde{\boldsymbol{u}}}(\tilde{\boldsymbol{u}})}{\partial p} \\ \dfrac{\partial \mathcal{R}_{p}(\tilde{\boldsymbol{u}})}{\partial \tilde{\boldsymbol{u}}} & 0 \end{pmatrix}. \tag{3.52}$$

In order to set the local subproblems, we introduce prolongation operators, indexed by element K, for coupled velocity and microstructure field, denoted by $\mathcal{P}_K^{\tilde{\boldsymbol{u}}}$,

$$\mathcal{P}_K^{\tilde{\boldsymbol{u}}} : \mathbb{W}_h(K) \longrightarrow \mathbb{W}_h, \quad \forall\ K \in \mathcal{T}_h, \tag{3.53}$$

and for the pressure field, denoted by $\mathcal{P}_K^{p}$,

$$\mathcal{P}_K^{p} : \mathbb{Q}_h(K) \longrightarrow \mathbb{Q}_h, \quad \forall\ K \in \mathcal{T}_h. \tag{3.54}$$

For the prolongation pair $\mathcal{P}_K = (\mathcal{P}_K^{\tilde{\boldsymbol{u}}}, \mathcal{P}_K^{p})$ for coupled, velocity and microstructure fields, and the pressure field, we introduce the corresponding restriction operator pair $\mathcal{P}_K^{\mathrm{T}} = ({\mathcal{P}_K^{\tilde{\boldsymbol{u}}}}^{\mathrm{T}}, {\mathcal{P}_K^{p}}^{\mathrm{T}})$ defined for the global solutions as

$$\mathcal{P}_K^{\mathrm{T}} : \mathbb{W}_h \times \mathbb{Q}_h \longrightarrow \mathbb{W}_h(K) \times \mathbb{Q}_h(K), \quad \forall\ K \in \mathcal{T}_h. \tag{3.55}$$

Firstly, since velocity and microstructure flow fields are approximated with conforming Q_2 FE discretization, they are laying on the same degree of freedom. Furthermore, using conforming FE approximations on the one hand, and the jump stabilization on the other, we are in the situation of an overlapping of corresponding spaces of degrees of freedom $\mathbb{W}_h(K)\ \forall K \in \mathcal{T}_h$, that is

$$\begin{cases} \mathbb{W}_h(K) \subset\ \mathbb{W}_h, \mathbb{W}_h = \underset{K\in\mathcal{T}_h}{\cup} \mathbb{W}_h(K), \\ \forall\ K \in \mathcal{T}_h, \exists \tilde{K} \neq\ K \mid \mathbb{W}_h(K) \underset{K\neq\tilde{K}}{\cap} \mathbb{W}_h(\tilde{K}) \neq \emptyset. \end{cases} \tag{3.56}$$

Secondly, using discontinuous FE discretization for the pressure leads to nonoverlapping of spaces of degrees of freedom of $\mathbb{Q}_h(K)\ \forall K \in \mathcal{T}_h$, that is

$$\begin{cases} \mathbb{Q}_h(K) \subset\ \mathbb{Q}_h, \mathbb{Q}_h = \underset{K\in\mathcal{T}_h}{\cup} \mathbb{Q}_h(K), \\ \mathbb{Q}_h(K) \underset{K\neq\tilde{K}}{\cap} \mathbb{Q}_h(\tilde{K}) = \emptyset \quad \forall\ K \in \mathcal{T}_h. \end{cases} \tag{3.57}$$

Let $\boldsymbol{\mathcal{P}}_K^{\tilde{\boldsymbol{u}}}$, $\boldsymbol{\mathcal{P}}_K^{p}$, and $\boldsymbol{\mathcal{P}}_K$ denote matrix representations, that is, the algebraic counterparts of prolongations $\mathcal{P}_K^{\tilde{\boldsymbol{u}}}$, $\mathcal{P}_K^{p}$, and $\mathcal{P}_K$, defined on spaces of variables values $\mathcal{W}_K := \mathbb{R}^{\dim \mathbb{W}_K}$, $\mathcal{Q}_K := \mathbb{R}^{\dim \mathbb{Q}_K}$, and $\mathcal{V}_K := \mathcal{W}_K \times \mathcal{Q}_K$, respectively. Thus, the values for the local solutions in terms of local restriction matrices are given as follows (for details see [69]):

$$\mathcal{U}_K = (\tilde{\boldsymbol{u}}_K, p_K) := \boldsymbol{\mathcal{P}}_K^{\mathrm{T}} \mathcal{U} = ({\boldsymbol{\mathcal{P}}_K^{\tilde{\boldsymbol{u}}}}^{\mathrm{T}} \tilde{\boldsymbol{u}}, {\boldsymbol{\mathcal{P}}_K^{p}}^{\mathrm{T}} p). \tag{3.58}$$

Similarly, the values for the global solution are assembled using the local prolongation matrices as

$$\mathcal{U} = (\tilde{\boldsymbol{u}}, p) = \sum_{K \in \mathcal{T}_h} \boldsymbol{\mathcal{P}}_K \mathcal{U}_K = \sum_{K \in \mathcal{T}_h} (\boldsymbol{\mathcal{P}}_K^{\tilde{\boldsymbol{u}}} \tilde{\boldsymbol{u}}, \boldsymbol{\mathcal{P}}_K^{p} p). \tag{3.59}$$

The overlapped solutions, in the assembling process (3.59), are updated in a Gauss-Seidel manner [69]. Then, the smoothing steps in a monolithic geometric multigrid are simple block Gauss-Seidel iteration. In compact form, it reads:

$$\mathcal{U}^{l+1} = \mathcal{U}^{l} - \omega_l \sum_{K \in \mathcal{T}_h} \boldsymbol{\mathcal{P}}_K \left(\left(\boldsymbol{\mathcal{P}}_K^{\mathrm{T}} \left(\frac{\partial \mathcal{R}(\mathcal{U}^l)}{\partial \mathcal{U}} \right) \boldsymbol{\mathcal{P}}_K \right)^{-1} \boldsymbol{\mathcal{P}}_K^{\mathrm{T}} \mathcal{R}(\mathcal{U}^l) \right). \tag{3.60}$$

In practice, the local residuum is calculated, using restriction (3.58),

$$\mathcal{R}_K(\mathcal{U}^l) = \boldsymbol{\mathcal{P}}_K^{\mathrm{T}} \mathcal{R}(\mathcal{U}^l). \tag{3.61}$$

Then, we obtain the linear local matrices

$$\left(\frac{\partial \mathcal{R}(\mathcal{U}^l)}{\partial \mathcal{U}} \right)_K = \boldsymbol{\mathcal{P}}_K^{\mathrm{T}} \left(\frac{\partial \mathcal{R}(\mathcal{U}^l)}{\partial \mathcal{U}} \right) \boldsymbol{\mathcal{P}}_K, \tag{3.62}$$

to solve for the local updates by means of solving the local subproblems

$$\left(\frac{\partial \mathcal{R}(\mathcal{U}^l)}{\partial \mathcal{U}} \right)_K \delta \mathcal{U}_K^l = \mathcal{R}_K(\mathcal{U}^l). \tag{3.63}$$

We obtain the global update, using the prolongation (3.59),

$$\delta \mathcal{U}^l = \sum_{K \in \mathcal{T}_h} \boldsymbol{\mathcal{P}}_K \delta \mathcal{U}_K^l, \tag{3.64}$$

and, finally we update the solutions with a certain damping parameter ω_l

$$\mathcal{U}^{l+1} = \mathcal{U}^{l} - \omega_l \delta \mathcal{U}^l. \tag{3.65}$$

Remark 10. Note that the local subproblem is of the saddle point type. Furthermore, due to the jump stabilization contributions, the local matrices for velocity and microstructure are deduced from a patch of elements, that is, the designated element by pressure and all its neighbors. In order to keep the size of the local subproblem of a small size, one might only include the jump contributions within the designated element by pressure [62, 77].

3.5 Concluding Remarks

In this chapter, we presented a monolithic Newton-multigrid FEM solver for the quasi-Newtonian modeling approach for thixoviscoplastic flows.

Based on a two-fields Stokes solver, we used higher order stable Q_2/P_1^{disc} FE discretization for velocity and pressure. Then, we approximated the microstructure field similar as the velocity field, using the higher order Q_2 FE approximation, with an appropriate stabilization term to enhance the coercivity for the microstructure weak formulation. The bilinear stabilization term consists of edge-oriented jump of the gradient to upgrade the coercivity to match the space norm. Additionally, it is consistent with FEM discretization, linear with respect to the problem, and improves the solver's efficiency.

The FEM quasi-Newtonian model for thixoviscoplastic flows is a highly nonlinear multifield coupled problem. The extended viscosity for generalized TVP Stokes equations is dependent on flow fields, by means of shear rate and microstructure, and the regularization parameter. And the thixotropic model is dependent on the shear rate. As a consequence, the FEM quasi-Newtonian modeling approach requires a robust solver to obtain accurate numerical solutions.

Firstly, we used a combined adaptive discrete Newton and monolithic geometric multigrid solver to delicately handle the regularization and to treat the nonlinearity multifield coupled issues alike. The solver has two folds with respect to adaptivity; the one related to discrete Newton's method is done via the step-size in finite difference approximation of the Jacobian, while the one related to the linear multigrid solver is achieved by requiring the optimal convergence according to the nonlinear one. The resultant solver is a black box solely dependent on the actual rate of the nonlinear residual convergence, singularity-free, and robust with respect to the starting guess.

Secondly, we advantageously concretized the monolithic geometric multigrid solver on FEM discretization choice used so far. It is based on the local pressure Schur complement (LPSC) approach to handle the coupled linearized TVP saddle point problems locally. That is, to solve exactly on the element level, one element or a patch of elements, and perform an outer block Gauss-Seidel iteration. The choice of the blocks for block Gauss-Seidel iteration is based on the pressure degrees of freedom P_1^{disc}. The local character of this procedure together with the global defect-correction mechanism on the one hand, and the choice of discontinuous FE approximations for the pressure on the other, results in an efficient linear solver.

Summarising, we developed a solver for TVP generalized Stokes equations. The developed solver is black box, and based on the monolithic Newton-multigrid method. It uses an adaptive strategy for the step-size control in divided difference for the Jacobian approximation. The size of step length follows the convergence process via the actual residual convergence rate. Accordingly, the multigrid convergence is made optimal to achieve the nonlinear convergence. To conclude, the combination of pair Q_2/P_1^{disc} FEM discretization together with an adaptive Newton-multigrid solver results in a highly numerically accurate, robust, and efficient solution scheme.

4

Numerical Simulations of Thixoviscoplastic Flows

This chapter is concerned with numerical simulations of thixoviscoplastic flow problems as a useful tool to understand the complex phenomena of the interplay between plasticity and thixotropy. Thixoviscoplastic flow is a multifield coupled nonlinear problem, beside the integrated nonlinearity within the momentum equation and microstructure equation, it induces two-way coupling, by means of microstructure dependent plastic-viscosity and yield stress as well as shear rate dependent buildup and breakdown functions, and microstructure convection. We have selected, for our numerical simulations, flow configurations of academic background, modeling interest, and industrial applications, that extend the CFD simulations (as for instance [34, 37, 39]) to include TVP flow problems.

4.1 Introduction

Incorporating thixotropy in complex flow processes necessitates flow simulations in a wide range of circumstances. In this regard, we provide thixoviscoplastic flow simulations in different flow configurations. Firstly, we start with a channel flow as a means to validate our numerical solutions and algorithmic tools. We use the unidirectional flow assumptions for fully developed flow to generate data from a reduced one-dimensional corresponding Houška TVP model, to be used as necessary boundary conditions (inflow boundary conditions), alternative boundary conditions at the outflow (Dirichlet instead of "do-nothing"), and a solution's validation mechanism at each x-axis cross section.
Secondly, we move to lid-driven cavity flow as an important benchmark for several computational fluid dynamics codes in academia. We investigate different flow regimes. We start with the analysis of Newtonian case for a wide range of Reynolds number to track the nonuniformities of the flow in the absence of any regularization effects. Then, we use the viscoplastic model to optimize the settings for mesh refinement and regularization parameter for model accuracy. With these optimized settings, we investigate the accurate growth and location of unyielded regions, and the role played by the microstructure equation throughout the analysis of the types of transitions between yielded and unyielded regions. We provide the corresponding analysis of Newton-multigrid solver convergence.
Thirdly, we present thixotropic flow in a simple enough geometry for laboratory experiments and for numerical simulation validation, Couette device. We study the types of transitions from a quasi-static flow regime to an intermediate flow regime and vice versa, with respect to the changes in the intensity of breakdown parameter.
Lastly, we choose the contraction domain as a close enough configuration for industrial and engineering applications, and its utility in applied mathematics and simulation communities to develop efficient numerical methods and practical algorithms. We use this flow configuration to analyze the thixotropic phenomena, namely the competition processes of *Aging* and *Shear Rejuvenation*.

4.2 Thixoviscoplastic Channel Flow

In this section, we are concerned with thixoviscoplastic channel flow as a means to validate our numerical solutions and algorithmic tools. Unidirectional flow is an inevitable assumption to generate exact solutions for many nonlinear flow problems in certain circumstances.

As far as the numerical simulations of thixoviscoplastic flow problems are concerned, the inflow boundary conditions are required for the microstructure equation on the one hand, and a validation mechanism for the numerical solutions and algorithmic tools on the other. Manufacturing analytic solution for thixoviscoplastic flow is beyond our interest. Indeed, thixoviscoplastic flow problems are multifield coupled nonlinear problems, beside the integrated nonlinearity within the momentum equation and microstructure equation, thixoviscoplastic problems induce a two-way coupling, by means of microstructure dependent plastic-viscosity and yield stress as well as shear rate dependent breakdown functions and microstructure convection. Thus, we opt for the fully developed solutions as boundary data for our finite element simulations due to the nonavailability of Houška thixoviscoplastic analytical solution.
To calculate the fully developed solutions, we assume a x-axis unidirectional flow. From these assumptions, we rewrite a reduced one-dimensional generalized Stokes Houška thixoviscoplastic model to generate fully developed discrete data solutions. The fully developed discrete data solutions of the reduced one-dimensional generalized Stokes Houška TVP model are used to provide necessary boundary conditions (inflow boundary conditions), alternative boundary conditions at the outflow (Dirichlet instead of "do-nothing" [44] or any version of it from [4, 16, 14, 18, 40, 38, 74]), and a solution's validation mechanism at each x-axis cross section of the channel domain.

With respect to the quasi-Newtonian modeling approach, regularization is a common issue for both viscoplastic and thixoviscoplastic flow problems. Indeed, the impact of regularization of viscoplastic subproblems is replicated in thixoviscoplastic flow problems. In addition, manufacturing an analytical solution for unidirectional viscoplastic is achievable. Thus, we use the simplified viscoplastic unidirectional flow as a base for mechanism for accurate solutions with respect to regularization. In the next subsection, we investigate the regularization impact on viscoplastic flow with the help of an analytical solution.

4.2.1 Bingham Viscoplastic Channel Flow

This subsection is devoted to viscoplastic channel flow. It is considered here as a benchmark for a quasi-Newtonian modeling approach. Owning an exact solution, viscoplastic channel flow plays a key role, in the context of this work, as a validation tool for the quasi-Newtonian approach for thixoviscoplastic flow.

Quasi-Newtonian modeling approach for yield stress materials uses an approximated norm of shear rate with a regularization parameter, which may cause the solutions to be regularization dependent. In this subsection §4.2.1, we investigate the accuracy of the FEM regularized viscoplastic channel flow solution against the exact viscoplastic solution, to come up with optimal settings for the regularization parameter. We select two classical regularizations, namely Bercovier-Engelmann regularization, and Papanastasiou regularization, for the investigations of accuracy via calculation of the L^2-norm of the error for different yield stress parameter. Furthermore, for both regularizations, we analyze the solver behavior with respect to mesh refinement and regularization parameter.

We consider a unit channel configuration, with boundary $\partial\Omega$ with inflow section, denoted Γ^-, outflow boundary section Γ^+, and upper and lower walls Γ. Exact Bingham viscoplastic solution for velocity $\boldsymbol{u}_{ex} = (u, 0)^{\mathrm{T}}$ in a unit channel is given as follows;

$$u = \begin{cases} \dfrac{1}{8}\left((1-2\tau_0)^2 - (1-2\tau_0-2y)^2\right) & \text{if } y \in [0, \dfrac{1}{2}-\tau_0) \\ \dfrac{1}{8}(1-2\tau_0)^2 & \text{if } y \in [\dfrac{1}{2}-\tau_0, \dfrac{1}{2}+\tau_0] \\ \dfrac{1}{8}\left((1-2\tau_0)^2 - (2y-2\tau_0-1)^2\right) & \text{if } y \in (\dfrac{1}{2}+\tau_0, 1] \end{cases} \tag{4.1}$$

The analytical solution corresponds to the unyieded region in the center of the channel $y \in [\frac{1}{2}-\tau_0, \frac{1}{2}+\tau_0]$, which increases with the increase of the yield stress parameter τ_0. Two yielded regions, which decrease with the increase of yield stress parameter τ_0, separate the unyielded region from the channel's walls. The plastic-viscosity η_0 is set equal to unity, and the range of yield stress parameter values lies between zero and one-half. For the highest value of yield stress τ_0 set equal to one-half, the unyielded region occupies the full domain, while on the other extremity, the yielded region occupies the full domain. The shear stress on the unyielded region belongs to a ball centred at the origin with a radius value of yield stress parameter τ_0, while the pressure on the yielded regions obeys the Poiseuille law, that is $\nabla p = (-1, 0)^{\mathrm{T}}$.

The first numerical simulation aims to test the response of the regularized FEM solution with respect to the yield stress parameter over a wide spectrum of values within its admissible range. We plot, in Figure 4.1, the velocity magnitude at the vertical centerline for a set of yield stress parameter values. The simulations are done with Papanastasiou's regularized viscosity function, where the regularization parameter k is set equal to 10^3.

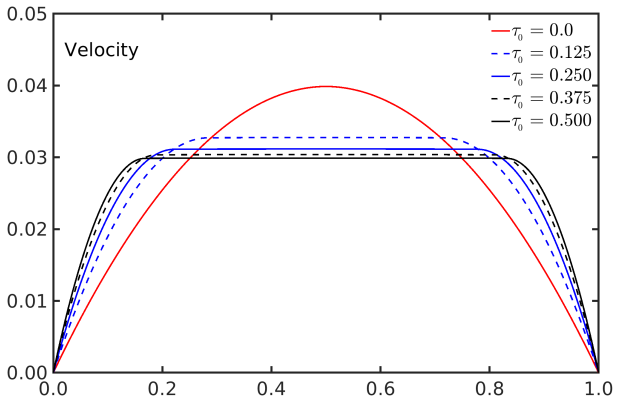

Fig. 4.1: **Viscoplastic channel flow:** Impact of yield-stress parameter τ_0 on velocity profiles across the line, $y = 0.5$, via Papanastasiou regularization at $k = 10^3$, where $\eta_0 = 1.0$ and grid refinement size $h = 0.03125$.

Clearly, for a vanishing yield stress parameter, the flow is Newtonian-like and shows the perfect parabolic profile. As we increase the yield stress parameter, the peak of the parabolic profile gets flattened respectively in the unyielded region. Now, we proceed with our settled goal for this benchmark problem to analyze the impact of the regularization parameter on the accuracy of solutions.

For our regularized FEM solutions, we take the exact Bingham viscoplastic solution (4.1) as Dirichlet boundary conditions on $\partial\Omega$, with a homogeneous source term. The smoothed constitutive equation defined

with the help of the extended viscosity on one hand, and the exact solution (4.1) as Dirichlet boundary conditions on $\partial\Omega$, and a homogeneous source term on the other hand, yields the constant pressure solution in the unyielded region. Thus, a linear pressure on the yielded regions and a constant pressure in the unyielded region, increase the benchmark challenges with respect to pressure FEM approximation, and resolving interfaces with respect to mesh. This is a classical issue within multiphase problems [28, 46, 78, 83]. Alternatively, one might go for a solution with linear pressure on all regions for this benchmark. To achieve this goal, one may either monitor the source term with exact Bingham solution (4.1) as Dirichlet boundary conditions on $\partial\Omega$, or apply a pressure drop as boundary conditions between the inflow boundary section Γ^- and the outflow boundary section Γ^+ and homogeneous Dirichlet boundary conditions on the boundary section Γ.

The numerical FEM simulations yield a flow distribution of the flow field and calculated quantities. We display the solutions (velocity, pressure, and shear rate) for different boundary conditions. In Figure 4.2 (TOP), we show the solutions obtained with the analytical Bingham viscoplastic solution (4.1) as Dirichlet boundary conditions on $\partial\Omega$, with homogeneous source term. Furthermore, with pressure drop as boundary conditions, the solutions are displayed in Figure 4.2 (BOTTOM).

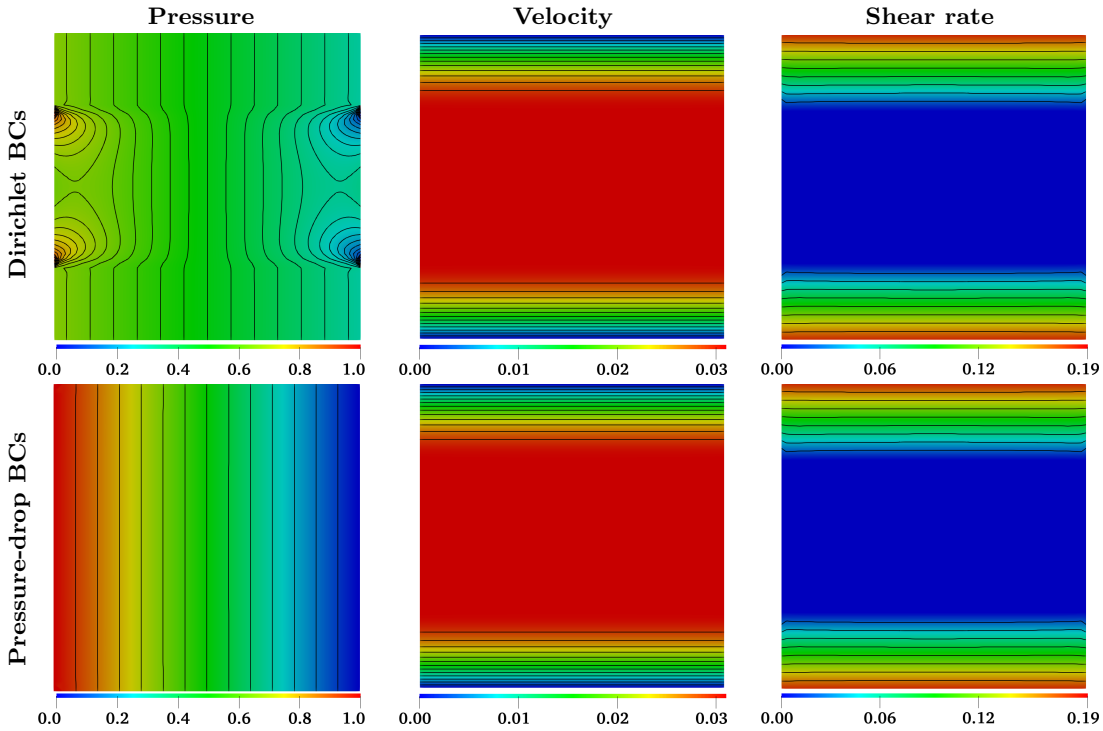

Fig. 4.2: **Bingham viscoplastic channel flow:** Bingham viscoplastic flow solutions, where $\eta_0 = 1.0$,$\tau_0 = 0.25$, $k = 10^4$.

The pressure solution for a regularized viscoplastic problem with analytical Bingham viscoplastic solution (4.1) as Dirichlet boundary conditions on $\partial\Omega$, and the homogeneous source term, shows discontinuity between regions, and jumps at the intersections of boundary sections Γ^- and Γ^+ with the interfaces. In contrast, the pressure driven flow shows a perfect linear pressure solution. It is worth mentioning that the well-known artifacts related to the 'do-nothing' boundary condition associated with pressure drop are removed simply by setting the y-velocity to zero at the boundary to remain with the unidirectional flow

assumptions, for details about this issue and possible remedies, we refer to [18, 44]. For both problems, the unyielded region is moving at a constant velocity, and is separated from the wall's channel by yielded regions. The shear rate follows the regions accordingly, particularly the zero-shear rate for the unyielded region at the center of the channel.

Before proceeding quantitatively with the investigation of the impact of regularization within the viscoplastic quasi-Newtonian modeling approach, we show qualitatively the regularization effect on velocity, pressure, and shear rate solutions in Figure 4.3. The simulation corresponds to Bingham's analytical solution (4.1) as Dirichlet boundary conditions on $\partial\Omega$, with a homogeneous source term. From Figure 4.3,

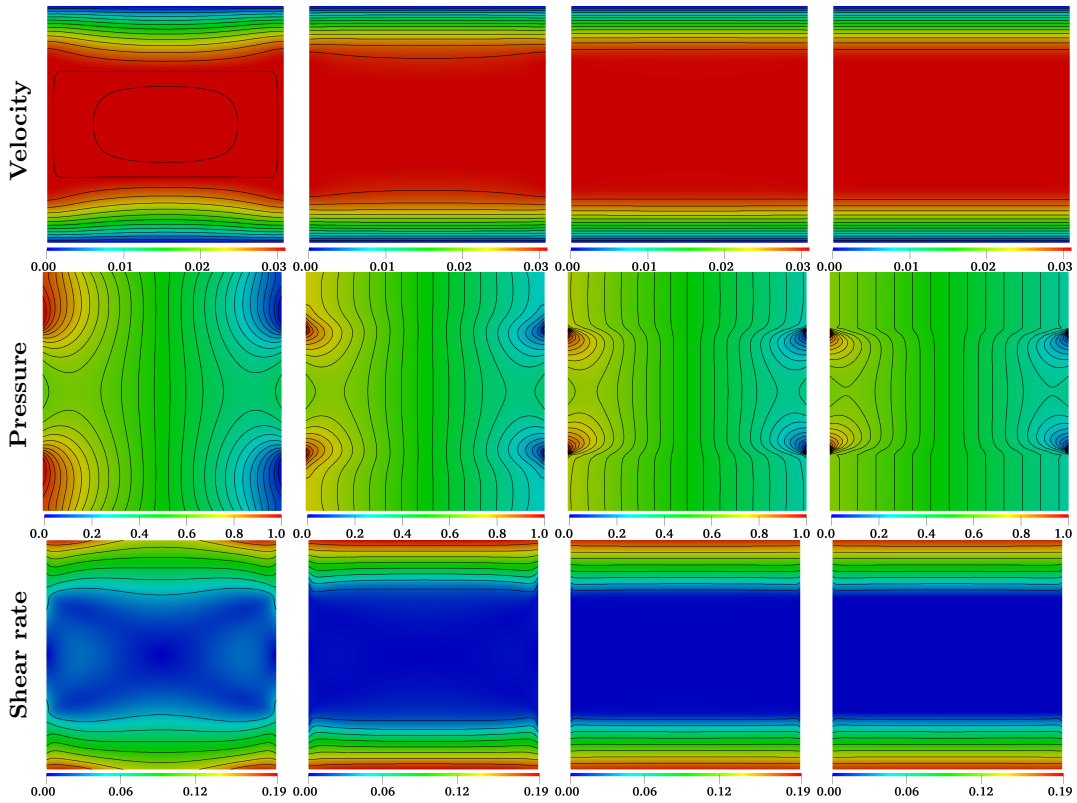

Fig. 4.3: **Viscoplastic channel flow:** Impact of Papanastasiou's regularization on flow solutions, for $\tau_0 = 0.25$ and $\eta_0 = 1.0$. The simulations are done for $k = 10^1$, 10^2, 10^3, 10^4 (LEFT to RIGHT), at grid refinement size $h = 0.03125$.

as the regularization parameter increases, the prescribed boundary conditions (which correspond to Bingham's analytical solution) are preserved along the channel to perfectly match the prescribed exact solution in full domain for the higher values of the regularization parameter. Next, we check quantitatively, via error analysis, the impact of regularization on the accuracy of solutions.

We proceed with the investigation of impact of the regularization on the accuracy of the solutions. To remain aligned with our goal fixed for this flow benchmark, we choose the yield stress parameter for our simulations with care to avoid that the interface crosses an element, that is, an aligned interface with the quadrilateral mesh. For the completeness of the exposure, we also provide simulations with a yield stress parameter which leads to an interface crossing element, that is, a nonaligned interface with the quadrilateral mesh.

We carry out the simulations with both Bercovier-Engelmann and Papanastasiou regularizations, and provide the corresponding velocity errors in Table 4.1 for two yield stress parameter values, which provide a solution with mesh-aligned interfaces between unyielded and yield regions.

Table 4.1: **L^2-error of velocity $\|\boldsymbol{u} - \boldsymbol{u}_{ex}\|_2$:** Velocity errors in the L^2-norm for Bingham viscoplastic flow for different values of the yield stress parameter.

$k\backslash L$	2	3	4	5	6
	$\underline{\tau_0 = 0.25}$				
	Bercovier-Engelmann Regularization				
10^{-1}	2.978095×10^{-3}	2.951861×10^{-3}	2.950375×10^{-3}	2.950330×10^{-3}	2.950331×10^{-3}
10^{-2}	6.901916×10^{-4}	6.913878×10^{-4}	6.802920×10^{-4}	6.793066×10^{-4}	6.793291×10^{-4}
10^{-3}	7.445251×10^{-5}	7.472293×10^{-5}	7.681642×10^{-5}	7.669420×10^{-5}	7.624363×10^{-5}
10^{-4}	7.682888×10^{-6}	7.497608×10^{-6}	7.471700×10^{-6}	7.553686×10^{-6}	7.652252×10^{-6}
10^{-5}	7.712732×10^{-7}	7.513904×10^{-7}	7.461318×10^{-7}	7.475360×10^{-7}	7.511636×10^{-7}
10^{-6}	7.715786×10^{-8}	7.515695×10^{-8}	7.461032×10^{-8}	7.470957×10^{-8}	7.470612×10^{-8}
	Papanastasiou Regularization				
10^{1}	3.007423×10^{-3}	2.986835×10^{-3}	2.985134×10^{-3}	2.985008×10^{-3}	2.985049×10^{-3}
10^{2}	8.070790×10^{-4}	7.910534×10^{-4}	7.771159×10^{-4}	7.766747×10^{-4}	7.766779×10^{-4}
10^{3}	8.854564×10^{-5}	8.713851×10^{-5}	8.999407×10^{-5}	8.962862×10^{-5}	8.876830×10^{-5}
10^{4}	9.265935×10^{-6}	8.958942×10^{-6}	8.871151×10^{-6}	8.863787×10^{-6}	8.919511×10^{-6}
10^{5}	9.311507×10^{-7}	8.991498×10^{-7}	8.892617×10^{-7}	8.868517×10^{-7}	8.860986×10^{-7}
10^{6}	9.316114×10^{-8}	8.994771×10^{-8}	8.894896×10^{-8}	8.869936×10^{-8}	8.863445×10^{-8}
	$\underline{\tau_0 = 0.375}$				
	Bercovier-Engelmann Regularization				
10^{-1}	1.623909×10^{-3}	1.582885×10^{-3}	1.581855×10^{-3}	1.581779×10^{-3}	1.581769×10^{-3}
10^{-2}	1.085270×10^{-3}	7.053111×10^{-4}	6.960561×10^{-4}	6.952442×10^{-4}	6.952255×10^{-4}
10^{-3}	8.821427×10^{-4}	8.278289×10^{-5}	8.758886×10^{-5}	8.704881×10^{-5}	8.638644×10^{-5}
10^{-4}	8.887202×10^{-4}	8.519315×10^{-6}	8.501405×10^{-6}	8.694866×10^{-6}	8.845921×10^{-6}
10^{-5}	8.893644×10^{-4}	8.569292×10^{-7}	8.509577×10^{-7}	8.570079×10^{-7}	8.649968×10^{-7}
10^{-6}	8.893644×10^{-4}	8.574575×10^{-8}	8.511668×10^{-8}	8.566827×10^{-8}	8.560124×10^{-8}
	Papanastasiou Regularization				
10^{1}	1.598519×10^{-3}	1.553552×10^{-3}	1.552506×10^{-3}	1.552413×10^{-3}	1.552401×10^{-3}
10^{2}	1.138180×10^{-3}	8.094995×10^{-4}	7.961622×10^{-4}	7.961382×10^{-4}	7.961298×10^{-4}
10^{3}	8.799405×10^{-4}	9.477742×10^{-5}	1.009830×10^{-4}	9.963894×10^{-5}	9.836866×10^{-5}
10^{4}	8.887246×10^{-4}	9.998811×10^{-6}	9.857640×10^{-6}	9.893807×10^{-6}	1.004589×10^{-5}
10^{5}	8.893694×10^{-4}	1.007135×10^{-6}	9.912362×10^{-7}	9.901165×10^{-7}	9.913865×10^{-7}
10^{6}	8.893644×10^{-4}	1.007866×10^{-7}	9.918013×10^{-8}	9.906410×10^{-8}	9.910985×10^{-8}

In Table 4.1, we compare the FEM regularized solution of velocity $\boldsymbol{u}$ with the analytical one $\boldsymbol{u}_{ex}$, and display the error with respect to the L^2-norm. The results are presented in two main blocks for two

different values of the yield-stress parameter, which are carefully chosen to have an aligned interface between unyielded and yielded regions with respect to the mesh refinement, $\tau_0 = 0.25$ and $\tau_0 = 0.375$. The simulations are carried out with both, Bercovier-Engelmann and Papanastasiou regularizations, where k denotes the regularization parameter. It is worth mentioning that the configuration is discretized with structured quadrilateral elements, and at each refinement level, each element is subdivided into four sub-elements. Thus, to have aligned interfaces on successive mesh refinement levels is possible only from certain finer levels. Here, for the yield stress parameter τ_0 set equal to 0.25, the alignment of the interfaces is possible from the mesh refinement level 2, and at mesh refinement level 3 for the yield stress parameter τ_0 set equal to 0.375. Thus, the odd behavior of the stagnation of the error at level 2 for the case $\tau_0 = 0.375$ needs to be interpreted with nonaligned interfaces case Table 4.3.

The accuracy of the solutions improves with a very small regularization parameter k for Bercovier-Engelmann regularization, while a very large regularization parameter provides accurate solutions for Papanastasiou regularization. For Bercovier-Engelmann regularization, as we decrease the regularization parameter from the range of values 10^{-1} to 10^{-6}, the corresponding L^2-norm of the error is proportionally decreasing with respect to regularization parameter. In contrast, the L^2-error shows no improvement with respect to mesh refinement, and the accuracy of the solutions is of the regularization order. Similarly, for Papanastasiou regularization, the L^2-error is proportionally decreasing with respect to increasing the regularization parameter from the range of values 10^1 to 10^6, and shows no improvement with respect to mesh refinement. For both choices of yield stress parameter values, both regularizations have similar performance in terms of improving the accuracy of solutions.

Concerning the Newton solver, we list in Table 4.2 the number of nonlinear iterations for successive mesh level refinements with respect to regularization parameter. Furthermore, the linear subproblems inside each nonlinear Newton's sweep are solved with the direct linear solver, UMFPACK.

Table 4.2: **Newton Iterations:** Number of nonlinear iterations with respect to regularization parameter k and refinement level L for Bingham viscoplastic flow for different values of yield stress parameter τ_0.

$k\backslash L$	2	3	4	5	6	2	3	4	5	6
	$\tau_0 = 0.25$					$\tau_0 = 0.375$				
	Bercovier-Engelmann Regularization									
10^{-1}	3	3	4	4	4	3	3	3	3	3
10^{-2}	18	16	15	14	14	12	11	13	13	13
10^{-3}	21	22	19	19	18	15	21	19	19	18
10^{-4}	25	24	24	22	22	18	24	24	22	22
10^{-5}	27	25	25	24	24	11	25	28	26	25
10^{-6}	83	22	29	41	51	6	27	30	43	54
	Papanastasiou regularization									
10^1	3	3	4	3	4	3	3	3	3	3
10^2	15	15	14	12	12	11	11	11	11	11
10^3	16	17	18	16	16	13	17	17	16	19
10^4	22	22	24	24	25	15	23	25	26	26
10^5	28	22	27	29	32	11	25	29	32	35
10^6	34	22	30	50	52	9	25	32	51	53

We used the continuation strategy with respect to the regularization parameter for Newton's starting solutions. That is, as we decrease the amount of regularization introduced in the problem, the corresponding solutions are computed by using solutions with a higher amount of regularization as a start-solutions. The nonlinearity of the viscoplastic problem is increased either by increasing the yield stress parameter, or by decreasing the amount of regularization introduced in the problem. The amount of regularization is proportionally decreased, by decreasing the regularization parameter k for Bercovier-Engelmann regularization or by increasing the regularization parameter k for Papanastasiou regularization. Clearly, this is directly reflected on number of nonlinear iterations displayed in Table 4.2. Despite the complexity of the combination of regularization parameter and mesh refinement, the solver preserves the same nonlinear convergence rate at each refinement level.
In Table 4.3, we display the L^2-error for velocity solution with the exact one for the case of nonaligned interfaces of unyielded and yielded regions with the mesh.

Table 4.3: **L^2-error of velocity $\|\boldsymbol{u} - \boldsymbol{u}_{ex}\|_2$:** Velocity errors in the L^2-norm for Bingham viscoplastic flow for different values of the yield stress parameter.

$k\backslash L$	2	3	4	5	6
	$\tau_0 = 0.253125$				
	Bercovier-Engelmann Regularization				
10^{-1}	2.970230×10^{-3}	2.943989×10^{-3}	2.942496×10^{-3}	2.942447×10^{-3}	2.942446×10^{-3}
10^{-2}	7.017845×10^{-4}	6.968269×10^{-4}	6.828571×10^{-4}	6.818404×10^{-4}	6.818447×10^{-4}
10^{-3}	7.288438×10^{-5}	7.536287×10^{-5}	7.894642×10^{-5}	7.730505×10^{-5}	7.647529×10^{-5}
10^{-4}	7.196318×10^{-6}	7.201308×10^{-6}	7.330351×10^{-6}	8.585453×10^{-6}	8.013995×10^{-6}
10^{-5}	1.214840×10^{-6}	1.177080×10^{-6}	1.118774×10^{-6}	1.905528×10^{-6}	1.596786×10^{-6}
10^{-6}	1.235439×10^{-6}	1.078582×10^{-6}	9.709680×10^{-7}	1.446487×10^{-6}	1.223437×10^{-6}
	Papanastasiou Regularization				
10^{1}	2.994777×10^{-3}	2.974349×10^{-3}	2.972587×10^{-3}	2.972478×10^{-3}	2.972516×10^{-3}
10^{2}	8.203538×10^{-4}	7.958385×10^{-4}	7.801462×10^{-4}	7.797193×10^{-4}	7.797139×10^{-4}
10^{3}	8.640441×10^{-5}	8.797258×10^{-5}	9.262107×10^{-5}	9.013183×10^{-5}	8.892082×10^{-5}
10^{4}	8.723038×10^{-6}	8.628136×10^{-6}	8.633317×10^{-6}	9.796810×10^{-6}	9.306870×10^{-6}
10^{5}	1.260804×10^{-6}	1.244867×10^{-6}	1.214936×10^{-6}	1.932024×10^{-6}	1.659530×10^{-6}
10^{6}	1.230502×10^{-6}	1.076311×10^{-6}	9.707930×10^{-7}	1.444387×10^{-6}	1.333276×10^{-6}
	$\tau_0 = 0.3333333$				
	Bercovier-Engelmann Regularization				
10^{-1}	2.289944×10^{-3}	2.251774×10^{-3}	2.251031×10^{-3}	2.250828×10^{-3}	2.250848×10^{-3}
10^{-2}	1.186941×10^{-3}	7.169343×10^{-4}	7.183205×10^{-4}	7.173794×10^{-4}	7.174272×10^{-4}
10^{-3}	9.088943×10^{-4}	1.212913×10^{-4}	9.535640×10^{-5}	8.306562×10^{-5}	8.328602×10^{-5}
10^{-4}	8.992746×10^{-4}	8.895081×10^{-5}	3.782218×10^{-5}	8.606960×10^{-6}	8.722071×10^{-6}
10^{-5}	8.988972×10^{-4}	8.916449×10^{-5}	3.580582×10^{-5}	3.887651×10^{-6}	1.875271×10^{-6}
10^{-6}	8.988921×10^{-4}	8.924030×10^{-5}	3.555589×10^{-5}	3.669765×10^{-6}	3.223283×10^{-6}
	Papanastasiou Regularization				
10^{1}	2.250569×10^{-3}	2.210720×10^{-3}	2.209799×10^{-3}	2.209523×10^{-3}	2.209524×10^{-3}
10^{2}	1.247860×10^{-3}	8.229736×10^{-4}	8.232711×10^{-4}	8.224887×10^{-4}	8.225101×10^{-4}
10^{3}	9.091701×10^{-4}	1.268233×10^{-4}	1.075757×10^{-4}	9.523797×10^{-5}	9.547306×10^{-5}
10^{4}	8.994667×10^{-4}	8.897055×10^{-5}	3.838476×10^{-5}	9.941859×10^{-6}	9.968182×10^{-6}
10^{5}	8.988920×10^{-4}	8.915357×10^{-5}	3.584173×10^{-5}	3.941740×10^{-6}	1.947580×10^{-6}
10^{6}	8.988920×10^{-4}	8.923839×10^{-5}	3.555196×10^{-5}	3.667045×10^{-6}	3.333523×10^{-6}

To complete the exposure with circumstances that occur for interfaces in general flow simulations, in addition to the exposed results for the yield stress parameters leading to aligned interfaces in Table 4.1, we provided results for simulations with a yield stress parameter for nonaligned interfaces in Table 4.3.

Table 4.3 displays the velocity L^2-error with the exact solution for the nonaligned interface case. We shift the interface a little bit to cross the element with a small perturbation of the yield stress parameter values of the previous simulation. We made this choice to not introduce any error related to mesh disturbance. The simulations are carried out for two yield stress value parameter τ_0 set equal to 0.253125, and 0.3333333 with both regularizations, Bercovier-Engelmann and Papanastasiou regularizations, and the results are displayed block wise. Each block presents the velocity L^2-error with respect to mesh refinement and regularization parameter.

Once again, with respect to mesh refinement, the L^2-error shows no clear reduction. Moreover, the error is only decreasing up to a certain stagnating value with respect to the decrease in amount of regularization. For Bercovier-Engelmann regularization, the parameter k is decreased in the range of 10^{-1} to 10^{-6}, and error shows a stagnating behavior when k takes values less than or equal to 10^{-4}. For Papanastasiou regularization, the parameter k is increased in the range of 10^1 to 10^6, and error shows a stagnating behavior when k takes values greater than or equal to 10^4. For both choices of yield stress parameter values, the regularizations have the same behavior towards L^2-error.

A comparative analysis of the errors of aligned and nonaligned cases in Table 4.1 and Table 4.3 shows that, for the former case, the error keeps decreasing with respect to decreasing the amount of regularization, while for the latter, it stops decreasing and stagnates at a certain limit with respect to the decreases in the amount of regularization. Thus, the L^2-error is not only regularization parameter dependent, but also prone to the interface's alignment with the mesh. For both cases, the error reaches an acceptable limit, and the regularized FEM viscoplastic solutions are admissible for aligned and nonaligned interfaces.

We list the nonlinear iteration for the Newton solver for the nonaligned case in Table 4.4.

Table 4.4: **Newton Iterations:** Number of nonlinear iterations with respect to regularization parameter k and refinement level L for Bingham viscoplastic flow for different values of yield stress parameter τ_0.

$k\backslash L$	2	3	4	5	6	2	3	4	5	6
	$\tau_0 = 0.253125$					$\tau_0 = 0.333333$				
	Bercovier-Engelmann Regularization									
10^{-1}	3	3	4	4	4	3	3	3	4	4
10^{-2}	16	16	14	14	15	15	15	15	14	14
10^{-3}	20	21	20	18	18	19	18	20	19	18
10^{-4}	25	23	23	22	22	16	18	23	22	22
10^{-5}	31	24	25	24	24	9	19	23	23	25
10^{-6}	33	25	29	41	51	7	27	27	49	57
	Papanastasiou regularization									
10^1	4	4	3	3	4	3	3	3	3	3
10^2	15	13	14	11	12	12	13	11	11	11
10^3	18	17	18	16	16	16	17	17	16	16
10^4	21	24	25	25	25	18	18	24	25	25
10^5	40	25	25	33	31	10	19	25	25	35
10^6	47	25	31	39	53	44	24	28	46	59

The results are presented in a block wise manner, where the blocks correspond to the yield stress parameter τ_0 set equal to 0.253125 and 0.333333, for both regularizations. For each block, we list the nonlinear sweeps for successive mesh refinement levels and regularization parameter. The Newton's starting solutions follow the continuation strategy with respect to regularization parameter. And the linear systems at each nonlinear iteration are solved using a direct solver.

The nonlinear solver for the nonaligned interface case, Table 4.4, shows similar behavior as for the aligned interface case, Table 4.2. The nonlinearity of the problem, remains unchangeable with respect to mesh refinement, while it is increased either by increasing the yield stress parameter, or by decreasing the amount of regularization introduced in the problem.

We proceed with the highlight of the similar performance for both regularizations, Bercovier-Engelmann regularization and Papanastasiou regularization, and provide the velocity at the vertical centerline with respect to regularization parameters for both regularizations.

In Figure 4.4, we display the velocity solutions at vertical centerlines for both Bercovier-Engelmann regularization and Papanastasiou regularization, with respect to the amount of regularization.

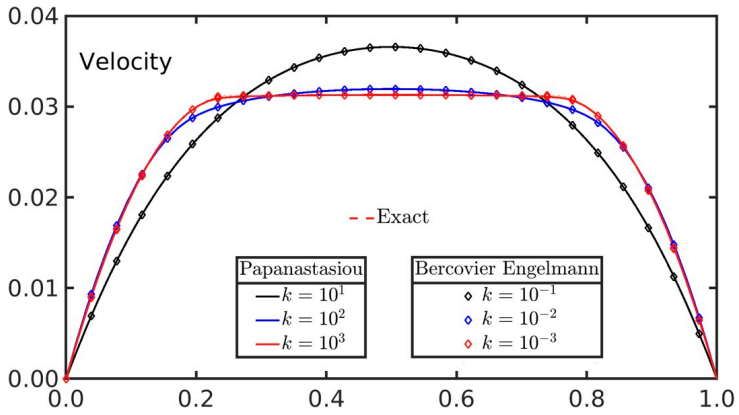

Fig. 4.4: **Viscoplastic channel flow:** Impact of regularization parameter on velocity solution profiles for yield stress parameter $\tau_0 = 0.25$, where $\mu_0 = 1.0$ and grid refinement size $h = 0.03125$. The velocity profile corresponds to optimal k is plotted together with Bingham analytical velocity in Eq. (4.1).

Along the investigations of viscoplastic channel flow, both Bercovier-Engelmann regularization and Papanastasiou regularization show similar behavior, either with regard to nonlinear solver or the accuracy aspect. Clearly, there is no fond preference, and we content to use Papanastasiou regularization in what follows.

In regard to the study of aligned and nonaligned interfaces, the accuracy of the solutions is prone to regularization and the alignment of interfaces with the mesh. For both cases, accepted solutions with respect to accuracy are possible with a moderately smaller amount of regularization introduced to the problem.

In Figure 4.5, we display the velocity at the vertical centerline for two yield stress values, which correspond to aligned and nonaligned interfaces.

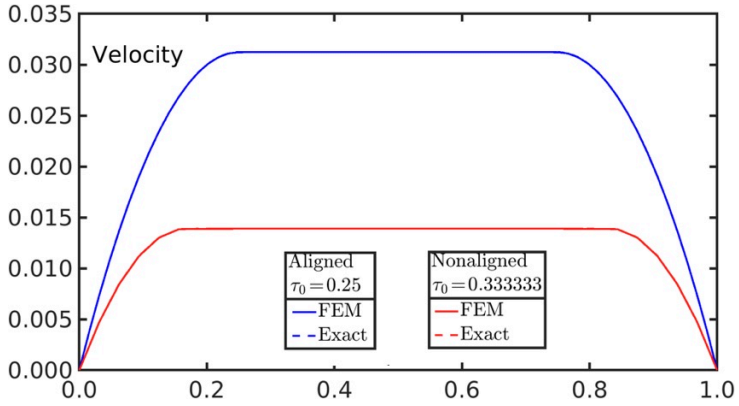

Fig. 4.5: **Viscoplastic channel flow:** Impact of regularization parameter on velocity solution profiles for yield stress parameter $\tau_0 = 0.25$, where $\mu_0 = 1.0$ and grid refinement size $h = 0.03125$. The velocity profile that corresponds to optimal k is plotted together with Bingham's analytical velocity in Eq. (4.1).

Clearly, Figure 4.5 depicts that for both cases, aligned interfaces with mesh case and nonaligned interfaces with mesh case, the exact solution can be obtained with a regularized FEM viscoplastic model.

We proceed with our investigations with Papanastasiou regularization for the rest of this work. Next subsection is devoted to thixoviscoplastic channel flow.

4.2.2 Houška Thixoviscoplastic Channel Flow

This subsection is concerned with thixoviscoplastic channel flow. The microstructure equation raises additional challenges to the ones related to the viscoplastic subproblem, which need to be addressed. That is, the regularization of the breakdown function (nonsmoothness with respect to shear rate), and the boundary conditions for the microstructure equation. We upgrade the quasi-Newtonian viscoplastic channel flow benchmark to incorporate the microstructure equation's challenges and provide validation tools for the numerical solutions. We tackle the extended challenges of thixoviscoplastic channel flow with the accepted convergence of quasi-Newtonian viscoplastic solutions to exact Bingham solution with respect to regularization in section §4.2.1. So, we advantageously use the unidirectional flow assumption to overcome the lack of an analytic exact solution for thixoviscoplastic channel flow. As the flow is exclusively in the x-axis direction, we implement the reduced one-dimensional thixoviscoplastic model, and use the solutions as boundary conditions, as well as validation tools for solutions of FEM thixoviscoplastic channel flow (for additional implementation information, we refer to [81]).

For our problem, we set the material parameter values as follows: the nonthixotropic and thixotropic plastic viscosities η_0, and η_∞, respectively, with a value unity. We form the unyielded region with the same contributions of nonthixotropic yield stress τ_0 and thixotropic yield stress τ_∞ parameters, with a value set equal to 0.25. The ratio of breakdown and buildup parameters in the microstructure equation is set to unity, where both breakdown parameter $\mathcal{M}_b$, and buildup parameter $\mathcal{M}_a$ are set to take 0.01 value.

We plot in Figure 4.6, the one-dimensional reduced thixoviscoplastic flow velocity solution against the two-dimensional FEM thixoviscoplastic developed velocity solution.

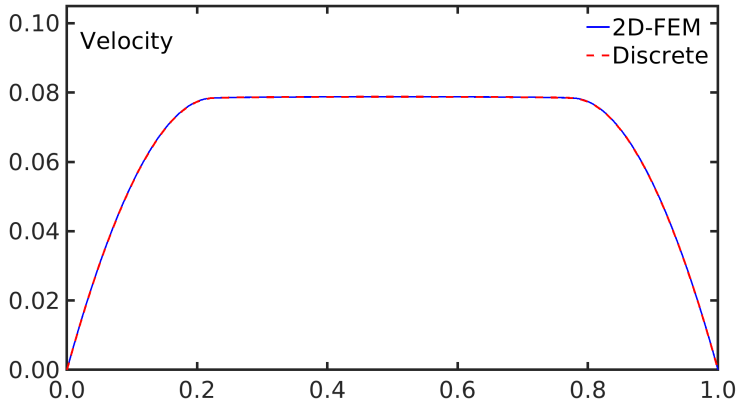

Fig. 4.6: **Thixoviscoplastic channel flow:** Comparison of velocity solutions of 1D and fully developed 2D models for thixoviscoplastic flows in a unit channel.

Figure 4.6 shows that the velocity solution of the two-dimensional FEM thixoviscoplastic developed channel flow matches with the velocity solution of the reduced one-dimensional thixoviscoplastic problem.

Similarly, for microstructure solutions, Figure 4.7 depicts the matchable superposition of two microstructure solutions.

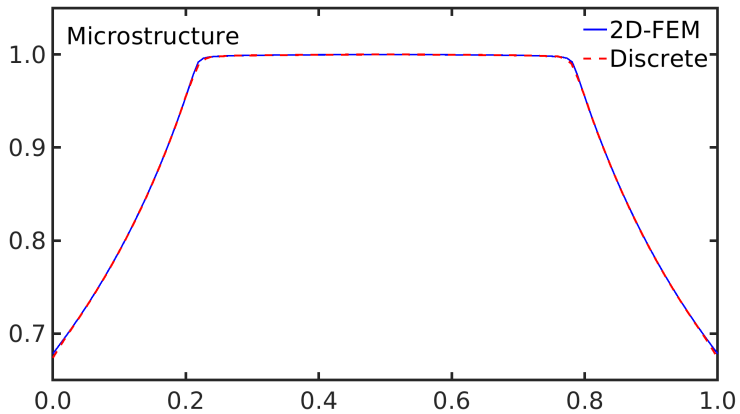

Fig. 4.7: **Thixoviscoplastic channel flow:** Comparison of microstructure solutions of 1D and fully developed 2D models for thixoviscoplastic flows in a unit channel.

The usefulness of reduced one-dimensional thixoviscoplastic solutions lies in the validation of FEM thixoviscoplastic flow solutions, as well as to provide the necessary or alternative boundary conditions. Firstly, with respect to the momentum equation, as the flow reaches the developed state, both solutions should coincide. Or, if it is imposed as Dirichlet boundary conditions at the inflow boundary section Γ^-, it

should remain unchanged along the channel. Furthermore, we use it as Dirichlet boundary conditions at outflow boundary section Γ^+ to overcome the need to use 'do-nothing' or any modified version of it. Secondly, with respect to the microstructure equation, beside from its validation aspect, it provides the necessary inflow boundary conditions at the inflow boundary section Γ^-.

In Figure 4.8, we present the velocity and the microstructure solutions of two-dimensional FEM thixotropic channel flow with Dirichlet boundary conditions at both, inflow boundary section Γ^-, and the outflow boundary section Γ^+.

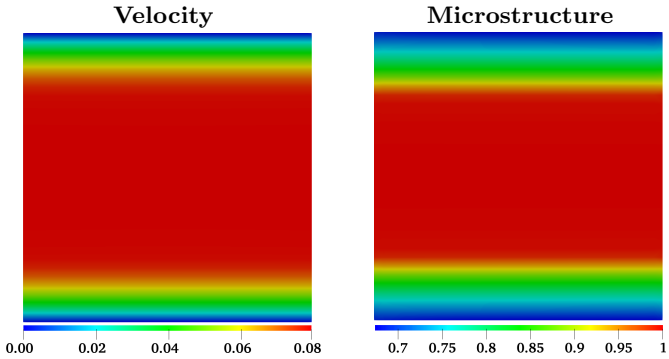

Fig. 4.8: **Thixoviscoplastic channel flow:** The FEM Houška thixoviscoplastic flow solutions, velocity magnitude (LEFT) and microstructure (RIGHT), with solutions of the one-dimensional reduced Houška thixoviscoplastic problem as Dirichlet boundary conditions at inflow and outflow boundary sections.

Figure 4.8 shows a thixovicoplastic channel flow solution, which fulfills the x-axis unidirectional flow assumptions along the channel (including the outflow boundary sections).

With the reduced one-dimensional thixoviscoplastic model mechanism as a validation tool for the two-dimensional FEM numerical solutions, we proceed with the analysis of regularization impact on the accuracy of the quasi-Newtonian modeling approach for thixoviscoplastic channel flow. We select a set of increased regularization parameter values in a wide range to allow for a clear change in the profile.

In Figure 4.9, we plot the velocity profiles of fully developed two-dimensional FEM regularized thixoviscoplastic channel flow with respect to regularization parameter values.

Figure 4.9 depicts that, for smaller regularization parameter value, the velocity flow profile shows a perfect parabolic profile, which is connected to a Newtonian-like flow profile, expressing that the flow is driven by almost constant viscosity dominated by the regularization parameter value. As we increase the regularization parameter values, the peak of the parabolic profile smoothly gets flattened in the unyielded region, to fully flattened shape for the unyielded region and converges to the final profile for a larger regularization parameter value. This is so far the same observation for the viscoplastic channel flow benchmark.

With the consistency "convergence" of velocity solutions of quasi-Newtonian modeling of thixoviscoplastic channel flow and viscoplastic channel flow benchmark with respect to the regularization parameter, we proceed with our investigations for the microstructure equation.
Firstly, we analyze the impact of regularization on the indicator prospects of microstructure for the regions. Indeed, the admissible range for the microstructure field lies in the close interval $[0, 1]$, for the

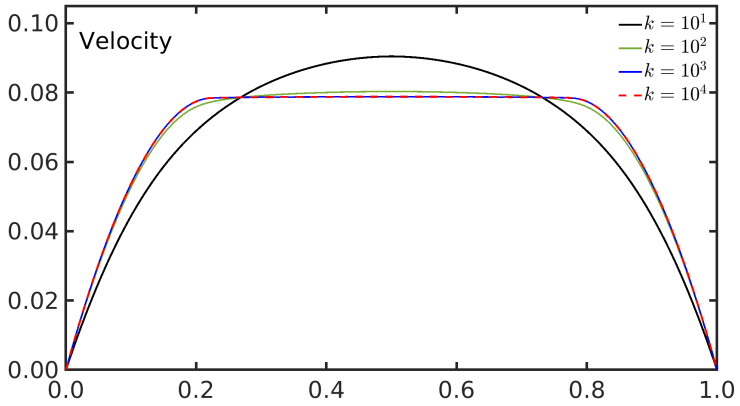

Fig. 4.9: **Thixoviscoplastic channel flow:** Impact of regularization parameter on velocity magnitude u for regularized Houska's model , where $\tau_0 = \tau_\infty = 0.125$, $\eta_0 = 1.0$, and $\eta_\infty = 0.0$, $\mathcal{M}_a = 0.01$, and $\mathcal{M}_b = 0.01$.

unyielded region, the microstructure takes values approaching unity, otherwise, it indicates the yielded region. Thus, we analyze the "domain" of microstructure with respect to its admissible range for regularization parameter.
Secondly, we investigate the processes of buildup and breakdown within the microstructure equation. We study the boundary limit with respect to variations in rate of buildup parameter or breakdown parameters.

For the same set of regularized parameter values, we plot the microstructure solution profile of the developed thixoviscoplastic channel flow in Figure 4.10. Figure 4.10 shows that, for a smaller regularized

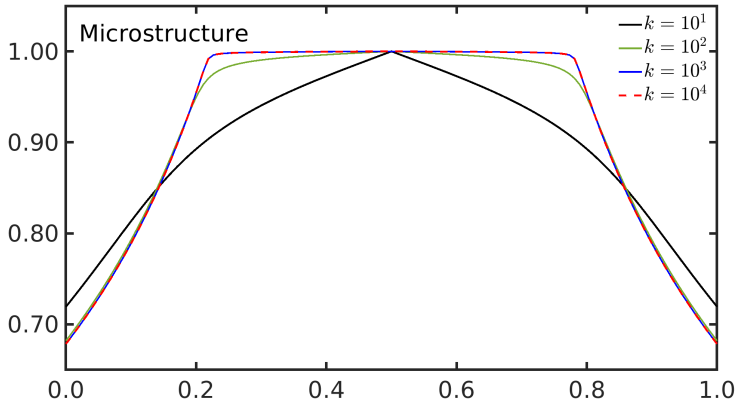

Fig. 4.10: **Thixoviscoplastic channel flow:** Impact of regularization parameter on microstructure λ for regularized Houška's thixoviscoplastic model where $\tau_0 = \tau_\infty = 0.125$, $\eta_0 = 1.0$, and $\eta_\infty = 0.0$, $\mathcal{M}_a = 0.01$, and $\mathcal{M}_b = 0.01$.

parameter value, the microstructure domain indicates the unyielded region is reduced to the centerline of the channel, and sigmoidally changes with the increase of the regularization parameter. The unyielded region indicated by microstructure matches perfectly with the unyielded region indicated by velocity.

The unidirectional x-axis flow assumptions are satisfied along the channel, and irrespective of the regularization parameter, as depicted in Figure 4.11.

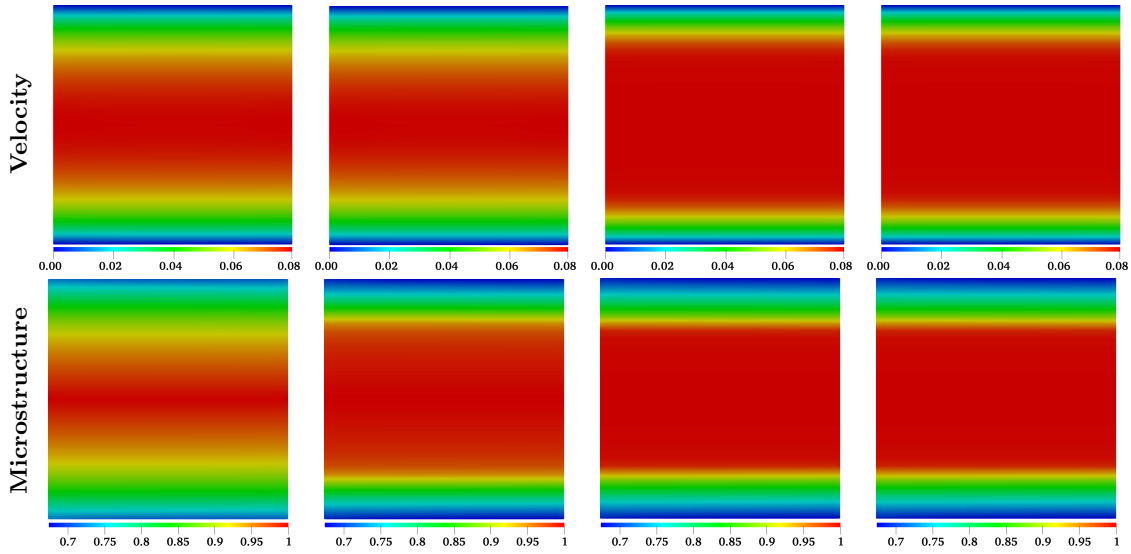

Fig. 4.11: **Thixoviscoplastic channel flow:** Velocity magnitude (TOP) and microstructure (BOTTOM) for increased regularization parameter values $k = 10^1, 10^2, 10^3, 10^4$ (LEFT-to-RIGHT), where $\tau_0 = \tau_\infty = 0.125$, $\eta_0 = 1.0$, and $\eta_\infty = 0.0$, $\mathcal{M}_a = 0.01$, and $\mathcal{M}_b = 0.01$.

We proceed with the analysis of the competition process of buildup and breakdown incorporated in the microstructure equation. Since the ratio of the breakdown $\mathcal{M}_b$ and buildup parameter $\mathcal{M}_a$ is important in this process, we content to vary only the breakdown parameter $\mathcal{M}_b$, and keep the buildup parameter $\mathcal{M}_a$ fixed. In Figure 4.12, we plot the microstructure solution profiles for different values of the breakdown parameter.

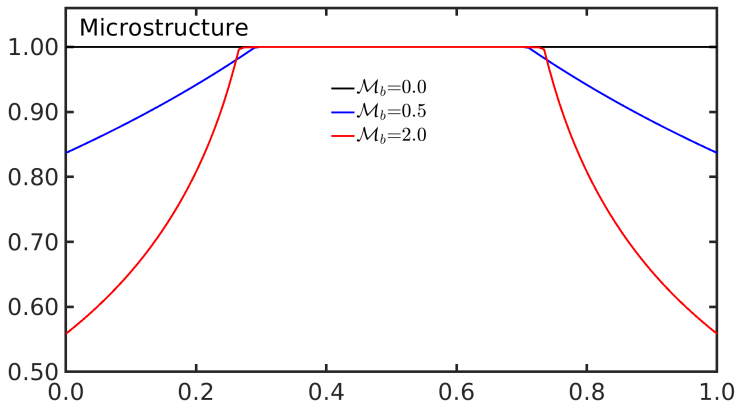

Fig. 4.12: **Thixoviscoplastic channel flow:** Impact of breakdown parameter $\mathcal{M}_b$ on microstructure solutions, where $\tau_0 = 0.0, \tau_\infty = 0.25$, $\eta_\infty = 0.0$, $\eta_0 = 1.0$, and $k = 10^4$.

It is depicted in Figure 4.12 that, at vanishing breakdown parameter, the process of breakdown take over the full channel. For the nonvanishing breakdown parameter, the striking remark is on the transition between the regions. As the breakdown parameter increases, the transitions between regions get sharpened, which is clearly seen in the increase of the jump of the gradient of microstructure at interfaces.

In this section, we investigated thixoviscoplastic channel flow to incorporate the microstructure challenges within the viscoplastic channel flow benchmark.

Firstly, we analyzed the regularization impact within the quasi-Newtonian modeling approach for viscoplastic channel flow. Owing an exact solution, viscoplastic channel flow benchmark is meant for providing optimal parameter settings with respect to the modeling of the thixoviscoplastic flow problem. We started by showing that the regularized FEM solution perfectly follows the changes in the yield stress parameter. For a vanishing yield stress parameter, the flow is Newtonian-like and showed the perfect parabolic profile. And as we increased the yield stress parameter, the peak of the parabolic profile got flattened respectively in the unyielded region. We used the exact Bingham solution as boundary conditions for the FEM regularized viscoplastic problem in conjunction with a homogeneous source term as a standard way in FEM simulations. This leads to a discontinuous pressure solution between regions, which increased the benchmark challenges with respect to pressure approximations. Beside that, big jumps at the intersections of boundary sections Γ^- and Γ^+ with the interfaces. We also provided a solution avoiding the discontinuity of the pressure along the interfaces using pressure drop boundary conditions. For the quantitative analysis with respect to regularization (Bercovier-Engelmann and Papanastasiou regularizations), we proceeded with the former one to provide error with respect to the analytic exact solution. We carried out simulations for yield stress parameter values yielding aligned interfaces (one element belongs either to an unyielded region or a yielded region) as well as nonaligned interfaces (unyielded and yielded regions coexist in the same element). For both cases, we showed a continuation of an increase in accuracy for the aligned interfaces and up to a certain acceptable limit for the nonaligned ones, with decreasing the amount of regularization introduced in the problem. Both, Bercovier-Engelmann and Papanastasiou regularizations, showed one-to-one similitude along the investigations, either with respect to accuracy or for the nonlinear solver behavior. In regard to accuracy, the solutions showed a clear improvement in accuracy with very a small amount of regularization. And with respect to nonlinear solver behavior (for both regularizations), the Newton showed mesh refinement independency, while the nonlinear iterations are increased either by the increase of the yield stress parameter values, or by the decrease of the amount of regularization introduced in the problem.

Secondly, we used the unidirectional flow assumptions to overcome the lack of an analytic solution for thixoviscoplastic channel flow. We implemented the reduced one-dimensional thixoviscoplastic model, and used the solutions as boundary conditions, as well as validation tools for solutions of FEM thixoviscoplastic channel flow. On the one hand, the fully developed FEM thixoviscoplastic flow solutions and the reduced one-dimensional thixoviscoplastic solutions match. On the other hand, we used reduced one-dimensional thixoviscoplastic solutions as Dirichlet boundary conditions at outflow boundary section Γ^+ instead of 'do-nothing' boundary conditions, and as inflow boundary conditions for microstructure. Then, we analyzed the impact of regularization on the indicator prospect of microstructure for the regions, and the competition process of buildup and breakdown incorporated in the microstructure equation by monitoring the ratio of the breakdown parameter $\mathcal{M}_b$ and buildup parameter $\mathcal{M}_a$. It is conceived that the unyielded region indicated by microstructure matches perfectly with the unyielded region indicated by velocity. Furthermore, the transitions between unyielded and yielded regions got sharpened for larger breakdown parameter values. We proceed with another well established academic benchmark in the next section, which is the lid-driven cavity flow benchmark.

4.3 Thixoviscoplastic Lid-driven Cavity Flow

This section is devoted to thixoviscoplastic (TVP) lid-driven cavity flow, as an important benchmark for computational fluid dynamics codes in academia. Lid-driven cavity is accepted as a test configuration to check point-wise mesh convergences despite the lack of regularity due to the pressure singularity in the corners of upper-lid. The schematic of the classical lid-driven cavity configuration is presented in Figure 4.13. We present the corresponding results for Newtonian, viscoplastic, and thixoviscoplastic lid-driven flows [7].

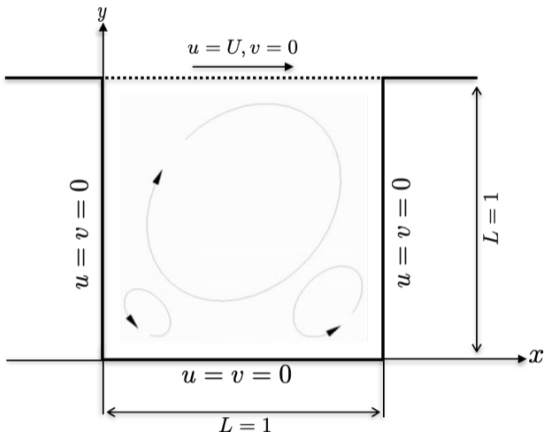

Fig. 4.13: **Schematic representation of lid-driven cavity.**

Firstly, we start with the Newtonian lid-driven cavity flow benchmark. It introduces nonuniform recirculating flows with well-studied vortices with respect to Reynolds number. Beside being the benchmark for global quantities, for instance kinetic energy and enstophy, it also provides a point-wise benchmark, namely the location of vortices and x-axis cutline solutions. We investigate the global quantity benchmark using the kinetic energy, and the point-wise benchmark with the help of the velocity magnitude at the vertical centerline and the locations of the primary and the lower left secondary vortices for the particular Reynolds numbers set to 1000, 5000, and 10 000, respectively. We also present the corresponding Newton-multigrid solver behavior.

Secondly, we analyze the viscoplastic lid-driven cavity flow benchmark. The quasi-Newtonian modeling approach for yield stress materials introduces a regularization parameter to get a well-defined extended viscosity function in the whole computational domain. We investigate the accurate growth and location of unyielded regions with respect to the optimal settings of regularization and mesh refinement, for increased values of the yield stress parameter. Moreover, we analyze the corresponding Newton-multigrid solver convergence with respect to all parameters, namely the yield stress parameter, and the regularization parameter on successive mesh refinement levels. Meanwhile, we check the optimal strategy for fast convergence for the nonlinear solver.

Lastly, we present thixoviscoplastic lid-driven cavity flow. Thixoviscoplastic flow equations are an upgrade of generalized viscoplastic Navier-Stokes equations in two aspects. On the one hand, the extended viscosity function integrates the microstructure via thixotopic plastic viscosity and thixotropic yield stress. On the other hand, the set of equations is supplemented with a microstructure evolution equation. This equation

reflects the competition process of Aging and Rejuvenation, which occurs via the interaction of buildup and breakdown functions dependent on two additional model parameters, namely buildup and breakdown parameters. Here, we also investigate the accurate growth and location of unyielded regions with respect to the optimal settings of regularization and mesh refinement, for increased values of the thixotropic yield stress parameter. We analyze the corresponding Newton-multigrid solver convergence with respect to the thixotropic yield stress parameter, and regularization parameter on successive mesh refinement levels. Moreover, we investigate the role played by the microstructure equation throughout the analysis of the types of transitions between yielded and unyielded regions.

We consider the classical lid-driven cavity settings on unity square for our study of Newtonian, viscoplastic, and thixoviscoplastic flows. In what follows, the flow is generated with the moving upper lid with x-velocity set to unity, which comes into contact with the stationary walls. That is, the flow problem is subject to nonhomogeneous Dirichlet boundary conditions for x-velocity at the upper boundary wall, and homogeneous Dirichlet boundary conditions at the other walls. Next subsection is devoted to Newtonian lid-driven cavity flow.

4.3.1 Newtonian Lid-driven Cavity Flow

In this subsection, we present Newtonian lid-driven cavity flow. It is used in the context of this work to provide a foundation for validation, mainly point-wise, for our numerical method and simulation algorithm. Indeed, Newtonian lid-driven cavity flow is not only the benchmark for global quantities, it also provides point-wise benchmark quantities, for instance, cutline solutions, and the location of vortices. Moreover, the Newtonian flow is free from regularization effects, which occur with our choice of a quasi-Newtonian modeling approach for viscoplastic and thixoviscoplastic flows. Thus, it provides a reference base for a mesh refinement for FEM solutions point-wisely, mainly in this work, the accurate track of the interface between yielded and unyielded zones with respect to mesh refinement.

We use the classical lid-driven cavity configuration presented in Figure 4.13, with the upper lid moving with speed U set to unity. For a particular set of Reynolds numbers, Re set equal to 1000, 5000, and 10 000, we validate our FEM code on two folds, namely accuracy and efficiency. Firstly, with respect to accuracy, we provide the global quantity benchmark of kinetic energy, and the point-wise quantities benchmark of velocity magnitude at vertical centerline beside the location of the primary and the lower left secondary vortices. Secondly, with respect to efficiency, we study the Newton-multigrid solver in terms of the quotient of the number of nonlinear sweeps and the average number of linear multigrid sweeps with respect to mesh refinement levels.

In Table 4.5, we list the kinetic energy, half of the power two of the L_2-norm of the approximated velocity, and Newton-multigrid iterations,in terms of the quotient (N/M) of the number of nonlinear sweeps and the average number of linear multgrid sweeps, with respect to mesh refinement.
For the starting solutions in Table 4.5, we use the continuation strategy, which constitutes of the interpolated solutions on the one-level coarser. The kinetic energy results displayed in table 4.5 show a clear mesh convergence, and are in agreement with the different FEM discretizations from literature [30, 78]. Moreover, the Newton-multigrid solver shows a mesh refinement independent behavior. The quotient N/M is almost constant independently with respect to mesh refinement, without confusion, the additional nonlinear iterations at the coarser levels are simply due to the higher interpolation error for the starting solutions at coarser levels.

We proceed with the progressive increases in Reynolds number and present a relative comparison of kinetic energy, and Newton-multigrid solver results in Table 4.6.

Table 4.5: **Newtonian lid-driven cavity flow**: Comparison of energy norm results with references [30] and [78] for Reynolds number R$e = 1000$.

R$e = 1000$		$Kinetic\,Energy = 1/2\left(\int_\Omega \|\boldsymbol{u}_h\|^2\,dx\right)$			
Level	cells	Present	N/M	Ref. [30]	Ref. [78]
5	1024	4.541506×10^{-2}	5/1	4.5418×10^{-2}	4.8095×10^{-2}
6	4096	4.458877×10^{-2}	5/1	4.4590×10^{-2}	4.5828×10^{-2}
7	16384	4.452357×10^{-2}	3/1	4.4524×10^{-2}	4.4843×10^{-2}
8	65536	4.451904×10^{-2}	3/1	4.4519×10^{-2}	4.4592×10^{-2}
9	262144	4.451846×10^{-2}	3/1	4.4518×10^{-2}	4.4535×10^{-2}

The numerical solution corresponding to Reynolds number Re set equal to 1000, and 5000, is obtained without stabilization. While for the simulation case of Reynolds number Re set equal to 10 000, the numerical solution necessitates the use of stabilization, the solution is obtained with the help of edge-oriented stabilization method.

Table 4.6: **Newtonian lid-driven cavity flow**: The kinetic energy and the number of Newton-multigrid iterations, nonlinear number of iterations and the average number of multigrid iterations (N/M), for different mesh refinement levels for Reynolds numbers R$e = 1000$, R$e = 5000$, and R$e = 10\,000$.

Re		1000		5000		10 000	
Level	cells	Energy	N/M	Energy	N/M	Energy	N/M
4	256	5.245101×10^{-2}	6/1	0.106888×10^{-2}	7/1	0.208089×10^{-2}	8/1
5	1024	4.541506×10^{-2}	5/1	6.082524×10^{-2}	6/1	7.940472×10^{-2}	7/1
6	4096	4.458877×10^{-2}	5/1	4.955858×10^{-2}	5/1	5.369527×10^{-2}	6/1
7	16384	4.452357×10^{-2}	3/1	4.768669×10^{-2}	4/1	4.868399×10^{-2}	5/1
8	65536	4.451904×10^{-2}	3/1	4.744815×10^{-2}	3/2	4.783917×10^{-2}	4/2
9	262144	4.451846×10^{-2}	3/1	4.742921×10^{-2}	3/1	4.773500×10^{-2}	3/2
10	1048576	4.451834×10^{-2}	2/1	4.742815×10^{-2}	3/1	4.772692×10^{-2}	3/1
$Ref.\,values \approx$		4.45×10^{-2}		4.74×10^{-2}		4.77×10^{-2}	

Table 4.6 displays ostentatiously the mesh convergence of the kinetic energy in clear accordance with the amount of convection. It is progressively higher with respect to the successive decreases in Reynolds numbers. Moreover, for Reynolds number Re set equal to 10 000, the mesh convergence of the kinetic energy is a simple confirmation result of the consistency of edge-oriented stabilization. In regard to the Newton-multigrid solver, taking in consideration on the one hand the higher interpolation error for the starting solutions at the coarser levels, and the flexibility of the linear solver to match optimally the requirements of the optimal accuracy of the nonlinear solver in the combined adaptive nonlinear-linear solver on the other hand, the average ratio reflects the mesh and Reynolds number independent solver behavior.

The efficiency and robustness of the solver to provide accurate, and mesh independent solutions for global quantity for problems with different complexity, nonlinear convection and nonstandard edge-oriented stabilization stencils, do not overwhelm us to not go forward with the solution's point-wise mesh convergence investigation. The solution's point-wise mesh convergence study is to raise the awareness when dealing with visualization benchmark quantities and provide a base mesh requirement on well-documented classical Newtonian problems.

Next, we proceed to track the locations of the generated vortices for the different Reynolds numbers.

The interest in Newtonian flows exceeds the solver's examinations; the solver has to deal with different complexity, to provide well documented visual benchmark quantities studies, as for instance the locations of the generated vortices with respect to a particular Reynolds number.

In Figure 4.14, we display the formation of vortices for Newtonian flow with respect to the particular Reynolds numbers $Re = 1000$, $Re = 5\,000$, and $Re = 10\,000$ a graded cavity. Also, we provide the corresponding streamline functions.

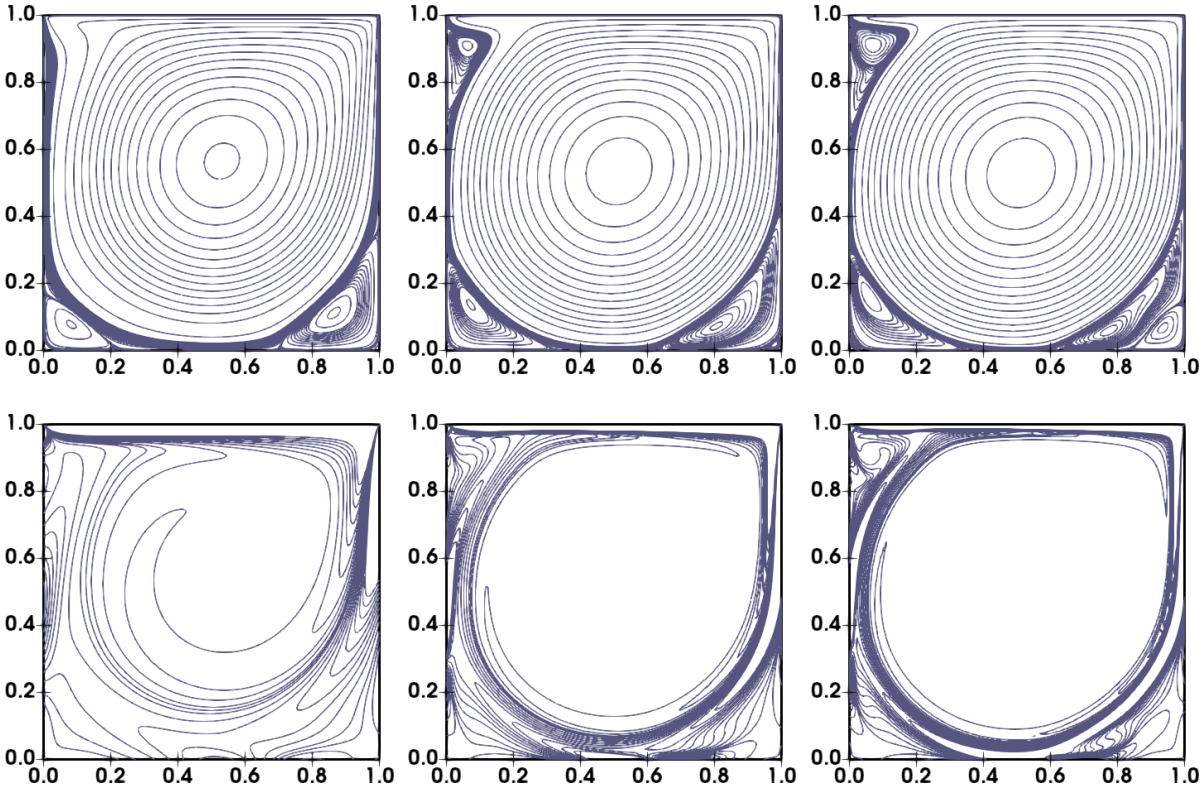

Fig. 4.14: **Newtonian lid-driven cavity flow:** The stream-function's contours (TOP) and vorticity (BOTTOM) computed for Reynolds numbers Re = 1000, Re = 5000, and Re = 10 000 respectively (LEFT-to-RIGHT), at mesh refinement level 9.

At a relatively lower Reynolds number, Re set equal to 1000, three vortices are generated. The main vortex is in the middle of the cavity, the bottom left corner vortices are near the bottom left corner of the cavity, and the bottom right vortex is near the bottom right corner of the cavity. As the Reynolds number increases, for Reynolds number Re set equal to 5000, a fourth top left vortex is generated, and for Reynolds number Re set equal to 10 000 a fifth secondary bottom right vortex is generated near the bottom right corner, increasing the bottom's left vortices to a primary bottom right and secondary bottom right vortices. Furthermore, the common vortices for all Reynolds numbers, that is, the main, the bottom's left and the primary bottom's right vortices, change in shapes and locations with respect to the particular Reynolds number.

We restrict our vortices's location track to the common ones for all Reynolds numbers, Re set equal to 1000, 5000, and 10 000, that is, the main and bottom's left vortices.

In Table 4.7, we list ψ_{max} and ψ_{min} of the main and bottom's left vortices, with respect to mesh refinement for Reynolds numbers Re set equal to 1000, 5000, and 10 000.

Table 4.7: **Newtonian lid-driven cavity flow**: The primary vortex and the lower left secondary vortex for Reynolds numbers Re = 1000, Re = 5000, and Re = 10 000, with respect to mesh refinements.

Re	1000		5 000		10 000	
level	ψ_{max}	ψ_{min}	ψ_{max}	ψ_{min}	ψ_{max}	ψ_{min}
6	0.1190073	-1.72813×10^{-3}	0.1249471	-3.145666×10^{-3}	0.1586626	-5.753575×10^{-3}
7	0.1189360	-1.72649×10^{-3}	0.1225439	-3.077555×10^{-3}	0.1236127	-3.207018×10^{-3}
8	0.1189361	-1.72851×10^{-3}	0.1222499	-3.072411×10^{-3}	0.1225210	-3.183135×10^{-3}
9	0.1189362	-1.72963×10^{-3}	0.1222269	-3.073524×10^{-3}	0.1224097	-3.191010×10^{-3}
10	0.1189366	-1.72965×10^{-3}	0.1222259	-3.073589×10^{-3}	0.1223892	-3.179739×10^{-3}
ref.	0.1189 [25]	-1.729×10^{-3} [25]	0.1221 [49]	-3.070×10^{-3} [25]		

Table 4.7 shows quantitatively the point-wise mesh convergence, once again, in accordance with progressive induces of convection with respect to the increases of Reynolds numbers.

The convergence of the point-wise quantity Table 4.7 is on the same path as the convergence of the global quantity in Table 4.6 with respect to Reynolds numbers. Consequently, the least mesh refinement for a visually accurate solution is designated quantitatively for moderately complex shapes. We go forward with a additional check and use, this time, the visual cutline of velocity solution magnitude at the vertical centerline for different mesh refinements.

We plot, in Figure 4.15, the visual cutline of the velocity magnitude solutions with the successive mesh refinement at the vertical centerline for the same set of Reynolds numbers, Re is set equal to 1000, 5000, and 10 000.

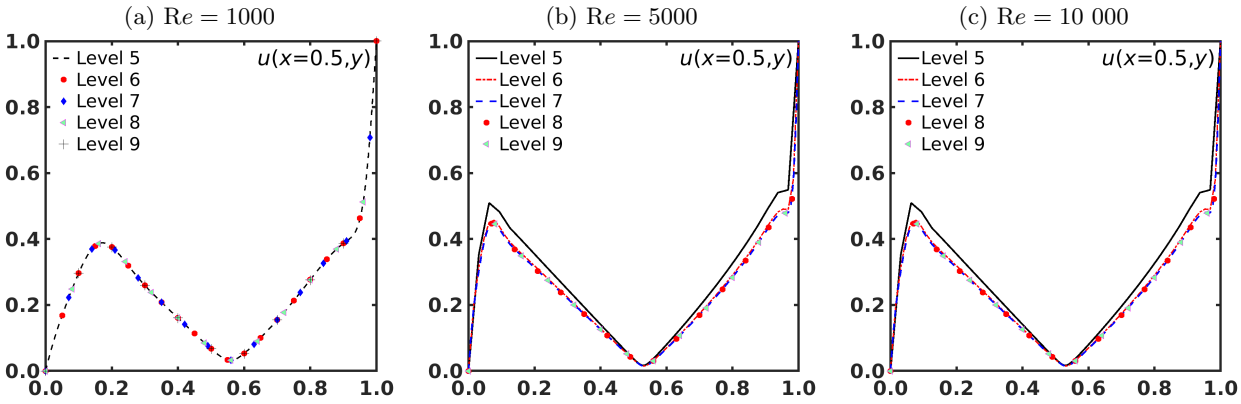

Fig. 4.15: **Newtonian lid-driven cavity flow:** The solutions of velocity magnitude at vertical centerline with respect to mesh refinement computed for different values of Reynolds numbers Re.

Once more, the velocity magnitude cutlines solutions, in Figure 4.15, show mesh refinement convergence in accordance with convection dominations connected to each particular Reynolds number. Most important conclusion is the confirmation of the designated least mesh refinement level to accept the solution irrespective of the complexity of the problem providing mesh converged solutions.

After raising awareness on the minimum mesh refinement for obtaining accurate solutions for problems having mesh refinement convergence in the global sense or point-wise, we proceed similarly with problems that might lack such property for artificial reasons, for instance due to regularization issue in quasi-Newtonian modeling of yield stress fluids.

Quasi-Newtonian modeling approach for yield stress materials uses an approximated norm of shear rate with an artificial regularization parameter, which may cause the solutions to be regularization dependent. In next Subsection §4.3.2, we investigate the accuracy of viscoplastic lid-driven cavity flow solutions with respect to the optimal settings of the pair regularization parameter and mesh refinement, and the corresponding Newton-multigrid solver behavior.

4.3.2 Bingham Viscoplastic Lid-driven Cavity Flow

This subsection is devoted to the viscoplastic lid-driven cavity flow benchmark. The quasi-Newtonian modeling approach for viscoplastic materials introduces a regularization parameter to get a well-defined extended viscosity function in the whole computational domain. We investigate the accurate growth and location of unyielded regions with respect to the optimal settings of regularization and mesh refinement, for increased values of the yield stress parameter. Moreover, we analyze the corresponding Newton-multigrid solver convergence with respect to yield stress and regularization parameters. Meanwhile, we check the optimal strategy for fast convergence of the nonlinear solver.

In Figure 4.16, we plot the interface between unyielded and yielded regions in terms of shear rate for moderately increased values of the yield stress parameter.

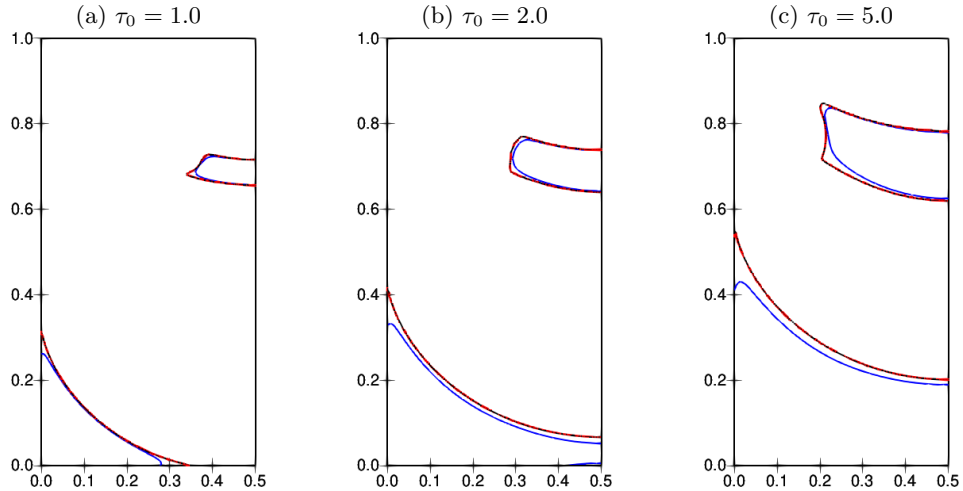

Fig. 4.16: **Viscoplastic lid-driven cavity flow:** Impact of the regularization parameter on the accurate track of the interface between unyielded and yielded regions for different yield stress parameter values, while $\eta_0 = 1.0$, and the regularization parameter is set to $k = 10^2$ (blue), $k = 10^3$ (red) and $k = 10^4$ (black). The solutions are calculated at mesh-refinement level 7.

Viscoplastic materials inhabit the coexistence of yielded and unyielded regions, modeled in a quasi-Newtonian approach with a unified extended viscosity function defined for both regions. The extended viscosity function leads to flow problems with regularization parameter dependent solutions, which have a direct impact on the accurate track of the interfaces between unyielded and yielded regions. In the context of this work, we use the Papanastasiou approximation, which requires a very large regularization parameter to get accurate solutions. This is clearly manifested in Figure 4.16, for a wide range of regularization parameter, the plotted interfaces show convergence with respect to an increase in the regularization parameter for different values of the yield stress parameter, that is, no further changes beyond the regularization parameter 1000.

Viscoplastic cavity flows benchmark presents a modeling challenge in two folds: on the one hand the proper track of the interface between unyielded and yielded regions, and on the other the exact location and shape of the formed unyielded regions with respect to yield stress parameters.

In Figure 4.17, we present the location and shape of the formed unyielded (red) and yielded (blue) regions in the full cavity, and in relative position to the stream function contours. Meanwhile, we plot the convergence of the interfaces with respect to the regularization parameter.

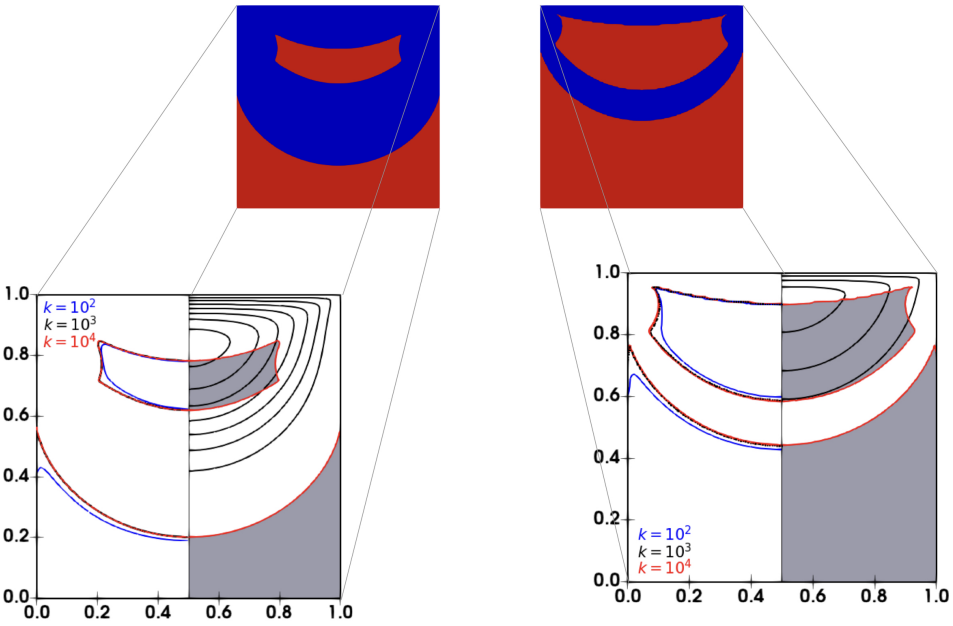

Fig. 4.17: **Viscoplastic lid-driven cavity flow:** Impact of regularization parameter on the accurate track of the interface between unyielded and yielded regions with a relative view of unyielded and unyielded regions, for two different yield stress parameter values $\tau_0 = 5.0$ (LEFT) and $\tau_0 = 50.0$ (RIGHT), while $\eta_0 = 1.0$. The solutions are calculated at mesh-refinement level 7.

Figure 4.17 depicts the formation of two unyielded regions, one resting at the bottom of the cavity and separated from the yielded region with a circular interface, and the other located near the lid of a lip-like shape surrounded by the yielded region. For the two prototype increased yield stress parameter τ_0 values, set equal to 5.0 and 50.0, respectively, both unyielded regions expand and occupy the shrinking yielded

region. Moreover, as the yield stress parameter increases, the intensity of the main vortex decreases and moves toward the lid. Furthermore, as the regularization parameter increases, the interfaces between unyielded and yielded regions converge, that is, no further changes beyond the regularization parameter 1000. We are in good agreement with the ones reported in [1].

For a systematic analysis of the accuracy and solver efficiency with respect to modeling parameters, we select a large set of increased yield stress parameter $\{1.0,\ 2.0,\ 5.0,\ 10.0,\ 20.0,\ 50.0\}$. On the one hand, we plot the location and shape of the formed unyielded regions, and the convergence of the interfaces between unyielded and yielded regions with respect to regularization parameter, and on the other hand we present the corresponding Newton-multigrid behavior on successively refined mesh levels.

In regard to accuracy, we plot in Figure 4.18 on the mesh refinement level 7, the least designated refinement level for obtaining an accurate solution, the location and shape of the formed unyielded regions relatively to the contours of stream function solution on the one hand, and the convergence of the corresponding interfaces with respect to regularization parameter on the other hand.

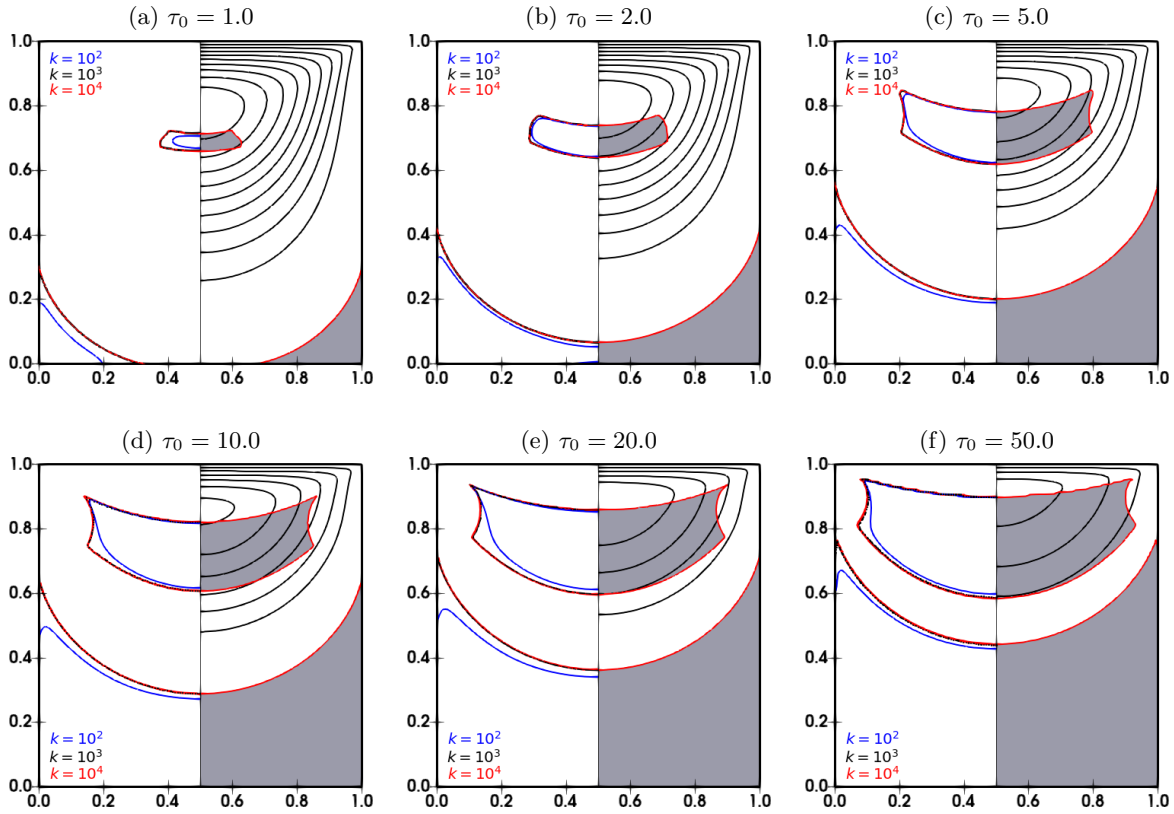

Fig. 4.18: **Viscoplastic lid-driven cavity flow:** The relative position of the unyielded and yielded zones to stream function contours for increased yield stress parameter τ_0 values. The other parameters are set to $\eta_0 = 1.0$, and $k = 10^4$. The solutions are calculated at mesh-refinement level 7.

Firstly, concerning the location and shape of the formed unyielded regions relative to the contours of the stream function solution, Figure 4.18 shows the formation of three unyielded regions for a very small yield stress parameter, the case of the prototype value of yield stress τ_0 set equal to 1, on the bottom left and

on bottom right corners of the cavity, and the third one of lips-like shape inside the cavity surrounded with yielded region. As the yield stress parameter increases, the two bottom corners unyielded regions expand and submerge to form one unyielded region resting at the bottom of the cavity, which reduces the total sum of unyielded regions to two, one resting at the bottom of the cavity separated from the yielded region with a circular interface, and the other located near the lid of a lip-like shape surrounded by the yielded region. For the prototype set of increased yield stress parameter $\{1.0,\ 2.0,\ 5.0,\ 10.0,\ 20.0,\ 50.0\}$, all unyielded regions expand and occupy the shrinking yielded region. Moreover, as the yield stress parameter increases, the intensity of the main vortex decreases and moves toward the lid.

Secondly, with regard to convergence of interfaces, Figure 4.18 shows that the interfaces between unyielded and yielded regions converge with respect to increases in the regularization parameter, that is, no further changes beyond the regularization parameter 1000.

Concerning the Newton-multigrid solver, we list in Table 4.8 the statistics of number of nonlinear and linear sweeps for successive mesh level refinements with respect to the progressive increases in regularization parameter.

Table 4.8: **Viscoplastic lid-driven cavity flow**: The number of Newton-multigrid iterations, nonlinear number of iterations and the average number of multigrid iterations (N/M), with respect to regularization parameter k for different values of yield stress parameter τ_0, for successive mesh refinement levels L.

$k\backslash L$	5	6	7	5	6	7	5	6	7
	$\tau_0 = 1.0$			$\tau_0 = 2.0$			$\tau_0 = 5.0$		
1×10^1	3/1	3/1	3/1	3/1	3/1	3/1	4/1	4/1	4/1
5×10^1	2/1	2/1	2/1	2/1	2/1	2/1	3/1	3/1	3/1
1×10^2	3/1	3/1	3/1	3/1	3/1	3/1	4/1	4/1	4/1
5×10^2	3/1	2/1	2/1	3/1	2/1	3/1	3/2	3/2	3/1
1×10^3	2/2	3/2	3/1	3/1	3/1	4/1	4/1	5/2	5/2
5×10^3	2/1	2/1	4/1	3/1	3/2	6/2	4/1	8/2	6/1
1×10^4	2/1	2/2	5/1	3/1	3/1	6/1	4/1	5/4	6/3
	$\tau_0 = 10.0$			$\tau_0 = 20.0$			$\tau_0 = 50.0$		
1×10^1	5/1	5/1	5/1	6/1	6/1	6/1	5/1	7/1	7/1
5×10^1	4/1	3/1	3/1	4/1	4/1	3/2	5/4	4/2	4/2
1×10^2	5/2	4/1	4/1	5/2	5/2	5/1	6/5	5/4	5/1
5×10^2	5/3	3/2	3/1	4/4	3/4	4/3	5/4	4/2	4/3
1×10^3	5/2	7/4	9/1	5/5	7/2	8/1	5/5	9/2	9/2
5×10^3	5/1	7/3	8/2	6/3	6/4	6/4	6/4	7/2	8/2
1×10^4	6/1	7/2	8/3	6/3	5/5	7/3	6/3	7/3	8/2

The statistics of the Newton-multigrid solver is presented in Table 4.8, in a block-wise manner. Each block corresponds to a particular yield stress parameter value, and displays the Newton-multigrid results with respect to increases in regularization parameter for successive mesh refinement levels. We used the continuation process with respect to regularization to obtain the listed results of Newton-multigrid solver statistics. As we increase the regularization parameter, the corresponding solutions are computed by using a lower value regularized solutions as a start-solutions. It is worth mentioning that for two successive regularization parameter values listed in the table, our continuation strategy uses a non-uniform step-size to increase the regularization parameter values. The blocks correspond to the set of increased yield stress parameter $\{1.0,\ 2.0,\ 5.0,\ 10.0,\ 20.0,\ 50.0\}$.

From Table 4.8, with respect to the linear solver, multigrid shows mesh independent behavior for all blocks of the yield stress parameter. Clearly, the nonlinearity of the problem is increased by either increasing the yield stress parameter or by increasing the regularization parameter. That is, the number of nonlinear iterations is increased moderately with respect to either increasing the yield stress parameter or increasing the regularization parameter. The worth noting remark is that multigrid sweeps increased in perfect accordance. This is quite an interesting result of the combined adaptive nonlinear-linear solvers, where the accuracy of the linear solver is made to match optimally the requirements of the accuracy of the nonlinear solver.

Viscoplastic lid-driven cavity flow investigation provided us with the optimal setting of mesh refinement and regularization parameter for accuracy and the continuation strategy with respect to regularization parameter for efficiency. Now, we are ready to go forward with the investigations of thixoviscoplastic driven cavity flow.

Next, we proceed with the investigations of thixoviscoplastic flow in a lid-driven cavity configuration.

4.3.3 Houška Thixoviscoplastic Lid-driven Cavity Flow

In this subsection, we present thixoviscoplastic lid-driven cavity flow. Thixoviscoplastic flow equations, in contrast to viscoplastic flow equations, induce a two-way coupling, which increase the numerical simulation challenges on two folds. On the one hand, the extended viscosity function integrates the microstructure via thixotropic plastic viscosity and thixotropic yield stress. On the other hand, the set of equations is supplemented with a microstructure evolution equation. This equation integrates the competition processes of aging and rejuvenation, which occur via the interaction of buildup and breakdown functions dependent on two additional model parameters, namely buildup and breakdown parameters.

Here, we also investigate the accurate growth and location of unyielded regions with respect to the optimal settings of regularization and mesh refinement, for increased values of the thixotropic yield stress parameter. We analyze the corresponding Newton-multigrid solver convergence with respect to thixotropic yield stress parameter, and regularization parameter on successive mesh refinement levels. Moreover, we investigate the role played by the microstructure equation throughout the analysis of the types of transitions between unyielded and yielded regions.

After gaining experience with the optimal data settings for accuracy and continuation strategy with respect to the regularization parameter for efficiency for a viscoplastic flow benchmark, we are now ready to investigate thixoviscoplastic lid-driven cavity flow. Indeed, on the one hand we obtained the pointwise convergence of interfaces between unyielded and yielded regions with respect to the regularization parameter k. Furthermore, for the pair mesh refinement level, and regularization parameter k set equal to 7, and 10^4 respectively, we reached the best resolution, and no further clear improvement by either increasing the mesh refinement level or regularization parameter is expected. On the other hand, lower regularization parameter's solutions are used as a start for higher regularization parameter's solution with nonuniform increases in the continuation process.

The thixoviscoplastic lid-driven cavity flow investigations concern the track of the location and shape of the formed unyielded regions with respect to thixotropic yield stress, the performance of Newton-multigrid solver with respect to thixotropic yield stress, regularization parameter, mesh refinement level, and the role of the microstructure equation in defining transitions between regions.

Figure 4.19 sets out the relative position of the rigid zones (shaded area), in terms of shear rate, to stream function contours for a set of increased thixotropic yield stress parameter τ_∞, $\{0.5,\ 1.0,\ 2.0,\ 5.0,\ 10.0,\ 20.0\}$. The solutions are calculated with the resolution threshold pair mesh refinement level, and regularization parameter k set equal to 7, and 10^4, respectively.

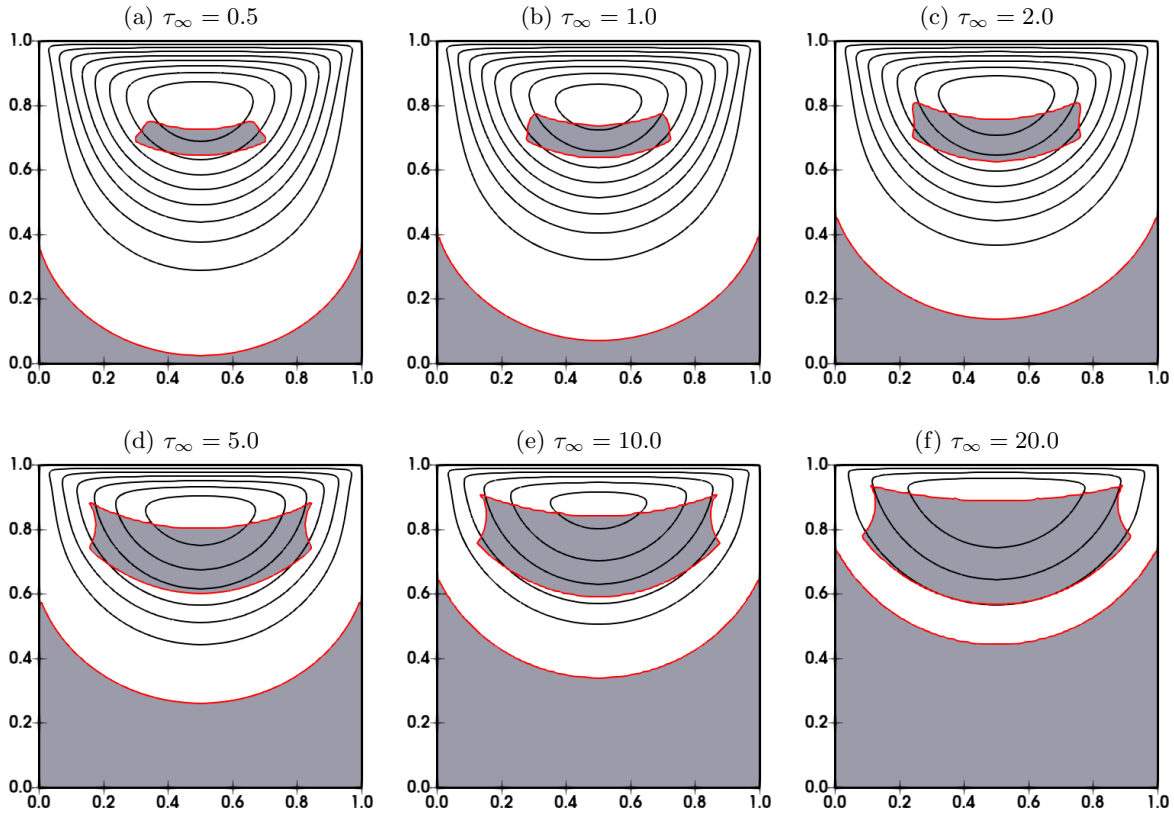

Fig. 4.19: **Thixoviscoplastic lid-driven cavity flow:** The relative position of the unyielded and yielded zones to stream function contours for an increased thixotropic yield stress parameter τ_∞. The other parameters are set to $\eta_0 = 1.0$, $\eta_\infty = 0.0$, $\tau_0 = 1.0$, $k = 10^4$, $\mathcal{M}_a = 1.0$, and $\mathcal{M}_b = 0.1$. The solutions are calculated at mesh-refinement level 7.

Figure 4.19 depicts the formation of two unyielded regions, one resting at the bottom of the cavity and separated from the yielded region with a circular interface, and the other located near the lid of a lip-like shape surrounded by the yielded region. For the set of increased thixotropic yield stress parameter values $\{0.5,\ 1.0,\ 5.0,\ 10.0,\ 20.0\}$, both unyielded regions expand and occupy the shrinking yielded region. Moreover, as the thixotropic yield stress parameter increases, the intensity of the main vortex decreases and moves toward the lid.

The unyielded regions for the set of increased thixotropic yield stress parameter values $\{0.5,\ 1.0,\ 5.0,\ 10.0,\ 20.0\}$, are built on the unyielded regions, which correspond to nonthixotropic yield stress value τ_0 set equal to 1.0. This is concretized in the corresponding larger unyielded regions compared to viscoplastic unyielded regions, which make thixotropic lid-driven cavity flow more challenging for Newton-multigrid solver, due to the additional dependency of the extended viscosity function on microstructure.

Beside the additional numerical challenges within the microstructure equation, the dependency of the extended viscosity function on microstructure increases the numerical challenges of the Newton-multigrid solver for thixoviscoplastic lid-driven cavity flow. Next, we analyze the Newton-multigrid solver behavior for the set of increased thixotropic yield stress parameter values $\{0.5,\ 1.0,\ 5.0,\ 10.0,\ 20.0\}$ with respect to regularization parameter and mesh refinement level. We use a lower range of values for the set of thixotropic yield stress parameter in comparison to the range for values for the set of yield stress parameter in Table 4.8, to maintain the numerical complexity related to plasticity of the same order (see Figure 4.19 and Figure 4.18.) Consequently, the focus is on the analysis of the impact of the upgrade of the thixoviscoplastic flow system with microstructure's equation numerical challenges, namely weak coercivity, extra nonlinearities, and additional degrees of freedom.

In Table 4.9, we summarize the number of Newton-multigrid iterations with respect to different values of the regularization parameter, k, and mesh refinement levels L to obtain the numerical thixoviscoplastic lid-driven cavity flow solutions. The listed results correspond to the set of increased thixotropic yield stress parameter values $\{0.5,\ 1.0,\ 5.0,\ 10.0,\ 20.0\}$. The solutions are calculated using the continuation process with respect to the regularization parameter k. That is, solutions corresponding to higher values of regularization parameter are computed using a lower value regularized solutions as starting solutions. And for two successive regularization parameter values listed in the table, our continuation strategy uses non-uniform multiple steps to increase the regularization parameter values.

Table 4.9: **Thixoviscoplastic lid-driven cavity flow**: The number of Newton-multigrid iterations, nonlinear number of iterations and the average number of multigrid iterations (N/M), with respect to regularization parameter k for different values of yield stress parameter τ_∞, for successive mesh refinement levels L.

$k\backslash L$	5	6	7	5	6	7	5	6	7
	$\tau_\infty = 0.5$			$\tau_\infty = 1.0$			$\tau_\infty = 2.0$		
1×10^1	5/2	5/3	6/2	5/2	5/2	9/1	5/2	5/2	9/1
5×10^1	4/2	4/2	4/2	3/2	3/3	7/1	3/2	3/3	8/1
1×10^2	4/1	4/2	5/1	4/1	4/2	7/1	4/2	4/2	8/1
5×10^2	4/1	4/1	5/1	3/1	4/1	6/1	4/2	4/2	8/1
1×10^3	4/1	4/1	4/1	4/2	4/2	8/1	4/4	6/1	7/1
5×10^3	4/1	4/1	3/2	7/1	9/1	5/1	6/1	9/1	8/1
1×10^4	4/1	4/2	4/2	5/1	7/1	4/1	7/1	10/1	8/2
	$\tau_\infty = 5.0$			$\tau_\infty = 10.0$			$\tau_\infty = 20.0$		
1×10^1	6/2	6/2	10/1	11/1	8/2	11/1	10/1	9/2	11/1
5×10^1	4/2	3/2	11/1	11/1	4/2	7/1	12/1	5/3	9/1
1×10^2	4/2	5/2	11/1	10/1	5/3	8/1	12/1	6/3	10/1
5×10^2	5/2	4/2	10/1	9/1	5/3	5/1	8/1	5/5	11/1
1×10^3	5/2	9/1	10/1	10/1	9/1	7/1	8/2	9/1	9/2
5×10^3	5/1	5/1	5/1	8/1	8/2	6/1	8/1	7/1	11/1
1×10^4	5/1	5/2	5/1	8/3	7/1	5/1	8/2	7/1	9/1

The Newton-multigrid solver's statistics results are listed in Table 4.9, in a block-wise manner. Each block corresponds to a particular thixotropic yield stress parameter value, and displays the Newton-multigrid results with respect to increases in regularization parameter for successive mesh refinement levels. The blocks correspond to the set of increased yield stress parameter $\{0.5,\ 1.0,\ 2.0,\ 5.0,\ 10.0,\ 20.0\}$.

From Table 4.9, similar to the viscoplastic case, the nonlinearity of the problem is increased either by increasing the plasticity in terms of the thixotropic yield stress parameter or by increasing the regularization parameter. The additional numerical complexity related to microstructure equation, namely extra nonlinearities, increased little bit the nonlinear sweeps. With respect to the linear solver, multigrid shows mesh independent behavior for all blocks of the thixotropic yield stress parameter, which confirms the efficient performance of coupled geometric multigrid for multifield problems (additional degrees of freedom) on the one hand, and edge-oriented stabilization for weak coercivity on the other hand.

Numerical simulations provide the flow distribution of thixoviscoplastic material for the main fields, velocity, microstructure, and pressure, as well as numerical quantities, as for instance shear rate. So far, the location and shape of zones have been analyzed by means of shear rate. With the interplay role of shear rate and microstructure in defining the zones, we content to show the flow distributions of the microstructure field only, for the investigation of types of transitions between zones.

We proceed with our investigation to analyze the role played by the microstructure equation in defining the types of transitions between unyielded and yielded regions. The microstructure evolution equation integrates the competition processes of Aging (buildup) and Rejuvenation (breakdown) inhabited in thixotropic material. This process occurs via interaction of buildup and breakdown functions dependent on two additional model parameters, namely buildup and breakdown parameters. We restrict our analysis with respect to breakdown parameter, as such types of transitions are due to the ratio of breakdown parameter and buildup parameter.

In Figure 4.20, we display the micostructure solutions for different values of the breakdown parameter.

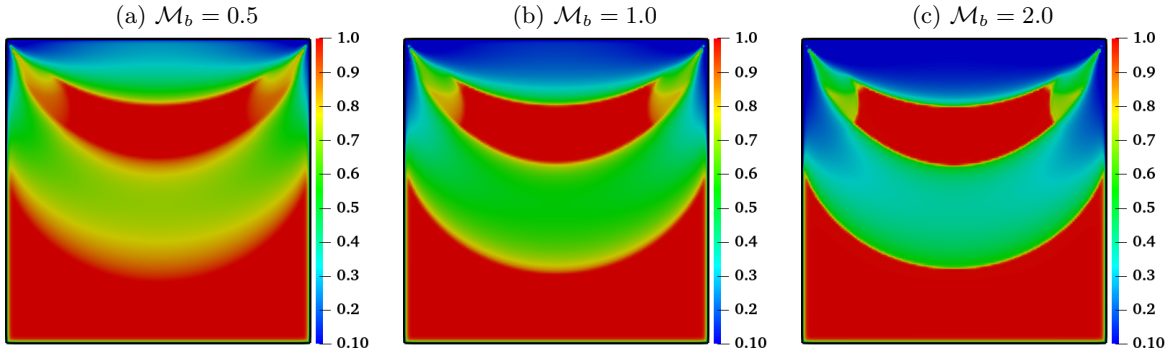

Fig. 4.20: **Thixoviscoplastic lid-driven cavity flow:** Impact of breakdown parameter $\mathcal{M}_b$ on microstructure, while $\eta_0 = 1.0$, $\eta_\infty = 0.0$, $\tau_0 = \tau_\infty = 2.0$, $k = 10^4$, and $\mathcal{M}_a = 1.0$. The solutions are calculated at mesh-refinement level 7.

The microstructure solutions lie between zero and unity, and it take values close to unity for indicating unyielded zones in Figure 4.20. Moreover, a clear smooth transition occurs between zones, termed as *shear localization*, for relatively small values of breakdown parameter. As the breakdown parameter increases, the transitions get sharper and reveal the *shear band* phenomenon.

In this Section §4.3, we analyzed thixoviscoplastic lid-driven cavity flow. Lid-driven cavity flow is a well accepted benchmark in academia. In the context of this work it is used mainly, on the one hand to validate point-wise mesh convergence of solutions, and to analyze the performance of the Newton-multigrid solver for coupled multifield problems on the other hand.

In Subsection §4.3.1, we presented a Newtonian lid-driven cavity flow benchmark to validate our numerical method and simulation algorithm. It provided us with a point-wise benchmark, in terms of cutline solutions, and well-studied vortices, with respect to Reynolds number. We got mesh convergence for both, global quantity (in terms of kinetic energy), and point-wisely (in terms of vertical centerline velocity magnitude cutlines and the locations of vortices). Moreover, we achieved mesh refinement independent behavior for Newton-multigrid solver for a wide range of Reynolds number. Furthermore, since the Newtonian flow is free from regularization effects, which occur for our choice of quasi-Newtonian modeling approach for viscoplastic and thixoviscoplastic flows, we have a reference base for a mesh refinement for FEM solutions point-wisely.

In Subsection §4.3.2, we analyzed the viscoplastic lid-driven cavity flow benchmark. We used the quasi-Newtonian modeling approach for yield stress materials, which introduces a regularization parameter to get a well-defined extended viscosity function in whole computational domain. We investigated the accurate growth and location of unyielded regions. Our findings are the optimal data settings for accuracy and continuation strategy with respect to regularization parameter for efficiency for a viscoplastic flow benchmark. On the one hand, we obtained the point-wise convergence of interfaces between unyielded and yielded regions with respect to regularization parameter k. Furthermore, for the pair mesh refinement level, and regularization parameter k set equal to 7, and 10^4 respectively, we reached the best resolution beyond which no further clear improvement by either increasing the mesh refinement level or regularization parameter is expected. On the other hand, lower-regularization parameter's solutions are used as a start for higher-regularization parameter's solutions with nonuniform increases in continuation process. With respect to the Newton-multigrid solver, we got a mesh independent behavior of linear multigrid solver, and the number of multigrid sweeps increased in perfect accordance with the nonlinear solver's sweeps. That is, the accuracy of the linear solver matches optimally the requirements for the accuracy of the nonlinear solver.

In Subsection §4.3.3, we presented the thixoviscoplastic lid-driven cavity flow. Thixoviscoplastic flow equations are an upgrade of generalized viscoplastic Stokes equations in two aspects. On the one hand, the extended viscosity function integrates the microstructure via thixotropic plastic viscosity and thixotropic yield stress. On other hand, the set of equations is supplemented with a microstructure evolution equation. This equation reflects the competition process of Aging and Rejuvenation, which occurs via the interaction of buildup and breakdown functions dependent on two additional model parameters, namely buildup and breakdown parameters. We maintained the numerical complexity related to plasticity of the same order as viscoplastic problem to analyze the impact of the upgrade of the thixoviscoplastic flow system with microstructure numerical challenges, namely weak coercivity, extra nonlinearities, and additional degrees of freedom. The multigrid linear solver showed mesh refinement independent behavior, which confirms the efficient performance of coupled geometric multigrid for multifield problems. Moreover, we analyzed the types of transitions between yielded and unyielded regions by monitoring the microstructure equation.

With the extensive study of lid-driven cavity flow as well documented flow configuration in academia, in what follows, we proceed with thixoviscoplastic flow simulations in a simple enough configuration for modeling, the Couette device, and a close enough configuration for industrial and engineering applications, the contraction configuration.

4.4 Thixoviscoplastic Couette flow

In this section, we present thixotropic flow behavior in a simple enough geometry for laboratory experiments and for validation of numerical simulations, Couette device. We study the types of transitions from the quasi-static flow regime to the intermediate flow regime and vice versa with respect to the changes in the intensity of the breakdown parameter.

We start by recalling the FEM modeling study of the frictional and collisional powder material sheared in the Couette device [51]. The aim of this recall is to validate our newly developed numerical tools with a well established study both in modeling and simulation on the one hand, and on the other hand to go forward with the ongoing research of analyzing the related types of transitions by including thixotropy.

In Couette flow, the material is sheared in two concentric cylinders with an inner and an outer radii r_{in} and r_{out} defined as follows:

$$r_{\text{in}} = \zeta/(1-\zeta), \tag{4.2}$$

$$r_{\text{out}} = 1/(1-\zeta), \tag{4.3}$$

where ζ denotes the radii ratio. The inner cylinder is made under rotation speed

$$\boldsymbol{u} = u(r_{\text{in}})\, e_\theta, \tag{4.4}$$

where $u(r_{\text{in}})$ is the speed given in revolutions per minute unit RPM, and e_θ denotes the unit tangent vector. The outer cylinder is kept static, $r_{\text{out}} = 0$ RPM [51].

In Figure 4.21 (LEFT), we show the Couette device used in the laboratory experiment for the modeling study of a unified constitutive equation for frictional and collisional powder flows. For detailed measure of material characteristics in Couette device namely torque and normal stress measurements, we refer to [51, 50]. For our numerical simulations, we are using a two-dimensional (r, θ) cut-plane, and a simple schematic representation of it is sketched in Figure 4.21 (RIGHT).

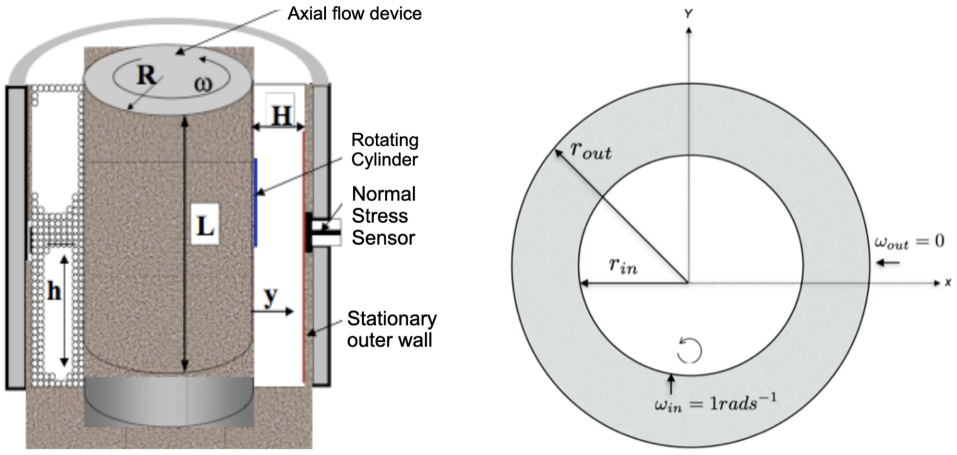

Fig. 4.21: **Thixoviscoplastic Couette flow:** Couette device and its schematic representation.

The numerical method defined so far, in this thesis, yields the pressure distribution, microstructure, and velocity fields as first solutions in the gap between two concentric cylinders. From the velocity results,

we calculate the velocity gradients, then express the stresses in the constitutive law for the respective materials, namely the total stress tensor

$$\mathbf{T}_{ij} = -p\mathbf{I} + \boldsymbol{\sigma}_{ij}. \tag{4.5}$$

The torque force, denoted by F, exerted on the inner cylinder as a function of its rotational speed is then computed as follows:

$$F = -\oint_S (\boldsymbol{x} - \boldsymbol{x}_0) \cdot \mathbf{T} \cdot \boldsymbol{n}\, dS, \tag{4.6}$$

where S is the inner-cylinder surface, $\boldsymbol{x}_0$ is the center of the concentric Couette device, and $\boldsymbol{n}$ the directional unit vector.

In Figure 4.22, we present the comparison of numerical solutions with experimental data of the ratio of average shear, calculated from the torque, to normal stresses measurement on the rotating cylinder versus the shear rate. Here, it should be made clear that the experimental data itself is used as an input in the model with the simple aim to validate our developed numerical tools.

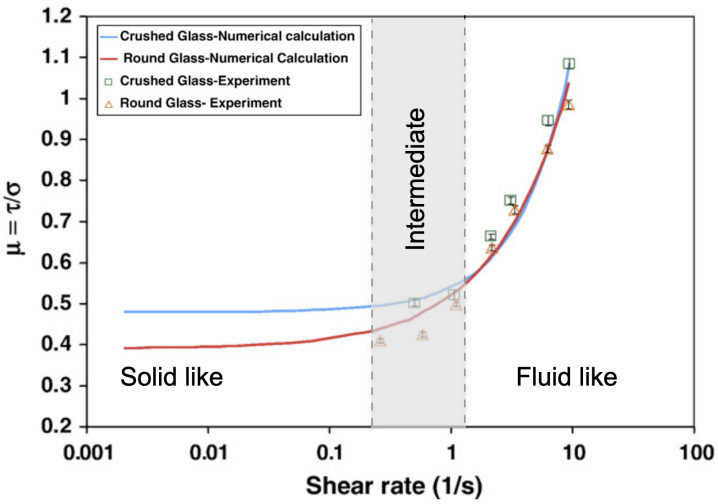

Fig. 4.22: **Thixoviscoplastic Couette flow:** Comparison of numerical solutions, of the ratio of average shear to normal stresses vs. shear rate, to experiments [51].

Clearly, the newly developed numerical methods do not introduce errors to experimental data. Furthermore, we can see the two regions, solid-like and fluid-like and an intermediate one, which we intend to investigate. That is, how the flow changes its behavior in the intermediate region referred as the type of transitions study.

In order to calibrate the code parameter for the optimal settings, we continue with the validation of our numerical method on standard models, namely Newtonian fluid and Bingham viscoplastic with the well conducted study for Couette flow in [51].

The FEM modeling study of Couette flow [51] is based on a stabilized low order nonconforming rotated bilinear FEM approximation for velocity on a quadrilateral in conjunction with piece-wise constant for the pressure approximation on the one hand. On the other hand, with respect to the solver aspect, it uses the monolithic Newton-multigrid method based on a combined adaptive continuous Newton's method based on the operator-splitting approach for the Jacobian calculation and geometric multigrid.

In Figure 4.23, we validate our code against the one used in [51] for the numerical calculation of torque on the inner rotating cylinder as a function of the rotational speed of the inner cylinder (in RPM) for Newtonian liquid and Bingham plastic. This is a multi-aspect validation, that is approximations aspect as well as solver aspect. In other words, accuracy and efficiency aspects for the optimal code's parameter settings of the new developed numerical method.

The parameters concerned with the calibration, for the optimal parameter settings for the code developed in this study, are mainly user defined and problem dependent parameters, as for instance user-defined edge-oriented free-parameter as well as the regularization parameter. The torque for the simulation

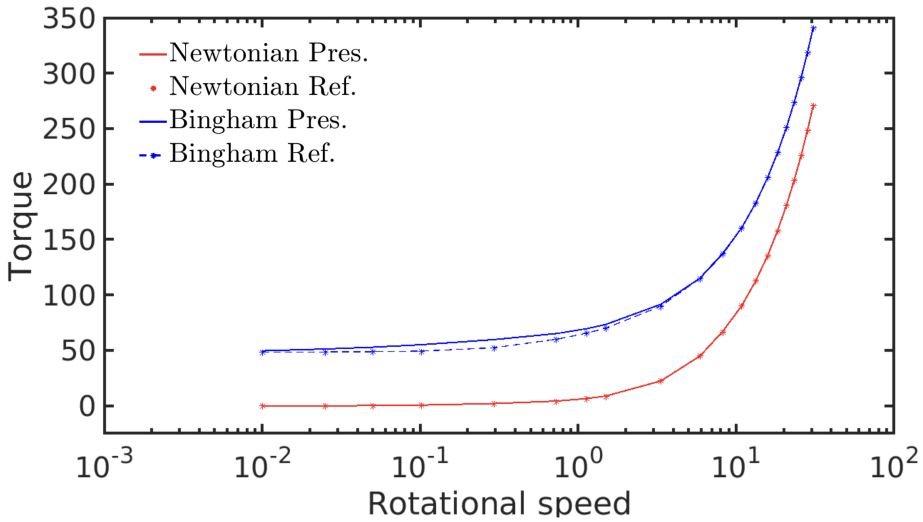

Fig. 4.23: **Thixoviscoplastic Couette flow:** The torque on the inner rotating cylinder as a function of the rotational speed of the inner cylinder (in RPM). Validation with respect to literature [51] for Newtonian fluids, and for Bingham viscoplastic materials.

depicted in Figure 4.23 is calculated on the inner rotating cylinder. The flow parameter used for the simulations, namely nonthixotropic viscosity η_0 is set to unity for Newtonian as well as for Bingham material, and the nonthixotropic yield stress for Bingham material τ_0 is set to 0.48 similar to [51].

After getting the optimal parameter settings for these two simple nonthixotropic models, we go forward to include thixotropy phenomenon for this configuration. To keep the new thixotropic phenomenon under control, we simply use a linear combination of Newtonian and Bingham flows with a microstructure, as expressed via Houška's model.
Our choice of Houška's thixotropic material is purely theoretical driven. Firstly, for its simplicity, as a linear combination of Newtonian and Bingham flows with a microstructure, providing extra parameter which made it possible to analyze the type of transitions. Secondly, for the unavailability of thixotropy's experimental data with corresponding models.

Next, we supplement the simulation results of the two nonthixotropic models, the Newtonian and Bingham models Figure 4.23, with an additional thixotropic model.

Thixoviscoplastic stress in Houška's model is a simple modification of viscoplastic stress by taking into consideration the internal material microstructure using an additional field, named as microstructure. That is, the nonthixotropic plastic viscosity as well as the nonthixotropic yield stress are upgraded to be microstructure dependent.

In Figure 4.24, we present a simple calculation with the numerical method for the torque on the inner rotating cylinder as a function of the rotational speed of the inner cylinder (in RPM). We show the three continua Newtonian liquid, Bingham plastic, Houška's thixotropic.

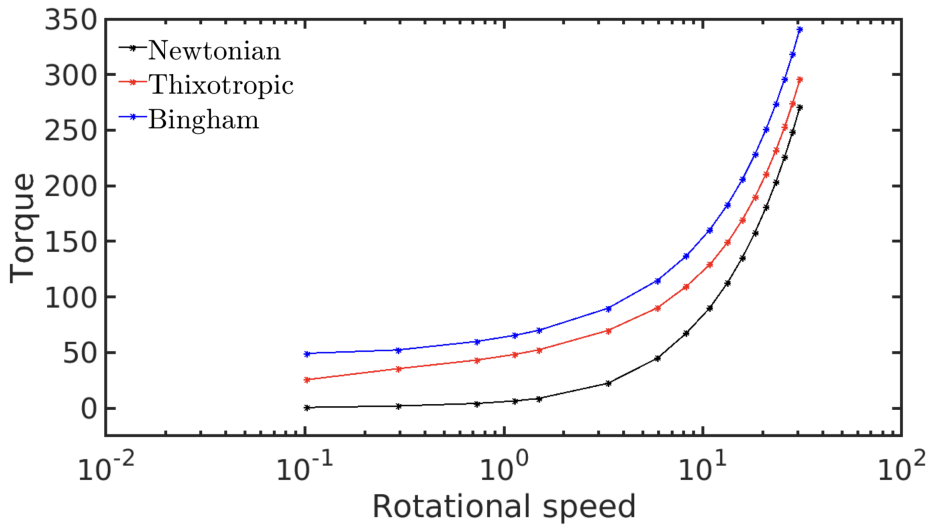

Fig. 4.24: **Thixoviscoplastic Couette flow:** The torque on the inner rotating cylinder as a function of the rotational speed of the inner cylinder (in RPM). The full spectrum of the numerical solution of thixoviscoplastic flows (a) Newtonian fluid, (b) Bingham plastic, (c) Houška's thixotropic.

As planned for this simulation, to proceed with the same range of optimal parameter settings, the thixotropic flow is encompassed between the two extremities, Newtonian liquid and Bingham plastic, which is a direct response of the model as a linear combination with a microstructure. We can see the changes in the flow characteristics in terms of force for all materials with respect to rotational speed. That is, the typical yield stress material phenomenon, for Bingham, and thixotropic materials, and Newtonian phenomenon, for Newtonian fluid. Furthermore, the way the flow is changing its characteristics is not reflected in Figure 4.24.
In general, the deformation mechanism study of flow characteristics is a long-standing research area for the modeling and simulation community alike. It allows to predict the material structure, failure as for instance, and helps to intervene in many engineering and natural fields.

In upcoming numerical simulations, we investigate the deformation mechanism of shear band and shear localization via the investigation the types of transitions in flow characteristics for thixoviscoplastic material.

Houska's thixotropic model is a straightforward extension of the viscoplastic constitutive equation as a linear combination of shear rate independent and shear rate dependent stress with microstructure, coupled to the microstructure evolution equation. The microstructure evolution equation induces the time-dependent process of competition between the destruction (breakdown) and the construction (buildup) processes inhabited in the material, which provides extra parameters to investigate the type of transitions, namely breakdown parameter and buildup parameter.

We dismiss the average quantity in favor of local quantity to investigate the types of transitions between solid-like and fluid-like regions. We show in Figure 4.25 the radial solution profiles for microstructure with respect to breakdown parameter, similar as in [11, 47].

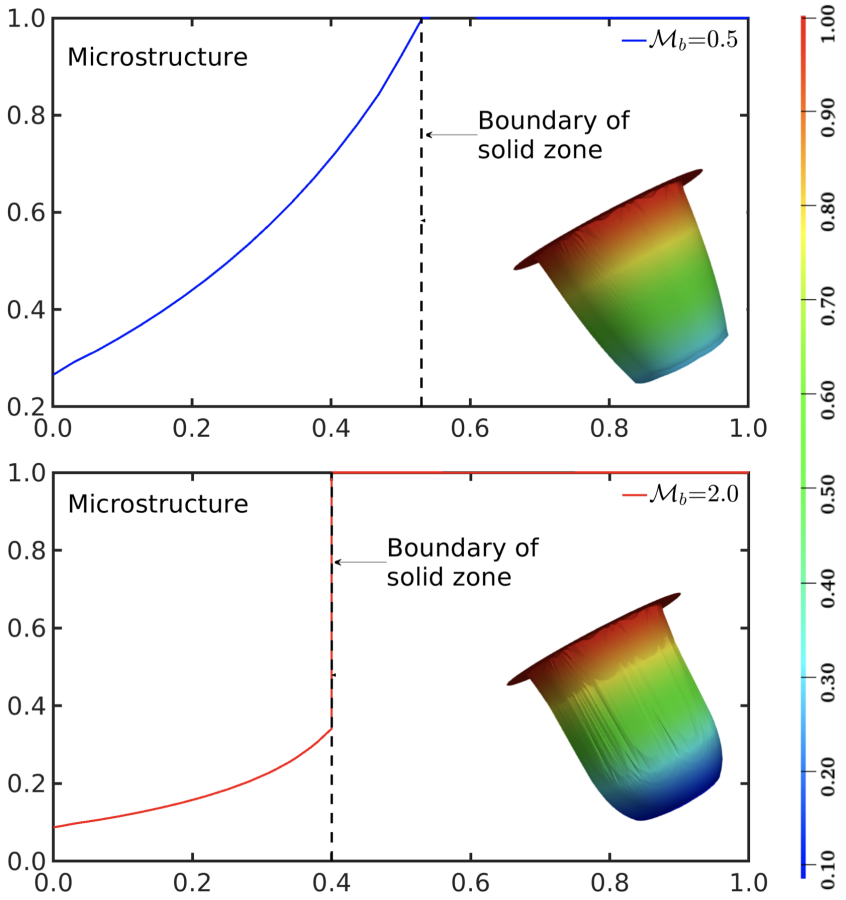

Fig. 4.25: **Thixoviscoplastic Couette flow:** The radial solution profiles of microstructure for different values of the breakdown parameter $\mathcal{M}_b$. The other parameters are set as $\eta_0 = \eta_\infty = 1.0$, $\tau_0 = 2.0$, $\tau_\infty = 1.0$, $\mathcal{M}_a = 1.0$, and $k = 10^4$.

As expected, the results in Figure 4.25 depict two different regions for the microstructure, a fluid like region and a solid like region, for different breakdown parameter, $\mathcal{M}_b$, ranges. However, each range of breakdown parameter induces a different transition.

Here, the lower value of breakdown parameter, $\mathcal{M}_b$, set equal to 0.5, as prototype of one range, leads to a smooth transition which refer as *shear localization* transition, instead the higher value of breakdown parameter $\mathcal{M}_b$ set equal to 2.0, as prototype of other counterpart range, induce a sharp transition which referred as *shear band* transition.

For better relative comparison, we present both radial solutions of microstructure, which correspond to shear localization and shear band transitions in Figure 4.26.

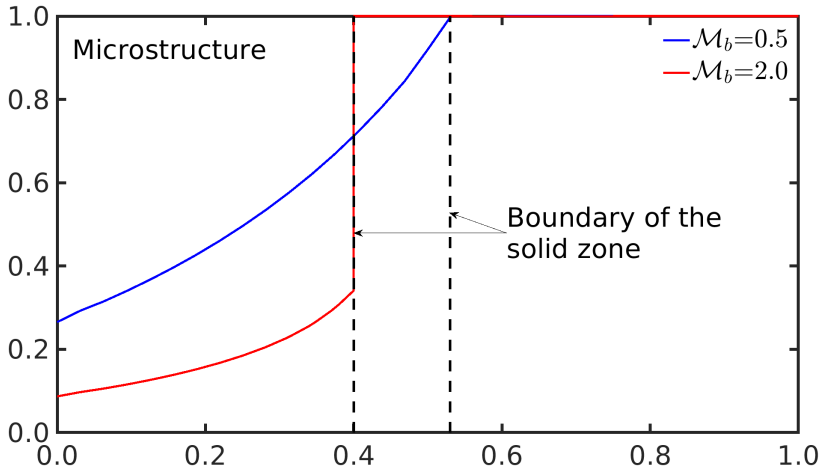

Fig. 4.26: **Thixoviscoplastic Couette flow:**The radial solution profiles of microstructure for different values of breakdown parameter $\mathcal{M}_b$. The other parameters are set as $\eta_0 = \eta_\infty = 1.0$, $\tau_0 = 2.0$, $\tau_\infty = 1.0$, $\mathcal{M}_a = 1.0$, and $k = 10^4$.

Beside the different shear localization and shear band transitions, Figure 4.26 shows the shift of the boundary of the rigid zone towards the center of the Couette device for higher breakdown parameter values. Furthermore, the microstructure field is compressed to lower values. Thus, the thixoviscoplastic material undergoes a sharp transition from fluid-like to solid-like zones. Furthermore, for lower values of the breakdown parameter, the fluid zone has a wider spread in the Couette device with smooth transit between the zones.

The deformation mechanism of shear localization and shear band for thixotropic material in terms of microstructure field is clear. Sure, the TVP flow is nonlinear two-way coupled problem, that is the microstructure is impacted by the velocity, and vice versa. We now proceed with the other counterpart of the coupling to analyze the deformation mechanism of shear localization and shear band for thixotropic material in terms of the velocity field.

As a feedback response of microsturcure, we present the radial solution profiles for velocity in Figure 4.27. The velocity solutions are related to the same simulations as in Figure 4.26 with the different breakdown parameter $\mathcal{M}_b$, which corresponds to the shear localization and shear band phenomena.

The flow of thixoviscoplastic material in the gap of the Couette device is a direct response of the rotating inner cylinder with a user defined uniform speed, set to unity, for both simulations.

For both simulations, with different breakdown parameter values, the velocities are the same at the vicinity of the inner cylinder and take the value of the prescribed rotational speed, which is simply the Dirichlet boundary conditions. As the flow evolves inside the gap, it reflects the material inhabited characteristics. It should be clear that the width of the gap is made to be large enough to cover all types of behavior so that the flow evolve freely. That is, both zones, rigid-like zone and fluid-like zone, coexist simultaneously in order to analyze the deformation mechanism of the flow characteristics.

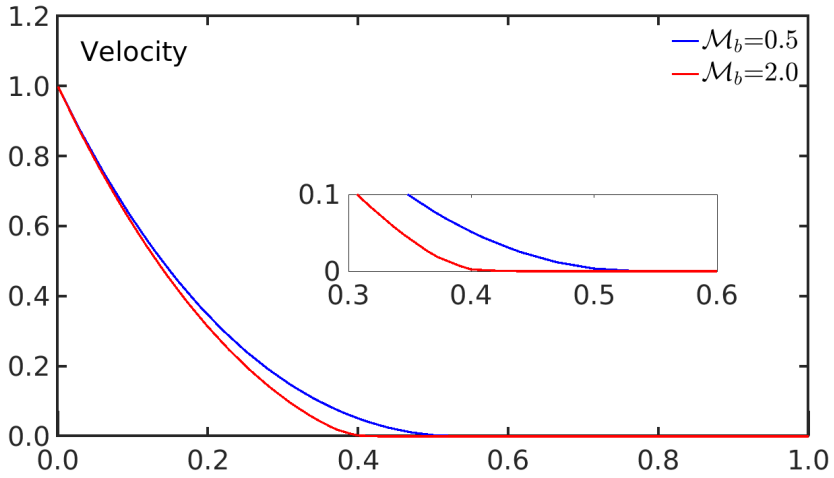

Fig. 4.27: **Thixoviscoplastic Couette flow:** The radial solution profiles of velocity for different breakdown parameter values. The other parameters are set as $\eta_0 = \eta_\infty = 1.0$, $\tau_0 = 2.0$, $\tau_\infty = 1.0$, $\mathcal{M}_a = 1.0$, and $k = 10^4$.

The radial velocity profile for the lower value of the breakdown parameter, as a prototype for the range of shear localization, is smooth which is clearly noticed on the boundary limit of the adjacent zones. On the contrary, the radial velocity profile for the higher value of breakdown parameter, as a prototype for the range of shear band, is nonsmooth on the boundary limit of the adjacent zones. Here, the concept of smooth and sharp transitions is much more manifested on velocity solution.

The boundary limits for the adjacent zones, expressed in terms of the velocity solution profiles, are shifted towards the rotating cylinder for higher value of breakdown parameter. Furthermore, the boundary limits for the adjacent zones in terms of velocity solutions in Figure 4.27 coincide with the adjacent zones in terms of microstructure in Figure 4.26. This is a direct result of the optimality of our parameter settings, that is mainly in this context the mesh refinement and regularization parameter, are optimal for the solution's accuracy.

Thixoviscoplastic problem, in this thesis, in the primitive variables yields the pressure, microstructure, and velocity solutions. Now, we continue our investigation in terms of shear rate, which we calculate from the velocity solution. This investigation is delicate due to the loss of one order of accuracy for the shear rate calculation.

In thixoviscoplastic quasi-Newtonian modeling approach, the extended viscosity function is dependent on microstructure and shear rate. Moreover, the viscosity function is inversely proportional to the shear rate. To overcome the undefined viscosity function with respect to the shear rate, as the rigid zone corresponds to the vanishing shear rate, regularization is used, which affects directly the shear rate at each quadrature point in the flow domain.

From the velocity solutions, we calculate the velocity gradient and get the shear rate which leads to one order loss of accuracy in contrast to microstructure and velocity FEM approximations. In Figure 4.28, we plot the radial profiles of the shear rate calculation for the shear localization and shear band phenomena.

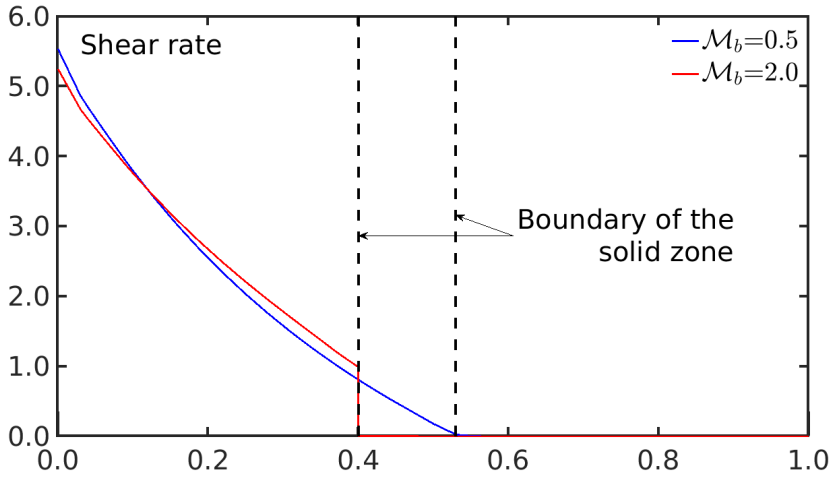

Fig. 4.28: **Thixoviscoplastic Couette flow:** The radial solution profiles of shear rate for different breakdown parameter values. The other parameters are set as $\eta_0 = \eta_\infty = 1.0$, $\tau_0 = 2.0$, $\tau_\infty = 1.0$, $\mathcal{M}_a = 1.0$, and $k = 10^4$.

Similarly two zones, a fluid-like zone and a solid-like zone, are depicted for the two prototype values of breakdown parameter $\mathcal{M}_b$ inducing shear localization and shear band phenomena. For the lower breakdown parameter, the shear rate is higher at the vicinity of the rotating cylinder and decreases for a larger fluid-like zone, before vanishing for the solid-like zone. In contrast, for higher breakdown parameter, the shear rate is lower at the vicinity of the rotating cylinder and slowly decreases to cross the shear rate profile of the lower breakdown value and continue in higher values on a shorter fluid-like zone, before reaching a larger solid-like zone. That is the explanation of the non-monotone behavior of the shear rate curve with respect to breakdown parameter, which leads to shear band phenomena.

The different types of transitions are also observed in terms of shear rate in Figure 4.28. For the shear localization case, shear rate decreases in a relatively larger liquid-like region with increasing distance from the rotating cylinder and vanishes *continuously* at the boundary limit zone and in a relatively shorter solid-like region. For the shear band case, shear rate decreases in a relatively shorter liquid-like region with increasing distance from the rotating cylinder and vanishes *discontinuously* at the boundary limit and in a relatively larger solid-like zone.

The boundary limit zones in terms of shear rate match exactly with the ones expressed in terms of microstructure in Figure 4.26 or in terms of velocity in Figure 4.27. This confirms, once again, the

parameter optimal settings, mesh refinement and regularization, and approves the higher order FEM discretization choice.

For numerical simulations, it is possible to see the flow distribution of thixoviscoplastic material for the main fields, velocity, microstructure, and pressure, on the whole domain as well as all numerically calculated quantities, as for instance shear rate, torque, shear stress , or shear wall stress.

In Figure 4.29, we content to show only the flow distributions of the microstructure field on the whole two-dimensional simulation domain and its corresponding extrusion in three-dimensions for a representative increasing breakdown parameter.

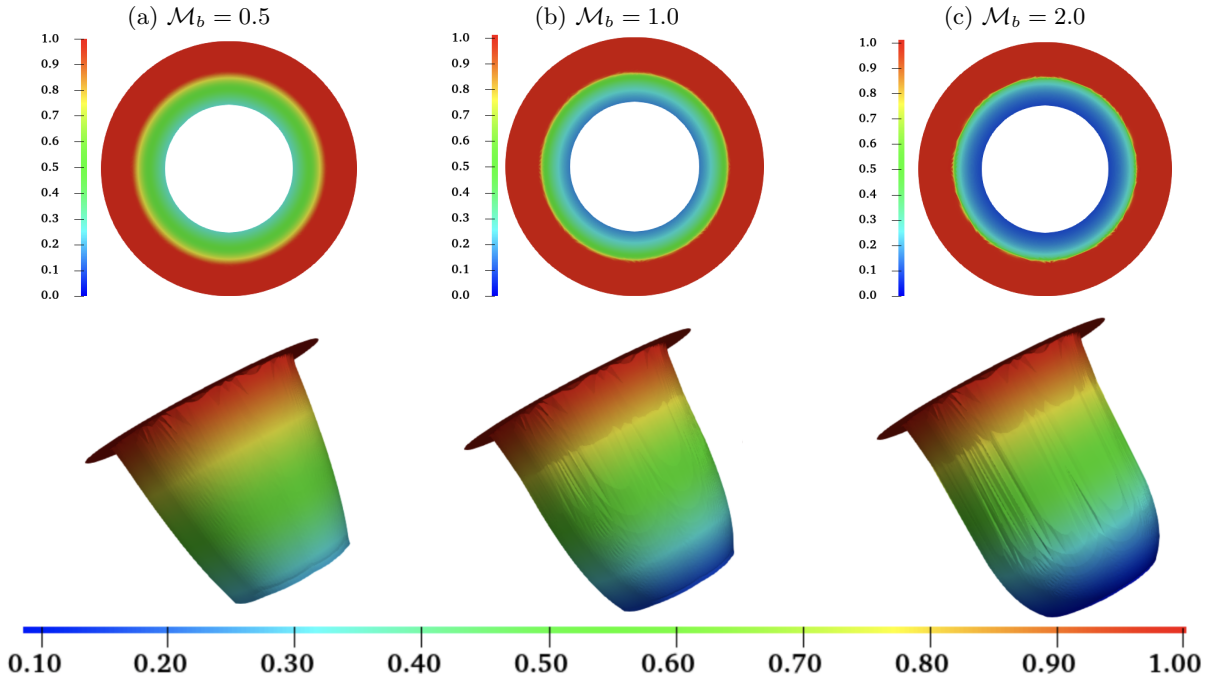

Fig. 4.29: **Thixoviscoplastic Couette flow:** Impact of breakdown parameter $\mathcal{M}_b$ on microstructure, while $\eta_0 = 1.0$, $\eta_\infty = 0.0$, $\tau_0 = 2.0$, $\tau_\infty = 1.0$, $\mathcal{M}_a = 1.0$, and $k = 10^4$. The solutions are calculated at mesh-refinement level 4, and through the integration of constant rotating speed at the inner cylinder of Couette device.

It is clear from Figure 4.29 that the flow is homogeneously distributed in the radial directions confirming the correctness of taking one radial solution for our analysis of the flow characteristics. Furthermore, the *Aging* phenomenon (buildup) corresponds to high microstructure value in the range of the unity, decreasing on relatively shorter intermediate region with an increased breakdown parameter to approach the trivial value for *Rejuvenation* phenomenon (breakdown). As far as the transitions are concerned, the "indicator function" like-behavior of the microstructure fields is manifested clearly for higher breakdown parameter. While for the lower breakdown parameter, the competition region of Aging and Rejuvenation phenomena is wider allowing for smooth transitions.

So far our investigations to analyze the deformation mechanism of shear localization and shear band phenomena are done for thixotropic model via the breakdown parameter. In Figure 4.30, we present the simulation results of our investigations of the impact of thixotropic plastic viscosity and thixotropic yield stress on the flow characteristics.

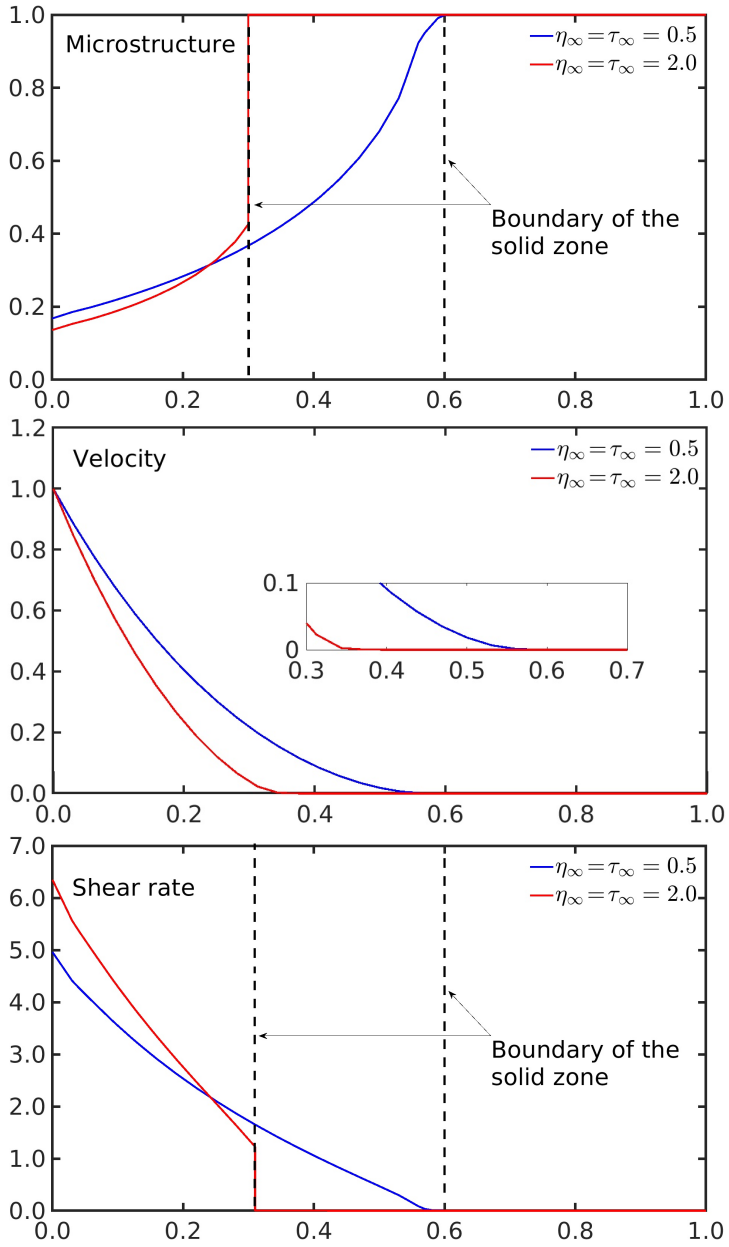

Fig. 4.30: **Thixoviscoplastic Couette flow:** The radial solution profiles with respect to thixotropic viscosity and thixotropic yield stress parameter $(\eta_\infty, \tau_\infty)$. While the other parameters are set to constants $\eta_0 = 1.0$, $\tau_0 = 2.0$, $\mathcal{M}_a = \mathcal{M}_b = 1.0$, and $k = 10^4$.

Figure 4.30 shows that the deformation mechanisms of shear localization and shear band phenomena are replicable simply by monitoring the viscosity function via thixotropic plastic viscosity and thixotropic yield stress.

Our analysis of the deformation mechanism of flow characteristics via breakdown parameter, in Figure 4.26 - Figure 4.29, is done with the aim to highlight the competition of breakdown and buildup processes inhabited in the material via the microstructure evolution equation. This does not necessarily means, that the shear localization and shear band phenomena are exclusively due to the breakdown parameter. Indeed, it is clear that similar phenomenon can be replicated using buildup parameter, as such phenomenon is due to the ratio of breakdown parameter and buildup parameter. It was, however, less clear that we could get the same behavior simply by monitoring the viscosity function, which is now clarified with the additional simulations shown in Figure 4.30.

In this section §4.4, we presented the thixoviscoplastic Couette flow. The Couette device is an interesting configuration, it is simple enough for both numerical simulations and laboratory tests. As far as we are concerned with the numerical simulations, the Couette device reduces the complexity of the boundary conditions to consider only the Dirichlet ones.

Firstly, we revisited the powder Couette flow mainly to validate and calibrate our numerical method for optimal settings with experimental data that we lack for thixoviscoplastic material, and to take forward the investigations of transitions in yield stress flow problems using thixotropy. We used the torque quantity as the means for comparison, as the measured experimental data is available, and the yield stress flow behavior, that is, the coexistence of shear rate independent and shear rate dependent shear stress, is clearly manifested.

Secondly, we dismissed the global quantity, torque, in favor of the local one, point-wise flow field solutions, to investigate the deformation mechanism of shear localization and shear band, that is the type of transitions between fluid-like and solid-like regions. Our investigations of flow characteristics by means of thixoviscoplastic model are extensively done via the breakdown parameter to manifest the competitive processes of Aging, "higher breakdown parameter values" , and Rejuvenation,"lower breakdown parameter values" , of thixoviscoplastic material. For lower values of breakdown parameter, the flow fields evolved on a relatively larger fluid-like region to stop at the boundary limit of the relatively shorter solid-like region. In contrast, for higher values of breakdown parameter, the flow fields evolved on a relatively shorter fluid-like region to stop at the boundary limit of a relatively larger solid-like region. In addition, we presented the flow distributions of microstructure field on the whole two-dimensional simulation domain and its corresponding extrusion in three-dimensions with respect to breakdown parameter values, which highlight the accurate representation of the flow field profiles.

Thirdly, we replicated the deformation mechanism of shear localization and shear band phenomena by monitoring the viscosity function via thixotropic plastic viscosity and thixotropic yield stress to complete the analysis with respect to all thixoviscoplastic model's parameter.

The boundary limit between the fluid-like and solid-like regions matches for all flow field profiles regardless of the thixotropic model's parameter, which confirms the accuracy of the quasi-Newtonian modeling approach modulo the solver's optimal parameter settings. To conclude, the FEM quasi-Newtonian modeling approach and Couette flows are powerful modeling and simulation tools for complex materials, particularly thixoviscoplastic materials.

4.5 Thixoviscoplatic Contraction flow

In this section, we consider a close enough configuration for industrial and engineering applications, the contraction configuration, to analyze the thixotropic phenomena, that is, the competition process of *Aging* and *Shear Rejuvenation*.

Beside the importance of contraction flows in industrial and engineering applications, they are used within the applied mathematics and numerical simulation communities to develop efficient numerical methods and practical algorithms for its challenging flow characteristics. The particularity of this configuration is its reentrant corner, which leads to the generation of recirculating flows. Furthermore, different flow characteristics can be observed, as for instance elongational shear stresses, non-uniqueness, non-regularity, transition and turbulence, where the aspect ratio of contraction can play a role.

Thixotropic contraction flows are far from being classical and have not yet been extensively investigated. Firstly, how the competition processes of aging and shear rejuvenation inhabited in thixotropic material are affected by the contraction. Secondly, if this competition process takes place, how the transitions between fluid-like and solid-like regions are affected by the thixotropic model parameters. In what follows, we content to investigate thixotropic contraction flow. To keep the problem simple and to focus on the flows characteristics at the vicinity of channel's wall, we remove the sharp reentrant corner challenges and consider instead a smoothed one. This simplification do not degrade the importance of our investigation, as the major thixotropic industrial application in our mind is crude oil transportation [80].

We display in Figure 4.31 the curved contraction domain, that is a contraction configuration with a smooth reentrant corner [6, 8].

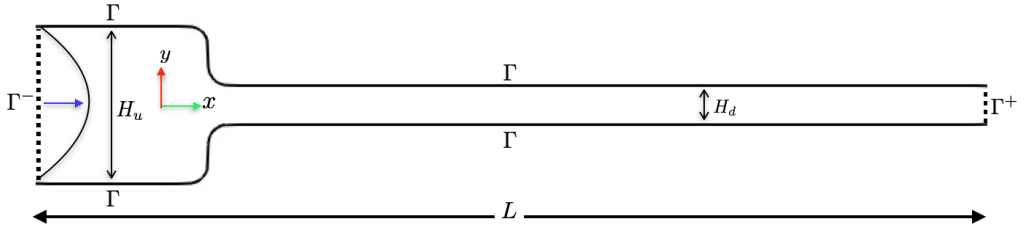

Fig. 4.31: **Thixoviscoplastic contraction flow:** 4:1 Contraction configuration.

The boundary, $\partial\Omega = \Gamma^- \cup \Gamma \cup \Gamma^+$, is composed of three sections, inflow entrance section denoted by Γ^-, upper and lower channel's walls denoted by Γ, and the outflow exit section denoted by Γ^+. The length of the channel is set equal to L. The aspect ratio of contraction is the ratio of the height of the upstream channel, H_u, and the height of the downstream channel, H_d. We use a 4:1 ratio for the current study.

The nonuniform shape of the curved contraction configuration, displayed in Figure 4.31, raises challenges with respect to mesh discretization. Beside the 4:1 aspect ratio of the contraction, the mesh generation has to deal with the circularity of the corners.

We subdivide the computational domain into three patches. Inflow's entrance patch, a two-third of the upstream channel, and outflow's exit patch, a seven-eighth of the downstream channel, both are discretized with structured quadrilaterals. The transit's zone patch, is discretized with mixed condensed structured and unstructured quadrilaterals.

Figure 4.32 presents the computational coarse gird mesh, where we show the different zones, inflow's entrance zone, transit's zone, and outflow's exit zone, with the corresponding quadrilateral composition.

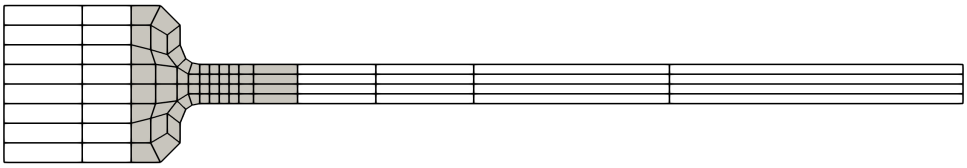

Fig. 4.32: **Thixoviscoplastic contraction flows:** Coarse grid mesh.

To investigate carefully the flow characteristics, we allow the flow to develop constraint-free after the entrance on the one hand, and to avoid any non-physical behavior due to outflow boundary conditions on the other hand, a relatively larger length of the outflow's exit zone is used.

At the inflow boundary, Γ^-, we prescribe the fully-developed flow according to the Houška thixoviscoplastic model for velocity and microstructure. The homogeneous Dirichlet boundary conditions are imposed for velocity at the channel's walls, Γ. In order to avoid the well known nonphysical do-nothing boundary conditions effects, that is, the reentrance of the flow at the outflow boundary, we prescribe instead the Dirichelet boundary conditions which correspond to the fully-developed flow solutions. These imposed Dirichlet boundary conditions do not remove the challenges that the material has to develop inside the channel with respect to the model description to match, at each section point-wisely, with the prescribed conditions. This is challenge in itself, as the comparison of finite element solutions and fully developed prescribed solutions is not trivial.

We opt for the fully developed solutions as boundary data for our finite element simulations due to the nonavailability of Houška thixoviscoplastic exact solution on the one hand, and to avoid the unnecessary extra time to reach the developed flow solutions in the upstream zone on the other hand.

To calculate the fully developed solutions, we assume a x-axis unidirectional flow. With these assumptions, we rewrite a one-dimensional generalized Stokes Houška thixoviscoplastic model to generate the fully developed generalized Stokes Houška TVP discrete data solutions.

The fully developed discrete data solutions of the one-dimensional generalized Stokes Houška thixoviscoplastic model are advantageously used for our developed numerical methods. It is providing less restriction on the mesh refinement. As a consequence, reproducing such solution for two-dimensional FEM generalized Stokes Houška TVP model on very large geometry is "enough as a benchmark" to go forward with the obtained numerical solutions.

Far from the contraction zone, the flow material should develop with respect to the x-axis unidirectional assumptions considered so far. Consequently, the usefulness of the fully developed solutions exceeds the necessary need for boundary conditions, to provide a powerful validation tool and also a parameter calibration tool for optimal settings for our complex thixoviscoplastic model.

In Figure 4.33, we show the comparison of the two-dimensional FEM numerical solution of generalized Stokes Houška TVP model in the downstream channel, that is, x-velocity with respect to the y-axis, and the reduced one-dimensional velocity solution counterpart. The same behavior occurs for the inflow boundary section Γ^{-}, which is not shown here to not overload the text with unnecessary plots.

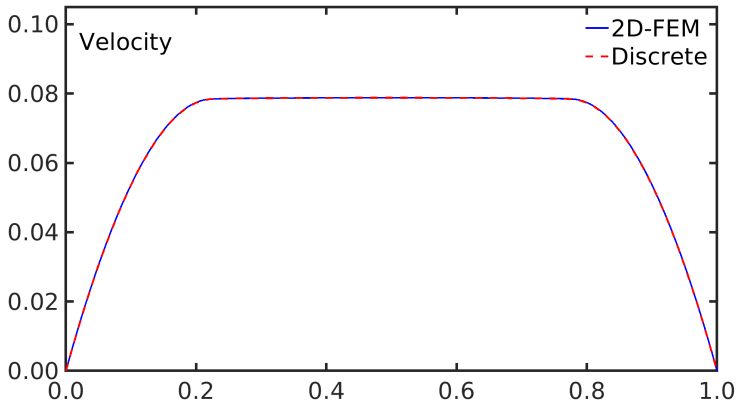

Fig. 4.33: **Thixoviscoplastic contraction flows:** Comparison of the two-dimensional FEM numerical velocity solution of the generalized Stokes Houška TVP model and the velocity solution of the fully developed reduced one-dimensional generalized Stokes Houška TVP model.

It is clear from the comparison presented in Figure 4.33, that the fully developed two-dimensional FEM numerical velocity solution of generalized Stokes Houška TVP model matches perfectly with the velocity solution of reduced one-dimensional generalized Stokes Houška TVP model. Furthermore, the solid-like zone is located at the channel's center, and separated from the channel's walls by fluid-like zones. The fluid-like and solid-like zones are indicated by a parabolic-like function for velocity solutions, with flattened curve to an exact constant value for solid-like zone.

The reduced one-dimensional generalized Stokes Houška TVP model has two unknown scalar quantities, and is defined on a one-dimensional domain. Beside the efficiency and accuracy of the computed numerical solution counterpart, since the analytical exact solution is not available, when used as boundary conditions or validations for the fully developed FEM two-dimensional solution, it does not introduce the interpolation error. Furthermore, it is used to calibrate the two-dimensional FEM code of thixoviscoplastic contraction flow to optimal parameter settings with respect to the velocity field.

To complete the investigations of the generalized Stokes Houška TVP model, we proceed with the analysis of microstructure solutions.

The microstructure equation, in the generalized Stokes Houška thixoviscoplastic model, necessitates the description of inflow boundary conditions. Similarly, we proceed with the assumptions of the fully developed flow and deduce the boundary conditions for the microstructure from the reduced one-dimensional generalized Stokes Houška TVP model.

We show, in Figure 4.34, the comparison of microstructure solutions of the two-dimensional FEM generalized Stokes Houška TVP model in the downstream channel, and the reduced one-dimensional counterpart. The same behavior occurs at the inflow boundary section Γ^{-}, this is not shown here for brevity reason. Moreover, we used moderate values of generalized Stokes Houška TVP model parameters to focus exclusively on the boundary conditions and validation issues.

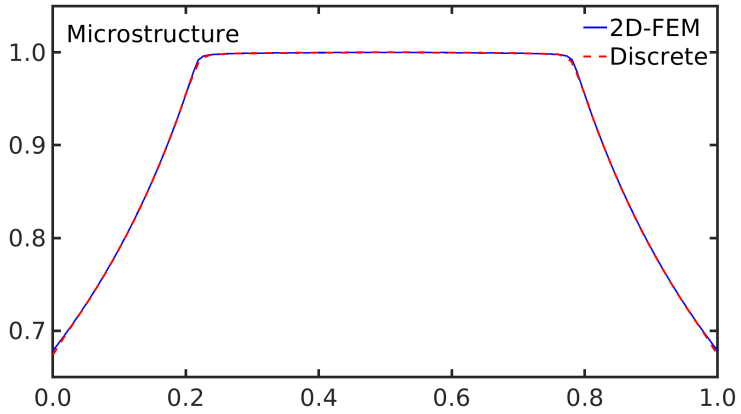

Fig. 4.34: **Thixoviscoplastic contraction flows:** Comparison of the two-dimensional FEM numerical microstructure solution of the generalized Stokes Houška TVP model and the microstructure solution of the fully developed reduced one-dimensional generalized Stokes Houška TVP model.

The microstructure solutions corresponding to the fully developed FEM two-dimensional and the reduced one-dimensional generalized Stokes Houška TVP model match exactly, as depicted in Figure 4.34. The microstructure is an indicator of fluid-like and solid-like zones. Indeed, the values of the microstructure solution lie in the interval $[0, 1]$, and it takes values close to unity for the solid-like zone, and relatively smaller values for the fluid-like zone.

The approximated microstructure solutions of the reduced one-dimensional generalized Stokes Houška TVP model are the perfect choice as boundary conditions for FEM two-dimensional simulations. Also, it is used as a validation of the two-dimensional FEM solutions. Beside, its highly accurate calculation, since it is only a one-dimensional computed solution, it does not introduce interpolation error. Furthermore, it is useful to calibrate the two-dimensional FEM code of thixoviscoplastic contraction flow to optimal parameter settings with respect to microstructure field.

The fully developed FEM two-dimensional generalized Stokes Houška solutions are accepted after validation with the unidirectional reduced model ones. Next, we visualize the two-dimensional FEM solutions on the full simulation domain.

The generalized Stokes Houška's thixoviscoplastic model in primitive variables yields the solutions for velocity, microstructure, and pressure fields. In our simulation, the FEM two-dimensional generalized Stokes Houška model is simulated using discrete data boundary conditions of fully developed flow, calculated from the reduced one-dimensional model. On one hand, at the inflow boundary, Γ^-, we take the fully developed flow data to reduce the computational time for flow to reach the fully developed state in the upstream channel. On the other hand, at the outflow boundary, Γ^+, we use the fully developed flow data for velocity to avoid the well-known effect of do-nothing boundary conditions, that is, the reentrance of velocity at the outflow.

In Figure 4.35, we display the FEM generalized Stokes Houška thixoviscoplastic flow solutions, for velocity, micostructure, and pressure, in 4:1 contraction configuration.

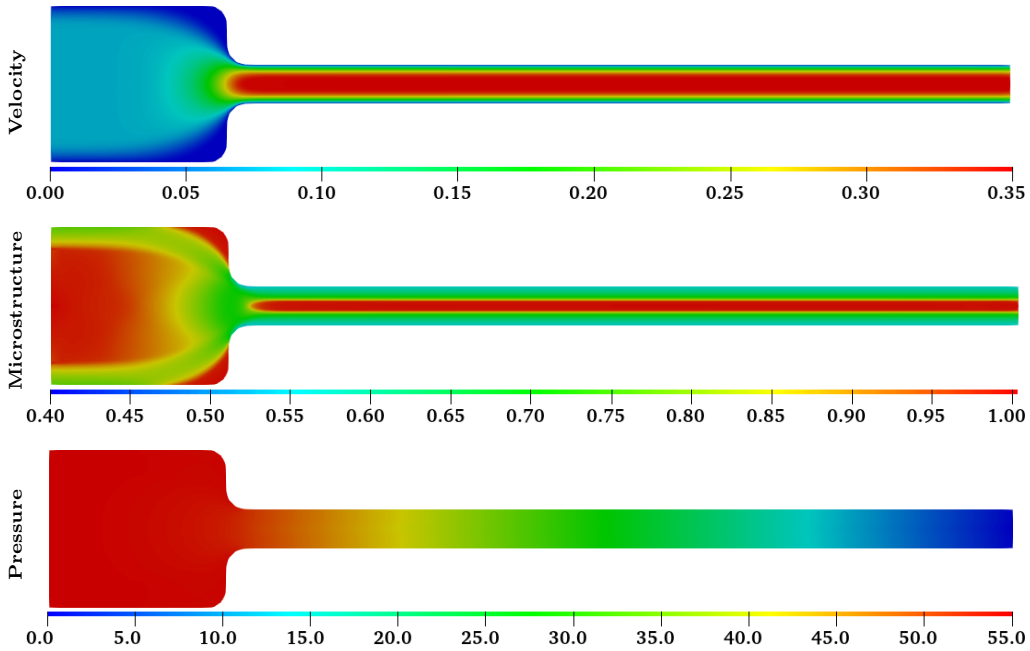

Fig. 4.35: **Thixoviscoplastic contraction flows:** The FEM solutions of generalized Stokes Houška's thixoviscoplastic flow in 4:1 contraction configuration. The parameters are set to constants $\eta_0 = \eta_\infty = 1.0$, $\tau_0 = 0.0$, $\tau_\infty = 0.25$, $\mathcal{M}_a = \mathcal{M}_b = 1.0$, and $k = 10^4$.

For velocity and microstructure solutions, we clearly observe two different behavior. A fully developed flow at the upstream channel and at the downstream channel far from the contraction zone. In the contraction zone, the solid-like zone breaks apart at the entrance of the contraction. The pressure solution is linear along the length of the entire contraction domain.

Along the downstream channel, as the flow is free from the contraction effect, and it satisfies without exception the fully developed flow conditions for velocity and microstructure fields alike. With the x-axis cutlines at each prototype section validation done so far, for velocity in Figure 4.33 and for microstructure in Figure 4.34, and from the visualization of the solutions in 4.35, we can conclude the accuracy of our thixoviscoplastic contraction flow solutions.

As the FEM thixoviscoplastic contraction flow is calibrated to optimal parameter settings with respect to all fields. And with the certitude of replicating the fully developed thixoviscoplastic flow solutions free from reversed flow at the outflow, we proceed with further investigations of thixoviscoplastic phenomena in 4:1 contraction. Firstly, we investigate the thixoviscoplastic phenomena by means of monitoring the viscosity function. We intend to study the effect of thixotropic yield stress parameter on the formation of zones, fluid-like and solid-like, within the contraction domain. Moreover, we check the accurate response of microstructure field to the thixotropic yield stress parameter as an indicator for zones. Secondly, we analyze the competition between aging and rejuvenation, inhabited in thixotropic material with respect to breakdown parameter.

The thixotropic behavior is integrated into the flow through thixotropic plastic viscosity and thixotropic yield stress parameters in the extended viscosity function. Here, we limit our investigation to thixotropic yield stress parameter to focus on the formation and pattern of fluid-like and solid-like zones.

In Figure 4.36, we show the formation of solid-like zones in terms of shear rate. We increase the thixotropic yield stress parameter values, which are set equal to 0.125, 0.25, and 2.0, to analyze the pattern and the increase of solid-like zones. The solid-like zones are differentiated from the fluid-like zone by shading.

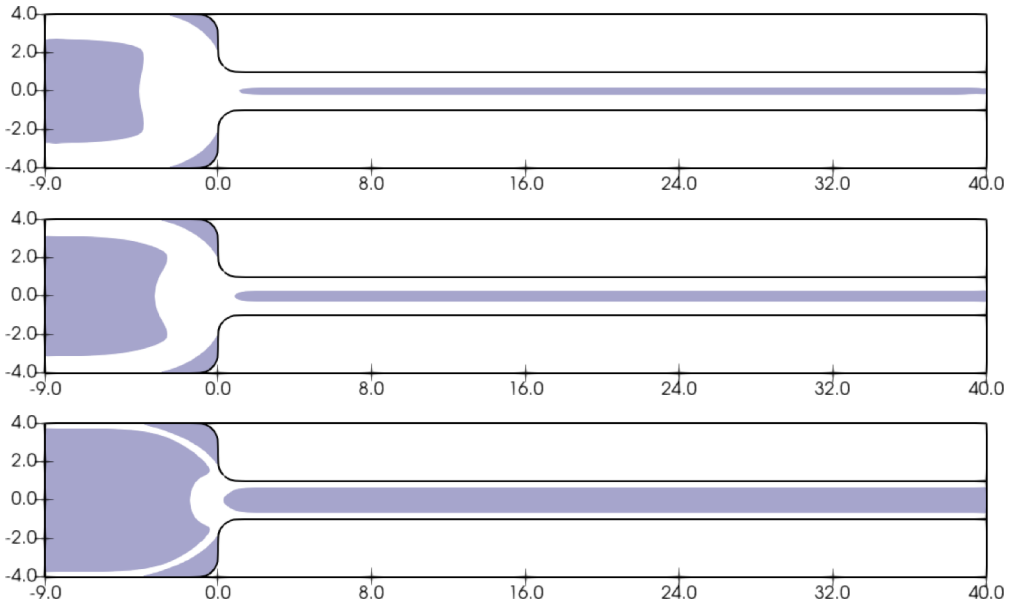

Fig. 4.36: **Thixoviscoplastic contraction flow:** The progressive growth of unyielded regions as a function of thixotropic yield stress parameter τ_∞ for thixoviscoplastic flow in 4:1 contraction. While the other parameters are set to constants $\eta_0 = \eta_\infty = 1.0$, $\tau_0 = 0.0$, $\mathcal{M}_a = \mathcal{M}_b = 1.0$, and $k = 10^4$.

Figure 4.36 depicts the progressive increase of solid-like zones in contraction configuration with respect to increases in thixotropic yield-stress parameter values. Three different types of solid-like zones, separated by a single fluid-like zone, are developed in the contraction. Firstly,a solid-like zone of envelope shape close to the inlet is separated from the upstream channel's walls by a fluid-like zone. Secondly, a solid-like zone along the downstream channel is separated by fluid-like zone from the downstream channel's walls and the contraction zone. Thirdly, a solid-like zone attached to the corners.

The solid-like zones are escalating with respect to the increase of thixotropic plasticity, and take over the shrinking single fluid-like zone. Moreover, the patterns of solid-like and fluid-like zones are relatively independent of thixotropic yield-stress parameter values.

The microstructure usually indicates the solid-like and fluid like zones, with the permissible range between zero and unity. It points out the solid-like zones with values close to unity, while it takes values close to zero for fluid-like zones. Next, we check the indicator aspect of microstructure for the zones with respect to thixotropic plasticity. In other words, we analyze the feedback response of microstructure to thixotropic yield-stress parameter values.

We proceed with the same simulations where the zones are depicted in terms of shear rate , in Figure 4.36, and present the corresponding microstructure field distributions in Figure 4.37 following the same arrangement order with respect to the chosen parameter values of thixotropic plasticity.

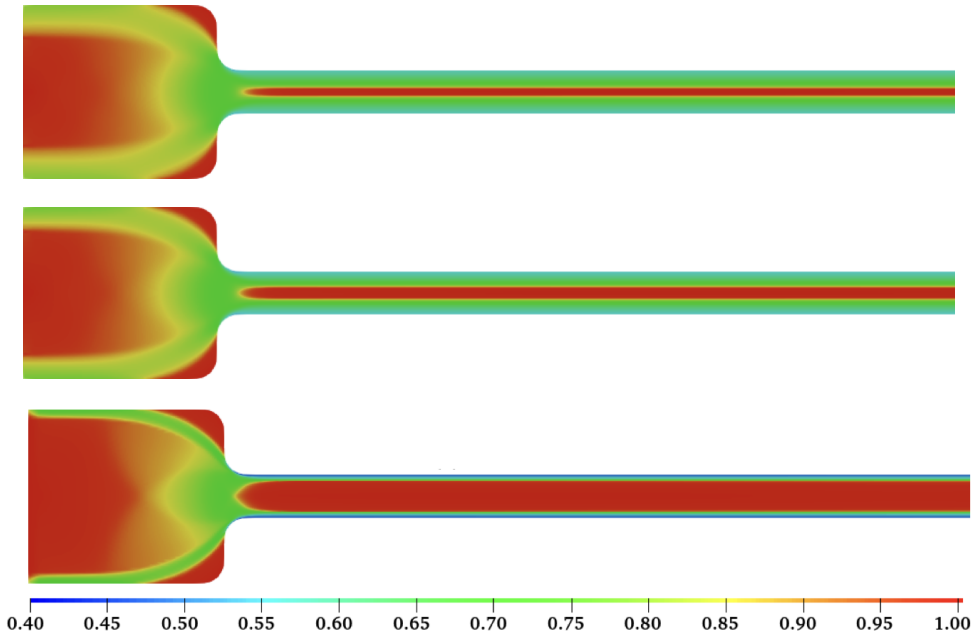

Fig. 4.37: **Thixoviscoplastic contraction flow:** The FEM solutions of microstructure as a function of thixotropic yield stress parameter τ_∞ in 4:1 contraction flow. While the other parameters are set to constants $\eta_0 = \eta_\infty = 1.0$, $\tau_0 = 0.0$, $\mathcal{M}_a = \mathcal{M}_b = 1.0$, and $k = 10^4$.

As expected, the microstructure field takes values close to unity for the solid-like regions indicated by shear rate. Furthermore, Figure 4.37 shows the progressive increase of solid-like zones in contraction configuration with respect to the increase in thixotropic yield-stress parameter values, by means of relatively higher microstructure values close to unity. Relatively to each thixotropoic yield stress parameter value, the solid-like zones pattern is the same for shear rate and microstructure indicator.

After the analysis of the impact of thixotropic plasticity on thixoviscoplastic contraction flow characteristics, we proceed with the played role of the microstructure equation via breakdown parameter, on flow characteristics. The microstructure evolution equation integrates the competition processes of aging (buildup) and rejuvenation (breakdown) inhabited in thixotropic material.

The competition process of aging and rejuvenation occurs via the interaction of buildup and breakdown functions dependent on two additional model parameters, namely buildup and breakdown parameters. Keeping in mind the analysis of types of transitions between the solid-like and fluid-like zones for thixotropic Couette flow, we aim to investigate its manifestation for thixoviscoplastic contraction flow. We restrict our analysis with respect to breakdown parameter, as such types of transitions are due to the ratio of breakdown parameter and buildup parameter. Since the microstructure field perfectly indicates the flow zones, we continue our investigation of the types of transitions only with the microstructure field.

In Figure 4.38, we show the impact of the breakdown parameter on the microstructure field. Two different breakdown parameter values are chosen for our investigation. For visualization clarity, we present the contraction and a zoom of a section of the downstream channel.

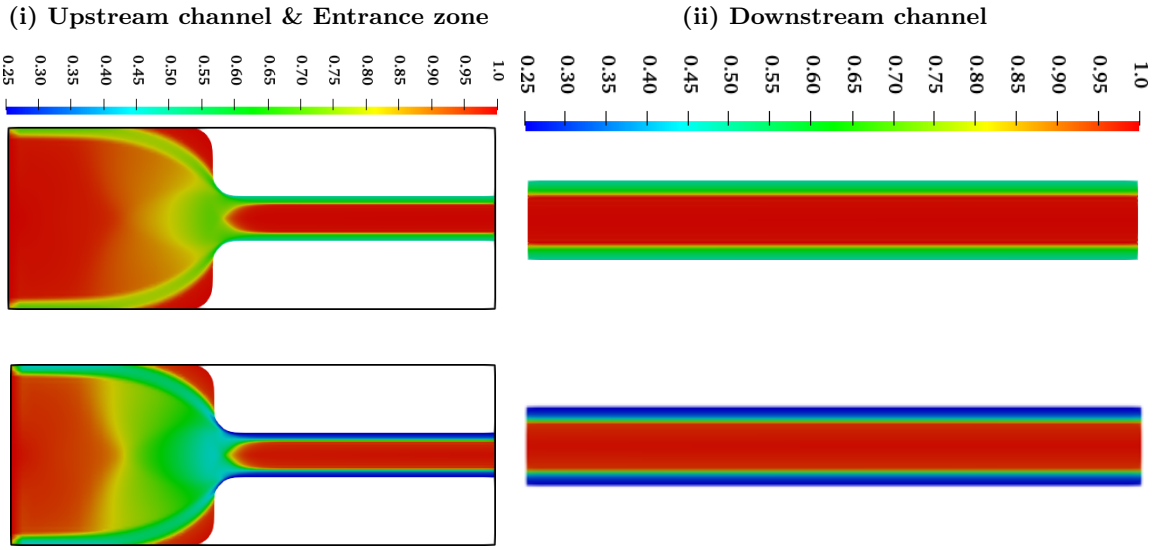

Fig. 4.38: **Thixoviscoplastic contraction flow:** Impact of breakdown parameter $\mathcal{M}_b$ on microstructure, for two different values $\mathcal{M}_b = 1.0$ (TOP) and $\mathcal{M}_b = 2.0$ (BOTTOM). The other parameters are set to constants $\mathcal{M}_a = 1.0$, $\eta_0 = \eta_\infty = 1.0$, $\tau_0 = 0.0$, $\tau_\infty = 2.0$, and $k = 10^4$.

In Figure 4.38, the solid-like zones remain relatively unchanged on corners, the downstream channel, and the upstream channel closer to the entrance. But more noticeable changes occur for the fluid-like zone. The higher breakdown parameter induces extra rejuvenation layers thickness at the vicinity of downstream channel's walls, and expands the fluid-like zone to take over a part of the shrinking solid-like zone at the contraction.

We used in this simulation the contraction configuration with a very large downstream channel, Figure 4.31, to give the flow a larger length to fully develop, and to have enough distance from the outflow boundary section to avoid any possible artifacts of outflow boundary conditions.

To have a close overview, we present again, for the same two-dimensional simulation, a corresponding extrusion in tree-dimension of the contraction with the full downstream channel length and the zoom of downstream channel's section. The simulation is only two-dimensional and the zoomed section of the downstream channel includes the outflow boundary.

In Figure 4.39, we present a three-dimensional extrusion of the contraction and a zoom on a section of the downstream channel, which includes the outflow boundary section. The investigation of the role of microstructure evolution equation on the flow characteristics is done with simple variations of breakdown parameter, while the buildup parameter is kept constant. Two prototype breakdown parameter values are chosen for our investigation. A relatively higher value of $\mathcal{M}_b$ set equal to 2.0, and smaller value of $\mathcal{M}_b$ set equal to unity. We present the two visualizations with same scale of the color map.

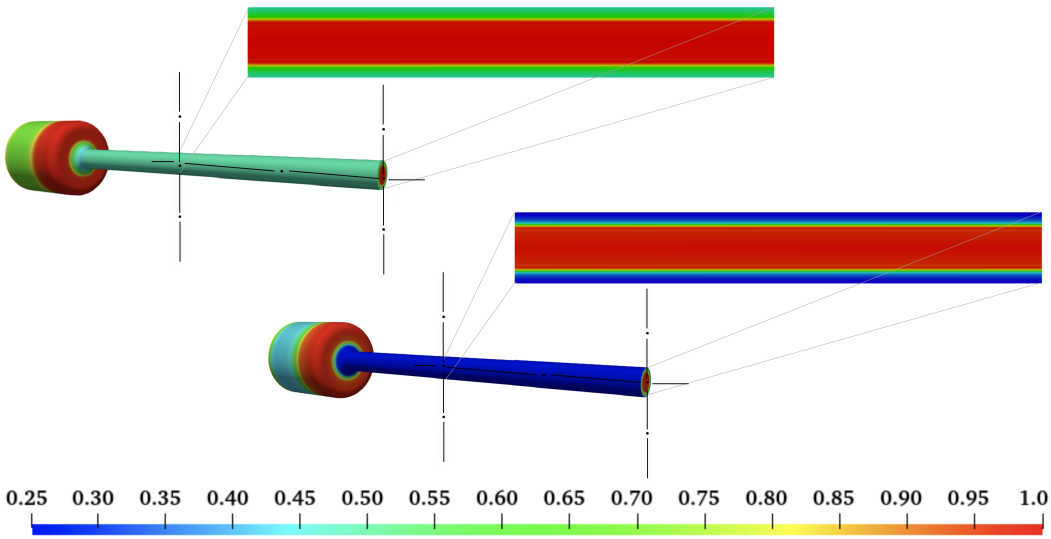

Fig. 4.39: **Thixoviscoplastic contraction flow:** Impact of breakdown parameter $\mathcal{M}_b$ on microstructure, for two different values $\mathcal{M}_b = 1.0$ (TOP) and $\mathcal{M}_b = 2.0$ (BOTTOM), while the other parameters are set to constants $\eta_0 = \eta_\infty = 1.0$, $\tau_0 = 0.0$, $\mathcal{M}_a = 1.0$,$\tau_\infty = 2.0$, and $k = 10^4$.

At a glance of two simulations in Figure 4.38 and in Figure 4.39, the prominent information concerns the types of transitions between fluid-like and solid-like zones. Clearly, the three solid-like zones for thixoviscoplastic contraction flow are formed, close to the inlet with an envelope shape, along the downstream channel, and at the corners, separated with the fluid-like zone. Two types of transitions are differentiated with respect to the prototype values of breakdown parameter. For all transitions between zones, smooth ones correspond to the smaller breakdown parameter values, and sharp ones correspond to the relatively higher breakdown parameter values. The former is named as *shear localization*, and the latter is named *shear band*, for thixoviscoplastic flows.

The additional rejuvenation layers, which are induced for higher breakdown parameter values, are to go with the remarks for thixotropic material. Consequently, thixotropic material remains flowing and not resting along the channel. In contrast, for smaller breakdown parameter values, a relatively higher buildup behavior occurs at the vicinity of the wall restricting the smooth flow of the material. This remark highlights the importance of taking into account the thixotropic rheology of the material in industrial and engineering applications. As for instance in crude oil transportation, the restart pressure settings can be optimized in accordance.

Thixoviscoplastic contraction flow was the focus of Section §4.5. The contraction configuration is an interesting configuration, as it is simple enough for industrial and engineering applications, to analyze the competition process of *Aging* and *Shear Rejuvenation* of thixotropic phenomena.

Firstly, we displayed the computational contraction domain with smooth reentrant corners, and the corresponding coarse mesh in Figure 4.31, and Figure 4.32. The aspect ratio of the contraction is set equal to 4:1, and the length of the downstream channel is kept relatively large for two reasons. On one hand, to give the flow a larger length to fully develop, and to have enough distance from the outflow boundary section to avoid any possible artifacts of outflow boundary conditions on other hand.

Secondly, we rewrite a one-dimensional reduced generalized Stokes Houška thixoviscoplastic model to generate the fully developed generalized Stokes Houška TVP discrete data solutions, which we used as boundary conditions and validation tools. Due to the nonavailability of Houška thixoviscoplastic exact solution, the reduced one-dimensional solutions are a well accepted mechanism to validate the fully developed flows, and provide boundary conditions for the FEM two-dimensional simulations. Moreover, we used the one-dimensional reduced solutions as outflow boundary conditions to get rid of the well-known nonphysical reentrance flow due to the classical "do-nothing" boundary conditions. We displayed the comparison of the reduced one-dimensional and the FEM two-dimensional fully developed solutions for velocity in Figure 4.33, and microstructure in Figure 4.34. Moreover, the FEM two-dimensional generalized Stokes Houška's thixoviscoplastic model in primitive variables yields the solutions for velocity, microstructure, and pressure fields. We displayed, in Figure 4.35, two-dimensional solutions, which confirm the fully developed flow free from any artifacts of the outflow boundary.

Thirdly, we investigated the thixoviscoplastic phenomena by means of monitoring the viscosity function, in terms of thixotropic plasticity. To focus on the formation and pattern of fluid-like and solid-like zones, beside the feedback response of microstructure, we limit our investigation with respect to the variation in thixotropic plasticity. With respect to the increase of thixotropic plasticity, the solid-like zones showed progressive growth and occupied the most part of the simulation domain. Moreover, the microstructure solutions followed the same behavior path, and its values close to unity indicates the solid-like zones. The formation and patterns of solid-like zones are displayed in terms of shear rate and microstructure in Figure 4.36 and Figure 4.37, respectively. The displayed solutions showed a one-to-one accordance behavior of progressive growth of the solid-like zones for a successive increase in thixotropic plasticity, and depicted the response of the microstructure field to thixotropic plasticity as an indicator for zones.

Lastly, we investigated the role played by the microstructure equation to complete the full spectrum of Houška thixoviscoplastic flow in contractions. The microstructure evolution equation integrates the competition processes of aging (buildup) and rejuvenation (breakdown) inhabited in thixotropic material, which allow different types of transitions between the zones via material model parameters. We used the breakdown parameter, to replicate the manifestation of shear localization and shear band in thixotropic contraction flow. For relatively higher prototype value of breakdown shear band occurs, that is, sharp transitions between zones. While for relatively smaller prototype value of breakdown parameter shear localization appears, that is smooth transitions between zones. In addition, extra rejuvenation layers are induced for higher breakdown parameter values, in Figure 4.38 and Figure 4.39, which allows the material to flow smoothly, mainly at the vicinity of the channel's walls. This particularity of thixoviscoplastic flows highlights the need to take into account the inhabited thixotropic material's rheology. A simple take-away from thixoviscoplastic flow in this simple enough configuration for industrial and engineering applications might be the revisit of the optimal restart pressure settings in waxy crude oil transportation.

4.6 Concluding Remarks

In this chapter, we numerically analyzed thixoviscoplastic flows. As a complex upgraded phenomenon of plasticity with thixotropy, numerical simulations are the tools to analyze the mechanism of their interplay. To obtain credible numerical solutions, we extensively analyzed thixoviscoplastic flows for different flow configurations, not only to overcome the modeling constraint, but also to provide efficient numerical methods and algorithmic tools.

With thixoviscoplastic channel flow, we upgraded the viscoplastic channel flow benchmark to incorporate microstructure. We took the reduced one-dimensional solution profiles to provide the necessary boundary conditions (inflow boundary conditions), alternative boundary conditions at the outflow (Dirichlet instead of "do-nothing"), beside as a solution's validation mechanism at each x-axis cross section along the channel.

Then, we moved to thixoviscoplastic lid-driven cavity flow as a long-standing flow benchmark for CFD in academia. We used it to validate thixoviscoplastic point-wise solutions, and to analyze the performance of the Newton-multigrid solver for this coupled multifield problem. The solver had to deal with few additional numerical challenges. The Newton-multigrid solver showed mesh refinement independent behavior.

In order to validate and calibrate our numerical method for an optimal settings with experimental data that we lack for thixoviscoplastic material, we revisited the powder Couette flow. We highlighted the issue of the types of transitions between fluid-like and solid-like zone. Then, we proceeded with the help of microstructure to categorize the types of transitions, shear localization and shear banding.

Lastly, we considered the contraction configuration as simple enough for industrial and engineering applications. We analyzed the competition processes of *Aging* and *Shear Rejuvenation* of thixotropic phenomena inhabited in thixoviscoplastic material. At higher breakdown parameter values, thixoviscoplastic contraction flow induced additional rejuvenation layers at the vicinity of the channel's walls, which might allow the material to flow smoothly. This particularity of thixoviscoplastic flows highlights the need to take into account the inhabited thixotropic material's rheology. As for instance, the revisit of the optimal restart pressure settings in waxy crude oil transportation.

5

Summary and outlook

In this thesis, we investigated thixoviscoplasticity in fluid flow problems with the lens of numerical simulations. We addressed the challenges with respect to theoretical analysis, numerical method, and the implementation of efficient algorithms. Our multi-aspect research results in the development of new numerical methods and algorithmic tools, which we used to provide extensive numerical simulations of thixoviscoplastic flow problems for academical benchmarks, as well as for modeling and industrial communities.

To start with, we highlighted the micro-macro structure connections of TVP flow problems. We selected the classical Houška's TVP model. Then, we formulated the problem in a generalized FEM settings of Stokes equations. To do so, we used quasi-Newtonian modeling approach, which is based on extended viscosity function defined on the full computational domain. We used the classical Bercovier-Engelmann's, and Papanastasiou's regularizations [13, 66].

After that, we analyzed the full set of equations, and exposed the nonlinear multifield two-way coupling aspect of the problem. We tackled the theoretical challenges with respect to different types of nonlinearities in an integrated way, as the nonlinear multifield coupled TVP problem is sensitive to coupling. Thus, we treated auxiliary subproblems with different analysis tools, and proceeded to guarantee existence of solutions for the multifield coupled TVP problem. We provided the well-posedness results for the TVP problem in FEM settings. Our well-posedness study is not an intellectual exercise, rather it is the foundation for the development of the efficient solver. In this regard, we advantageously used the delicate symbiosis aspects of the problem settings for FEM approximations, and the algorithmic tools to develop a monolithic Newton-multigrid TVP solver.

Our developed FEM-TVP solver is based on the monolithic Newton-multigrid method. The solver tackled the TVP generalized Stokes equations, and treats the nonlinearity and coupling of the problem in black box framework. The linear systems inside the outer nonlinear iterations of Newton's method are solved in a block Gauss-Seidel way, where the construction of the blocks is based on incompressibility constraint. Substantially, we handled the problem coupling efficiently with the choice of *discontinuous* linear approximation P_1^{disc} for pressure. We maintained the efficiency of the solver, due to the noncoupling of pressure and microstructure, with the collocation of microstructure and velocity components in the same quadratic FEM approximations Q_2. Furthermore, we dealt with the weak coercivity of microstructure form with edge-oriented stabilization, to upgrade the coercivity to match the space norm. It is consistent with FEM discretization, linear with respect to the problem, and in addition it enhanced the efficiency of the solver.

In the context of numerical simulations, we incorporated thixotropy in well-established academical benchmarks, namely channel flow and lid-driven cavity flow. In the former, we developed a reduced one-

dimensional TVP solver, then we generated reference solutions for higher-dimensional FEM fully developed TVP flow problem. We used the reduced one-dimensional solutions as a validation mechanism, and as necessary Dirichlet boundary conditions at inflow for microstructure, or as alternative Dirichlet boundary conditions instead of "do-nothing" at the outflow. For the lid-driven cavity, we used this case for the visual validations of the solution's domains, and to optimize the algorithmic tools. For both, channel flow, and lid-driven cavity flow, we related the sharpness of interfaces between unyielded and yielded regions to microstructure via evolution process, which occurs in the transitions at the boundary limit of the regions. In addition, we anticipated equations in cross engineering disciplines to model and replicate numerically the rheological phenomena, namely shear localization and shear banding in Couette device. In the end, we used thixotropy in contraction configuration to generate breakdown layers at the vicinity of downstream channel's walls, that keep the TVP material smoothly flowing along the downstream channel. Consequently, our findings highlight the benefit of including the material microstructure, namely thixotropy, in material rheology. As an industrial application, the optimal settings for restart pressure in waxy crude oil transportation.

Without restriction, we treated TVP problems in a steady state framework. The monolithic aspect of developed TVP solver enables it to straightforwardly handle time-dependent TVP problems. It is worth mentioning that this is an additional reason behind our favoured choice of monolithic approach at current stage of TVP investigations. Next immediate investigations would be in the direction to analyze thixotropy in time-dependent problems from theoretical perspective as well as for applications. With reliable reference results obtained so-far from the monolithic approach, proceeding with an operator-splitting approach might start to attract attention as well. In addition, the extension for models with shear rate dependent plastic-viscosity is straightforward, and the established theoretical results are adaptable for corresponding proper Sobolev spaces.

Furthermore, in our current settings of employed TVP model, the rheological manifestation of thixotropy is limited to viscoplastic materials. For future investigations (see Figure 5.1), we anchor modifications in constitutive laws toward thixotropic elasto-viscoplastic (TEVP) models (for instance [41, 72, 73]), that could accommodate both elastic and plastic characteristics of material in a single backbone.

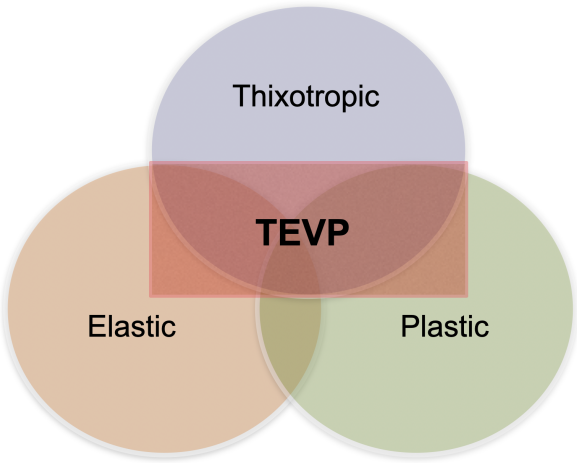

Fig. 5.1: **Thesis outlook:** Flow simulations of TVP model a gateway toward general thixotropic elasto-viscoplastic (TEVP) flow simulations.

References

[1] Aposporidis, A., Haber, E., Olshanskii, M. A., and Veneziani, A. A mixed formulation of the Bingham fluid flow problem: Analysis and numerical solution. *Computer Methods in Applied Mechanics and Engineering*, 200(29):2434–2446, 2011.

[2] Arnold, D. N., Brezzi, F., Cockburn, B., and Marini, L. D. Unified Analysis of Discontinuous Galerkin Methods for Elliptic Problems. *SIAM Journal on Numerical Analysis*, 39(5):1749–1779, 2002.

[3] Arnold, D.N., Boffi, D., and Falk, R.S. Approximation by Quadrilateral Finite Elements. *Math. Comput.*, 71(239):909–922, 2002.

[4] Bazilevs, Y., Gohean, J. R., Hughes, T. J. R., Moser, R. D., and Zhang, Y. Patient-specific isogeometric fluid–structure interaction analysis of thoracic aortic blood flow due to implantation of the Jarvik 2000 left ventricular assist device. *Computer Methods in Applied Mechanics and Engineering*, 198(45):3534–3550, 2009. Models and Methods in Computational Vascular and Cardiovascular Mechanics.

[5] Begum, N., Ouazzi, A., and Turek, S. FEM simulation for nonlinear multifield coupled problems: Application to thixoviscoplastic flow. In *X edition of the International Conference on Computational Methods for Coupled Problems in Science and Engineering*.

[6] Begum, N., Ouazzi, A., and Turek, S. Finite element methods for the simulation for the simulation of thixotropic flow. In *9th edition of the International Conference on Computational Methods for Coupled Problems in Science and Engineering*, 2021.

[7] Begum, N., Ouazzi, A., and Turek, S. Monolithic finite element method for the simulation of thixoviscoplastic flows. In *Book of Extended Abstracts of the 6th Eccomas Young Investigators Conference*, 2021.

[8] Begum, N., Ouazzi, A., and Turek, S. Monolithic Newton-multigrid FEM for the simulation of thixotropic flow problems. *Proc. Appl. Math. Mech.*, 21, 2021.

[9] Begum, N., Ouazzi, A., and Turek, S. FEM analysis and monolithic Newton-multigrid solver for thixo-viscoplastic flow problems. In *ECCOMAS Congress 2022 - 8th European Congress on Computational Methods in Applied Sciences and Engineering*, 2022.

[10] Begum, N., Ouazzi, A., and Turek, S. Efficient Newton-multigrid FEM Solver for Multifield Nonlinear Coupled Problems Applied to Thixoviscoplastic Flows. *Proc. Appl. Math. Mech.*, 24, 2023.

[11] Begum, N., Ouazzi, A., and Turek, S. FEM modelling and simulation of thixoviscoplastic flow problems. In *AIP Conference Proceedings*, 2023. in press.

[12] Begum, N., Ouazzi, A., and Turek, S. FEM simulations of thixoviscoplastic flow problems: Error analysis. *Proc. Appl. Math. Mech.*, 23, 2023.

[13] Bercovier, M. and Engelman, M. A finite-element method for incompressible non-Newtonian flows. *Journal of Computational Physics*, 36(3):313–326, 1980.

[14] Blazy, S., Nazarov, S., and Specovius-Neugebauer, M. Artificial boundary conditions of pressure type for viscous flows in a system of pipes. *J. math. fluid. mech.*, 2005. to appear.

[15] Boffi, D. and Gastaldi, L. On the quadrilateral Q2-P1 element for the Stokes problem. *Int. J. Numer. Meth. Fluids*, 39:1001–1011, 2002.

[16] Bothe, D., Köhne, M., and Prüss, J. On a Class of Energy Preserving Boundary Conditions for Incompressible Newtonian Flows. *SIAM Journal on Mathematical Analysis*, 45(6):3768–3822, 2013.

[17] Boyd, D. W. and Wong, J. S. W. On Nonlinear Contractions. *Proceedings of the American Mathematical Society*, 20(2):458–464, 1969.

[18] Braack, M. and Mucha, P. B. Directional Do-Nothing condition for the Navier-Stokes equations . *Journal of Computational Mathematics*, 32(5):507–521, 2014.

[19] Brenner, C. S. Korn's Inequalities for Piecewise H^1 Vector Fields. *Math. Comp.*, 73:1067–1087, 2004.

[20] Brenner, S. C. and Scoot, L. R. *The Mathematical Theory of Finite Element Methods*. Second edition, Springer, 2002.

[21] Brenner, S. C. and Zhao, J. Convergence of Multigrid Algorithms for Interior Penalty Methods. *Applied Numerical Analysis & Computational Mathematics*, 2(1):3–18.

[22] Brezzi, F. and Fortin, M. *Mixed and Hybrid Finite Element methods*. Springer, Berlin, 1986.

[23] Browder, F. E. Nonlinear elliptic boundary value problems. *Bulletin of the American Mathematical Society*, 69(6):862 – 874, 1963.

[24] Browder, F. E. and Hess, P. Nonlinear mappings of monotone type in Banach spaces. *Journal of Functional Analysis*, 11(3):251–294, 1972.

[25] Bruneau, C. and Saad, M. The 2D lid-driven cavity problem revisited. *Computers & Fluids*, 35:326–348, 2006.

[26] Burman, E. Stabilized Finite Element Methods for Nonsymmetric, Noncoercive, and Ill-Posed Problems. Part I: Elliptic Equations. *SIAM Journal on Scientific Computing*, 35(6):A2752–A2780, 2013.

[27] Burman, E. Stabilized Finite Element Methods for Nonsymmetric, Noncoercive, and Ill-Posed Problems. Part II: Hyperbolic Equations. *SIAM Journal on Scientific Computing*, 36(4):A1911–A1936, 2014.

[28] Coppola-Owen, A. H. and Codina, R. Improving Eulerian two-phase flow finite element approximation with discontinuous gradient pressure shape functions. *International Journal for Numerical Methods in Fluids*, 49(12):1287–1304, 2005.

[29] Coussot, P., Nguyen, Q. D., Huynh, H. T., and Bonn, D. Viscosity bifurcation in thixotropic, yielding fluids. *J. Rheol.*, 46(3):573–589, 2002.

[30] Damanik, H. *FEM Simulation of Non–isothermal Viscoelastic Fluids*. PhD Thesis, Technical University of Dortmund, 2011.

[31] Damanik, H., Hron, J., Ouazzi, A., and Turek, S. A monolithic FEM–multigrid solver for non–isothermal incompressible flow on general meshes. *Journal of Computational Physics*, 228:3869–3881, 2009.

[32] Damanik, H., Hron, J., Ouazzi, A., and Turek, S. Monolithic Newton-multigrid solution techniques for incompressible nonlinear flow models. *International Journal for Numerical Methods in Fluids*, Volume 71, Issue 2:208–222, 2012.

[33] Dullaert, K. and Mewis, J. Transient phenomena in thixotropic systems. *J. Non-Newton. Fluid Mech.*, 139:31–30, 2006.

[34] Engelman, M. S., Haroutunian, V., and Hasbani, I. Segregated finite element algorithms for the numerical solution of large–scale incompressible flow problems . *Int. J. Numer. Meth. Fluids*, 17:323–348, 1993.

[35] Fatima, A. *An Adaptive Discrete Newton Method for Regularization–Free Bingham Model*. PhD Thesis, TU Dortmund University, 2023.

[36] Fatima, A., Turek, S., Ouazzi, A., and Afaq, A. An Adaptive Discrete Newton Method for Regularization–Free Bingham Model. Technical report, Fakultät für Mathematik, TU Dortmund, January 2021. Ergebnisberichte des Instituts für Angewandte Mathematik, Nummer 635.

[37] Feistauer, M. Mathematical methods in fluid dynamics. *Pitman Monographs and Surveys in Pure and Applied Mathematics 67, Longman Scientific & Technical*, (67), 1993.

[38] Fernández, M., Moura, A., and Vergara, C. Defective boundary conditions applied to multiscale analysis of blood flow. *Esaim: Proceedings*, 14:89–99, 2005.

[39] Ferziger, J. H. and Peric, M. *Computational Methods for Fluid Dynamics*. Springer Verlag, Berlin–Heidelberg, 1996.

[40] Formaggia, L., Gerbeau, J. F., Nobile, F., and Quarteroni, A. Numerical Treatment of Defective Boundary Conditions for the Navier–Stokes Equations. *SIAM Journal on Numerical Analysis*, 40(1):376–401, 2002.

[41] Giannokostas, K. and Dimakopoulos, Y. Tevp model predictions of the pulsatile blood flow in 3d aneurysmal geometries. *Journal of Non-Newtonian Fluid Mechanics*, 311:104969, 2023.

[42] Girault, V. and Raviart, P. A. *Finite Element Methods for Navier-Stokes equations*. Springer, 1986. Berlin-Heidelberg .

[43] Guermond, J. Stabilization of Galerkin approximations of transport equations by subgrid modeling. *ESAIM: M2AN*, 33(6):1293–1316, 1999.

[44] Heywood, J. P., Rannacher, R., and Turek, S. Artificial boundaries and flux and pressure conditions for incompressible Navier Stokes equations. *Int. J. Numer. Math. Fluids*, 22:325–352, 1996.

[45] Houška, M. *Engineering aspects of the rheology of thixotropic liquids*. PhD Thesis, Faculty of Mechanical Engineering, Czech Technical University of Prague, 1981.

[46] Hysing, S. *Numerical simulation of immiscible fluids with FEM level set techniques*. PhD thesis, Technische Universität Dortmund, December 2007.

[47] Jenny, M., Kiesgen de Richter, S., Louvet, N., Skali-Lami, S., and Dossmann, Y. Taylor-Couette instability in thixotropic yield stress fluids. *Phys. Rev. Fluids*, 2:023302–023323, 2017.

[48] Köster, M., Ouazzi, A., Schieweck, F., Turek, S., and Zajac, P. New robust nonconforming finite elements of higher order. *Applied Numerical Mathematics*, 62:166–184, 2012.

[49] Kupperman, R. A central-difference scheme for a pure stream function formulation of incompressible viscous flow. *SIAM J. Sci. Comp.*, 23:1–18, 2001.

[50] Langroudi, M. K., Tardos, G. I., Michaels, J. N., and Mort, P. Effect of Material Properties, Boundary Conditions and Flow Fields on the Rheology of Dense Granular Matter. In *Powders and Grains 2009*, volume 1145 of *American Institute of Physics Conference Series*, pages 587–590, 2009.

[51] Langroudi, M. K., Turek, S., Ouazzi, A., and Tardos, G. I. An investigation of frictional and collisional powder flows using a unified constitutive equation. *Powder Technology*, 197(1-2):91–101, 2009.

[52] Lesaint, P. and Raviart, P. A. On a Finite Element Method for Solving the Neutron Transport Equation. Number 8. Publications des séminaires de mathématiques et informatique de Rennes, 1974.

[53] Mandal, S. *Efficient FEM solver for quasi–Newtonian flow problems with application to granular materials*. PhD Thesis, TU Dortmund University, 2017.

[54] Mandal, S., Ouazzi, A., and Turek, S. Modified Newton solver for yield stress fluids. In *Proceedings of ENUMATH 2015, the 11th European Conference on Numerical Mathematics and Advanced Applications*, pages 481–490. Springer, 2016.

[55] Martin, W. R. *The Application of the Finite Element Method to the Neutron Transport Equation*. PhD thesis, The University of Michigan, 1976.

[56] Mehlmann, C. and Richter, T. A modified global Newton solver for viscous-plastic sea ice models. *Ocean Modelling*, 116:96–107, 2017.

[57] Minty, G. J. Monotone (non-linear) operators in Hilbert space. *Duke. Math. J.*, 29:341–346, 1962.

[58] Minty, G. J. On a "Monotonicity" Method for the Solution of Nonlinear Equations in Banach Spaces. *Proceedings of the National Academy of Sciences of the United States of America*, 50:1038–41, 1963.

[59] Mujumdar, A., Beris, A. N., and Metzner, A. B. Transient phenomena in thixotropic systems. *J. Nonnewton. Fluid Mech.*, 102(2):157–178, 2002.

[60] Nashed, M. Z. and Wong, J. S. W. Some Variants of a Fixed Point Theorem of Krasnoselskii and Applications to Nonlinear Integral Equations. *Journal of Mathematics and Mechanics*, 18(8):767–777, 1969.

[61] Nitsche, J. On Korn's second inequality. *R.A.I.R.O.*, 15:562–580, 1981.

[62] Ouazzi, A. *Finite Element Simulation of Nonlinear Fluids: Application to Granular Material and Powder*. Shaker Verlag, 2006.

[63] Ouazzi, A., Begum, N., and Turek, S. Newton-Multigrid FEM solver for the simulation of quasi-Newtonian modelling of thixotropic flows. In *Numerical Methods and Algorithms in Science and Engineering*, volume 700, 2021.

[64] Ouazzi, A., Damanik, H., Hron, J., and Turek, S. FEM Techniques for the LCR Reformulation of Viscoelastic Flow Problems. In *Numerical Mathematics and Advanced Applications 2009*, Enumath 2009, pages 747–754. Springer, 2010.

[65] Ouazzi, A. and Turek, S. Efficient multigrid and data structures for edge-oriented fem stabilization. In Alfredo Bermúdez de Castro, Dolores Gómez, Peregrina Quintela, and Pilar Salgado, editors, *Numerical Mathematics and Advanced Applications*, pages 520–527, Berlin, Heidelberg, 2006. Springer Berlin Heidelberg.

[66] Papanastasiuo, T.C. Flow of materials with yield. *J. Rheol.*, 31:385–404, 1987.

[67] Pollock, S., Rebholz, L. G., and Vargun, D. Anderson acceleration for a regularized Bingham model. *Numerical Methods for Partial Differential Equations*, 39(5):3874–3896, 2023.

[68] Razzaq, M, Damanik, H., Hron, J., Ouazzi, A., and Turek, S. FEM multigrid techniques for fluid–structure interaction with application to hemodynamics. *Applied Numerical Mathematics*, 62(9):1156–1170, 2012. Numerical Analysis and Scientific Computation with Applications (NASCA).

[69] Saad, Y. *Iterative Methods for Sparse Linear Systems*. Society for Industrial and Applied Mathematics, second edition, 2003.

[70] Sampath, R. S., Adavani, S. S., Sundar, H., Lashuk, I., and Biros G. Dendro: parallel algorithms for multigrid and AMR methods on 2: 1 balanced octrees. In *Proceedings of the ACM/IEEE Conference on High Performance Computing, SC 2008, November 15-21, 2008, Austin, Texas, USA*, page 18. IEEE/ACM, 2008.

[71] Sampath, R. S. and Biros, G. A Parallel Geometric Multigrid Method for Finite Elements on Octree Meshes. *SIAM Journal on Scientific Computing*, 32(3):1361–1392, 2010.

[72] Saramito, P. Efficient simulation of nonlinear viscoelastic fluid flows. *Journal of Non-Newtonian Fluid Mechanics*, 60(2):199–223, 1995.

[73] Saramito, P,. A new constitutive equation for elastoviscoplastic fluid flows. *Journal of Non-Newtonian Fluid Mechanics*, 145(1):1–14, 2007.

[74] Simon, J. S. and Notsu, H. A convective boundary condition for the Navier-Stokes equations. *Appl. Math. Lett.*, 128:107876, 2021.

[75] Temam, R. *Navier-Stokes Equations Theory and Numerical Analysis*. Elsevier, 1979.

[76] Turek, S. *Efficient solvers for incompressible flow problems: An algorithmic and computational approach*. Springer, 1999.

[77] Turek, S. and Ouazzi, A. Unified edge–oriented stabilization of nonconforming FEM for incompressible flow problems: Numerical investigations. *Journal of Numerical Mathematics*, 15(4):299–322, 2007.

[78] Turek, S., Ouazzi, A., and Hron, J. On pressure separation algorithms (PSepA) for improving the accuracy of incompressible flow simulations. *J. Numer. Meth. Fluids*, 59:387–403, 2009.

[79] Vanka, S. P. Block–implicit multigrid solution of Navier–Stokes equations in primitive variables. *J. of Comp. Phys.*, 65:138–158, 1986.

[80] Wachs, A., Vinay, G., and Frigaard, I. A. A 1.5D numerical model for the start up of weakly compressible flow of a viscoplastic and thixotropic fluid in pipelines. *J. Non-Newtonian Fluid Mech.*, 159:81–94, 2009.

[81] Westervoss, P. *The Tensor Diffusion approach as a novel technique for simulating viscoelastic fluid flows*. PhD thesis, TU Dortmund, 2021.

[82] Worrall, W. and Tuliani, S. Viscosity changes during the aging of clay-water suspensions. *Trans. Brit. Ceramic Soc.*, 63:164–185, 1964.

[83] Zahedi, S., Kronbichler, M., and Kreiss, G. Spurious currents in finite element based level set methods for two-phase flow. *International Journal for Numerical Methods in Fluids*, 69(9):1433–1465, 2012. DOI: 10.1002/fld.2643.